Università degli Studi di Cagliari
Dipartimento di Ingegneria civile, Ambientale e Architettura
Dottorato di Ricerca in Ingegneria civile e Architettura
XXXII ciclo

PhD thesis on topic

“WAVE PROPAGATION IN ELASTIC MEDIA WITH INTERNAL STRUCTURE. PERIODIC TRANSFORMATIONS AND CURVED BEAMS”

submitted for the degree of Doctor of Philosophy
in Civil and Architecture Engineering (ICAR/08) by

BIBINUR MEIRBEKOVA

Supervisor: Prof. Michele Brun
Coordinator: Prof. Ivan Blečić

2018-2019 a.y.

Acknowledgements

First of all, I would like to express my gratitude to my supervisor prof. Michele Brun for his very useful suggestions and feedback during my Ph.D. thesis. He spent a lot of time with me, teaching me various aspects of research. I have benefited in various aspects, such as computational and analytical methods, professionalism in research, writing techniques, etc. I sincerely hope that our friendship and scientific cooperation will last for many years.

I am also grateful to the University of Cagliari for providing me with a full research scholarship for studies in university and abroad periods in France (University of Le Mans, LAUM).

I'm not going to be able to thank all the old and new friends who help me, one by one, sadly. The collection will be infinite. Last but not least, I would like to thank my family for their wise advice and kind words, as well as encouraging me if I have ever lost interest.

Contents

Chapter 1

General introduction

Recently, one of the most remarkable developments of modern scientific research is the production of *metamaterials*. The advantage of these artificial made media is that they exhibit exotic capabilities to control wave propagation [1–3] which significantly compensate those not found in traditional materials. Traveling wave paths are based on the material's complex properties that can be created by geometric transformation [4, 5]. Many unusual anomalies that are not currently possible for natural materials, such as negative refraction [6, 7], spontaneous emission control [8, 9], and anomalous tunneling effects, due to their extraordinary ability to control wave propagation [10, 11].

Probably, the most famous application consists in the possibility to make an object invisible to an impinging wave, by placing it in a cloak having the capability to cancel the scattering induced by the object itself. The research of invisibility dates back to previous centuries [12–14] and interesting models were also proposed in elasticity, including a coated elastic hole that, under specific external loads, does not perturb the static field [15], the coated sphere assemblage for hydrostatic loads [16, 17] and the energetically neutral inclusion covered by a structural interface [18].

Nevertheless, it was with the advent of metamaterials that the attention on the topic reached a vast community. Active and passive cloaks are applied to hide an object. An active cloak consists of a set of discrete multipole sources distributed in space to destructively interfere with an incident time-harmonic waves so as to nullify the total field in some finite domain and ensure that, in the far field, only the incident wave is present. The idea, which takes inspiration from active control of sound [19, 20], was applied to electromagnetism [21, 22], acoustics [23, 24], vector elasticity [25] and flexural waves in thin plates [26].

Passive systems are based on geometric transformation techniques, where a simply connected region, most often a circle, is mapped into a multiply connected one (an annulus). In the past conformal mappings, which are locally non deviatoric transformations, where frequently used to solve plane problems of mechanics [27, 28], with the possibility to take advantage of the properties of complex variable. Greenleaf, Lassas an Uhlmann [29, 30] showed that singular transformations could lead to cloaking for conductivity, while [4] and [5] made the key observation that singular transformations could be used to achieve cloaking of electromagnetic waves. A regular transformation was proposed in [31, 32] where a small, but finite central simply connected domain is transformed into a larger one. The theory for acoustic cloaking is presented in [33], where, instead of the differential geometry formalism, a formulation adapted from the theory of finite elasticity was adopted. For problems governed by the Helmholtz equation the transformed equation can be associated to an inhomogeneous and anisotropic material.

In vector elasticity, the wave equations are not invariant under a general mapping [34–36], since either non-symmetric stress or tensorial density are required. In this case, it was shown that the modified Newton's second law [37] remains invariant under specific conditions. The biharmonic equation for flexural wave propagation in Kirchhoff plates is transformed into an equation of an inhomogeneous and anisotropic plate in presence of in-plane stress [38, 39] usually studied in problems of static buckling of plates.

Extended reviews on transformation optics in metamaterials in different fields, with a focus on experimental results, can be found in [40–42].

In this work, transformation optics techniques are applied periodically on a periodic system. Propagation of out of plane shear waves in linear elastodynamics is considered. An illustrative example in Figure 1.1 shows the capability of the system to cloak multiple void inclusions of relatively large size. By making use of the periodicity it is possible to cloak not only a single inclusion but a grating and, in addition, high reflective systems and multiple anomalous localised resonances [43–46] can be obtained.

The focus is initially on the comparative analysis of dispersive properties of the transformed and original systems. To analyse the dispersive properties, we implemented both finite element codes and the semi-analytical multipole expansion method. Concerning the multipole expansion method, the solution of the incident and scattered fields for a single obstacle can be found in [47], while dispersion properties in an infinite one-dimensional array and doubly periodic arrays of circular scatterers were carried out in [48] for out of plane shear waves and in [49–52] for flexural waves in Kirchhoff plates. Arbitrarily shaped obstacles were considered in [53, 54].

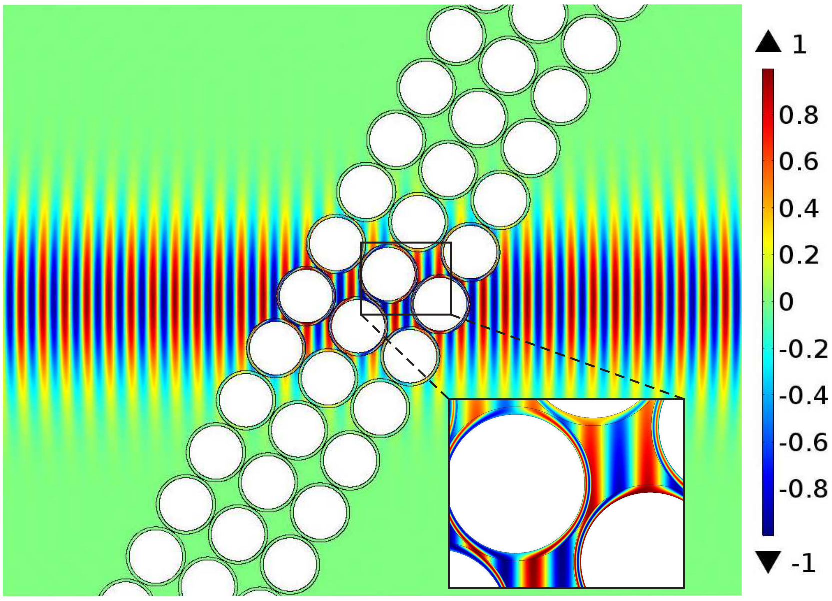

FIGURE 1.1: Wave transmission of a Gaussian beam throughout a slab of void inclusions. Each void is surrounded by a cloaking interface. Displacement distribution is shown, details on the computation are reported in Section 5.3.1.

A beam is typically described as a one-dimensional structural element significantly larger than its cross-sectional dimensions. It can be either flat or curved. It is possible to think that almost every structure or machine has one or more beam components. Curved beams are used in many elements of machines, such as c-clamps, crane rods, press frames, chains, links and rings, etc. In buildings they are usually visible around buildings for recreation, conference centers, cement bunkers, etc., where the circular beams serve the purpose in the form of ring beams.

Although straight beam dynamics are well studied, we cannot say the same about a curved beam. Our main objective is therefore to investigate the dynamic behavior of waves in curved beam, not only in a curved beam but also the propagation of waves in a complex structure containing straight and curved beam components.

Connected curved and straight beams are widely used in many engineering structures such as long-span bridges, train railways, aircraft structures, even pipes, which are used in house heating, water support and gas, oil transporting systems; they have been modelled as a combination of curved and straight beams [55]-[56]. In the second part of the Thesis, the dynamic behavior of these type of structures has been investigated.

In the past the research has been focused on how to derive, simplify and solve the equation of motion [57, 58], rather than studying the propagation, transmission and reflection of waves and determining the energy flow. Most of them analyzed the vibration of finite curved beam. Walsh and White [59] summarised the governing equations and developed the expressions for energy transmission for different theories of single curved beam. Recently, Søe-Knudsen [55]-[56] investigated the dynamics of compound elastic pipes with and without internal fluid loading. To predict the location of stop and pass band in infinite periodic structures, they applied the Floquet theory and used shape optimization procedure, derived Green's matrices and boundary integral equation for a curved pipe segments.

Wave propagation in elastic structures is a classical subject dating back to the early works of Taylor, Euler and Bernoulli. The theory of wave propagation is reported in several monographs [60–64]. In [61] it is shown that, in the low-frequency regime, the Euler-Bernoulli beam model is a good approximation for the wave propagation in a slender three-dimensional continuum, while at higher frequency the Timoshenko beam model gives better results. The coupled equations of motion for vibrations of curved beams are reported in [63, 64] and in the review papers [59, 65, 66]. They show a coupling between longitudinal and transverse modes which is not present in straight beams.

The attention of the scientific community is mainly devoted to finite structures and the computations of natural frequencies. Several models have been considered, including Love's theory, Flugge's theory, separate and combined effects of shear deformation, rotary inertia, warping due to torsional effects [59], damping and homogeneous and non-homogeneous distribution of material properties and cross-sectional shape [57]. Other applications include variable curvature (constant, polynomial, parabolic, elliptic, sinusoidal) and different boundary conditions [58, 67, 68]. Architected composite beam structures like laminated, sandwiched, periodic or complex combination of straight and curved beams or multi-span curved beam have been analysed in [55, 56, 69, 70], while application of the theory in piping systems can be found in [56, 69, 70].

Apart from few exceptions [71], the dispersive properties of periodic systems of curved beams have not been investigated in depth in the literature. Conversely, the dispersion analysis of periodic structures made of straight beams, with or without additional resonators, has been discussed extensively (see, for example, [72–76]).

In this thesis we will focus on the linear elastodynamic properties of complex materials. In *Chapter 2*, we review the linear theory of elasticity. This chapter provides a brief overview of the basic laws of elasticity theory for different coordinate systems, that will facilitate the further development of our research.

Dispersion properties of 2D periodic systems for different lattices are reported in *Chapter 3*.

The governing equations of out of plane wave and examples of coordinate transformations in Cartesian and cylindrical are considered in *Chapter 4*. Also the scattering problems by square and cylindrical uncloaked and cloaked holes are investigated analytically and numerically.

In *Chapter 5* a periodic transformation approach has been applied to the problem of out of plane shear wave propagation in an isotropic linear elastic material. The Chapter is organized as follows. In Section 5.1 we present initial and transformed equations of motion and corresponding boundary conditions, describing the periodic locally radial geometric transformation. In Section 5.2 we report the comparative analysis of dispersion properties and briefly describe the applied multipole expansion method. In particular, we focus our attention on classical, overlapping and unfolding transformations by also performing a low-frequency, long wavelength homogenisation. In Section 5.3 we show several application including a transmission problems in a continuum and in a waveguide, the detection of defect modes and the design of the transformation for the existence of Dirac points.

In *Chapter 6*, the mathematical model of a curved beam that is connected to two semi-infinite straight beams is developed. Dispersion properties of curved beams are derived, characterized by three different propagating regimes. By implementing the *Transfer matrix* approach, the reflection and transmission coefficients that depend on the curvature, frequency and total angle of the curved beam are determined. By analysing the effect of the curvature, frequency and total angle on *energy flux*, separation between high frequency/low curvature regime, where the incident wave is practically totally transmitted, and low frequency/high curvature regime where, in addition to reflection there is a strong coupling between longitudinal and flexural waves, are defined. Finally, general conclusions are given in the last chapter.

Chapter 2

Fundamentals of the elasticity theory

In this chapter, we build our path to models that are the basis for modern applied research in the field of Solid Mechanics. Therefore, we start with the derivation of the basic equations of linear elasticity.

2.1 Linear elastodynamic equations

In the presence of body force $\mathbf{B}$, the equation of motion, i.e. *the balance of linear momentum*, may be written as

$$\operatorname{Div} \mathbf{\Sigma} + \mathbf{B} = \dot{\mathbf{P}}, \tag{2.1}$$

where $\mathbf{\Sigma}$ is the Cauchy stress tensor, $\mathbf{P} = \rho \, \dot{\mathbf{U}}$ is the momentum, $\mathbf{U}(\mathbf{X}, t)$ is the vector of displacement, ρ is the density and $\mathbf{X}$ is the position vector, t is the time.

The deformation of the medium is described by the Green-Lagrange strain tensor $\boldsymbol{\varepsilon}$, which for small deformations, reduces to the symmetric tensor

$$\boldsymbol{\varepsilon} = \frac{1}{2}\Big[\nabla \mathbf{U} + \big(\nabla \mathbf{U}\big)^T\Big], \tag{2.2}$$

where $\nabla \mathbf{U}$ is the divergence of the displacement vector field. Eqn.(2.2) is the kinematic compatibility. In a linear elastic material, the small strain tensor $\boldsymbol{\varepsilon}$ is related to the Cauchy stress tensor $\mathbf{\Sigma}$ according to Hooke's law

$$\boldsymbol{\Sigma} = \mathbb{C}\,\boldsymbol{\varepsilon}, \tag{2.3}$$

in which the 81 coefficients of C_{ijkl} are called elastic constants and $\mathbb{C}$ is the *stiffness tensor*. The fourth-order stiffness tensor C_{ijkl} has major symmetry due to the existence of a strain energy function and minor symmetries due to symmetry of the Cauchy stress and deformation, thus, the number of independent elastic constants reduces from 81 to 21. In the case of an isotropic material, only two independent constants are needed and the stiffness tensor is defined as

$$C_{ijkl} = \lambda \delta_{ij}\delta_{kl} + \mu(\delta_{ik}\delta_{jl} + \delta_{il}\delta_{jk}), \tag{2.4}$$

where λ and μ are the Lamé moduli and δ is the Kronecker delta. The Kronecker delta is defined by

$$\delta_{ij} = \begin{cases} 0, & i \neq j \\ 1, & i = j \end{cases} \tag{2.5}$$

Alternatively, it is possible to introduce the engineering constants: the Young's modulus E, the Poisson's ratio ν, the shear modulus G and the bulk modulus K. The relationships between the Lamé and engineering constants are

$$\begin{aligned} \lambda &= \frac{\nu E}{(1+\nu)(1-2\nu)}, & \mu &= \frac{E}{2(1+\nu)}, \\ E &= \frac{\mu(2\mu+3\lambda)}{\mu+\lambda}, & \nu &= \frac{\lambda}{2(\mu+\lambda)}, \\ G &= \mu, & K &= \frac{E}{3(1-2\nu)}. \end{aligned} \tag{2.6}$$

The constraint on the constant are

$$\mu > 0, \quad \lambda > -2/3\,\mu, \quad E, G, K > 0$$

and Poisson's ratio must lie between

$$-1 < \nu \leq 0.5.$$

It is noted that, in the general case of an inhomogeneous medium, the mass density, and the elastic constants are functions of the position. Substituting eqn. (2.4) and eqn. (2.2) into eqn. (2.3), the balance of linear momentum (2.1) can be written in the Navier form as

$$(\lambda+\mu)U_{j,ji}+\mu U_{i,jj}+B_i=\rho\,\ddot{U}_i.$$

In tensorial form

$$(\lambda+\mu)\nabla\left(\nabla\cdot\mathbf{U}(\mathbf{X},t)\right)+\mu\Delta\mathbf{U}(\mathbf{X},t)+\mathbf{B}(\mathbf{X},t)=\rho\ddot{\mathbf{U}}(\mathbf{X},t). \tag{2.7}$$

Eqns. (2.7) are three equilibrium equations in terms of the displacement components. These are known as Navier equations or Lamé equations.

Eqns. (2.7) can be written in:

- Cartesian coordinate;
- Cylindrical coordinate;
- Spherical coordinate.

2.1.1 Cartesian coordinate

In three-dimensional Euclidean space, the displacement vector $\mathbf{U}$ is represented by a linear combination of unit vectors $\mathbf{E}_1$, $\mathbf{E}_2$, $\mathbf{E}_3$ as

$$\mathbf{U}=U_1\mathbf{E}_1+U_2\mathbf{E}_2+U_3\mathbf{E}_3, \tag{2.8}$$

where the three real numbers U_1, U_2, U_3 are components of the vector $\mathbf{U}$ along the given directions $\mathbf{E}_1$, $\mathbf{E}_2$ and $\mathbf{E}_3$, respectively. The components of $\mathbf{E}_1$, $\mathbf{E}_2$, $\mathbf{E}_3$ are $(1,0,0)$, $(0,1,0)$, $(0,0,1)$, respectively.

The gradient operator in Cartesian coordinates is

$$\nabla=\frac{\partial(\ )}{\partial X_1}\mathbf{E}_1+\frac{\partial(\ )}{\partial X_2}\mathbf{E}_2+\frac{\partial(\ )}{\partial X_3}\mathbf{E}_3. \tag{2.9}$$

The strain-displacement equations (2.2) are

$$\begin{aligned}
\varepsilon_{11} &= \frac{\partial U_1}{\partial X_1},\\
\varepsilon_{22} &= \frac{\partial U_2}{\partial X_2},\\
\varepsilon_{33} &= \frac{\partial U_3}{\partial X_3},\\
\varepsilon_{12} &= \frac{1}{2}\left(\frac{\partial U_1}{\partial X_2}+\frac{\partial U_2}{\partial X_1}\right),\\
\varepsilon_{13} &= \frac{1}{2}\left(\frac{\partial U_1}{\partial X_3}+\frac{\partial U_3}{\partial X_1}\right),\\
\varepsilon_{23} &= \frac{1}{2}\left(\frac{\partial U_2}{\partial X_3}+\frac{\partial U_3}{\partial X_2}\right).
\end{aligned} \tag{2.10}$$

The divergence of the displacement vector $\mathbf{U}$ is

$$\nabla\cdot\mathbf{U} = \frac{\partial U_1}{\partial X_1}+\frac{\partial U_2}{\partial X_2}+\frac{\partial U_3}{\partial X_3} \tag{2.11}$$

and its gradient is

$$\begin{aligned}
\nabla\mathbf{U} =& \frac{\partial U_1}{\partial X_1}\mathbf{E}_1\otimes\mathbf{E}_1+\frac{\partial U_1}{\partial X_2}\mathbf{E}_1\otimes\mathbf{E}_2+\frac{\partial U_1}{\partial X_3}\mathbf{E}_1\otimes\mathbf{E}_3+\\
&+\frac{\partial U_2}{\partial X_1}\mathbf{E}_2\otimes\mathbf{E}_1+\frac{\partial U_2}{\partial X_2}\mathbf{E}_2\otimes\mathbf{E}_2+\frac{\partial U_2}{\partial X_3}\mathbf{E}_2\otimes\mathbf{E}_3+\\
&+\frac{\partial U_3}{\partial X_1}\mathbf{E}_3\otimes\mathbf{E}_1+\frac{\partial U_3}{\partial X_2}\mathbf{E}_3\otimes\mathbf{E}_2+\frac{\partial U_3}{\partial X_3}\mathbf{E}_3\otimes\mathbf{E}_3,
\end{aligned} \tag{2.12}$$

then gradient of divergence of the displacement vector will be written as

$$\nabla(\nabla\cdot\mathbf{U}) = \frac{\partial}{\partial X_1}\left(\nabla\cdot\mathbf{U}\right)\mathbf{E}_1+\frac{\partial}{\partial X_2}\left(\nabla\cdot\mathbf{U}\right)\mathbf{E}_2+\frac{\partial}{\partial X_3}\left(\nabla\cdot\mathbf{U}\right)\mathbf{E}_3. \tag{2.13}$$

The Laplacian/divergence of the gradient of the displacement vector is

$$\nabla\cdot(\nabla\mathbf{U}) = \nabla^2\mathbf{U} = \Delta\mathbf{U} = \Delta U_1\mathbf{E}_1+\Delta U_2\mathbf{E}_2+\Delta U_3\mathbf{E}_3. \tag{2.14}$$

Substituting eqns. (2.13), (2.14) into eqn. (2.7), we obtain the Navier equation in terms of displacements

$$\begin{aligned}
(\lambda+\mu)\frac{\partial}{\partial X_1}(\nabla\cdot\mathbf{U})+\mu\Delta U_1+B_1&=\rho\ddot{U}_1,\\
(\lambda+\mu)\frac{\partial}{\partial X_2}(\nabla\cdot\mathbf{U})+\mu\Delta U_2+B_2&=\rho\ddot{U}_2,\\
(\lambda+\mu)\frac{\partial}{\partial X_3}(\nabla\cdot\mathbf{U})+\mu\Delta U_3+B_3&=\rho\ddot{U}_3.
\end{aligned} \tag{2.15}$$

The nine components of the Cauchy stress vector Σ_{ij} are components of a second-order Cartesian tensor, which completely defines the state of stress at a point and is given by

$$\begin{aligned}
\mathbf{\Sigma}=\Sigma_{11}\mathbf{E}_1\otimes\mathbf{E}_1+\Sigma_{12}\mathbf{E}_1\otimes\mathbf{E}_2+\\
+\Sigma_{13}\mathbf{E}_1\otimes\mathbf{E}_3+\ldots+\Sigma_{33}\mathbf{E}_3\otimes\mathbf{E}_3.
\end{aligned} \tag{2.16}$$

The equation of motion in terms of stress and displacements in Cartesian coordinates are

$$\begin{aligned}
\frac{\partial\Sigma_{11}}{\partial X_1}+\frac{\partial\Sigma_{12}}{\partial X_2}+\frac{\partial\Sigma_{13}}{\partial X_3}+B_1&=\rho\ddot{U}_1,\\
\frac{\partial\Sigma_{21}}{\partial X_1}+\frac{\partial\Sigma_{22}}{\partial X_2}+\frac{\partial\Sigma_{23}}{\partial X_3}+B_2&=\rho\ddot{U}_2,\\
\frac{\partial\Sigma_{31}}{\partial X_1}+\frac{\partial\Sigma_{32}}{\partial X_2}+\frac{\partial\Sigma_{33}}{\partial X_3}+B_3&=\rho\ddot{U}_3.
\end{aligned} \tag{2.17}$$

2.1.2 Cylindrical coordinate

The coordinate transformation from cylindrical (R,Θ,Z) to Cartesian coordinates (X_1,X_2,X_3) is

$$X_1=R\cos\Theta,\quad X_2=R\sin\Theta,\quad X_3=Z. \tag{2.18}$$

and the opposite transformation is

$$\begin{aligned}
R&=\sqrt{{X_1}^2+{X_2}^2},\\
\Theta&=2\arctan\left(\frac{X_2}{X_1+\sqrt{{X_1}^2+{X_2}^2}}\right),\\
Z&=X_3,
\end{aligned} \tag{2.19}$$

where $R \in [0, \infty)$, $\Theta \in [0, 2\pi)$, $Z \in (-\infty, \infty)$. Then the unit vectors

$$\mathbf{E}_R = \begin{pmatrix} \cos\Theta \\ \sin\Theta \\ 0 \end{pmatrix}, \quad \mathbf{E}_\Theta = \begin{pmatrix} -\sin\Theta \\ \cos\Theta \\ 0 \end{pmatrix}, \quad \mathbf{E}_Z = \begin{pmatrix} 0 \\ 0 \\ 1 \end{pmatrix}. \tag{2.20}$$

Derivatives of the unit vectors $\mathbf{E}_R, \mathbf{E}_\Theta, \mathbf{E}_Z$ with respect to the coordinates R, Θ, Z are

$$\begin{aligned} &\frac{\partial \mathbf{E}_R}{\partial R} = \mathbf{0}, \quad \frac{\partial \mathbf{E}_R}{\partial \Theta} = \mathbf{E}_\Theta, \quad \frac{\partial \mathbf{E}_R}{\partial Z} = \mathbf{0}, \\ &\frac{\partial \mathbf{E}_\Theta}{\partial R} = \mathbf{0}, \quad \frac{\partial \mathbf{E}_\Theta}{\partial \Theta} = -\mathbf{E}_R, \quad \frac{\partial \mathbf{E}_\Theta}{\partial Z} = \mathbf{0}, \\ &\frac{\partial \mathbf{E}_Z}{\partial R} = \mathbf{0}, \quad \frac{\partial \mathbf{E}_Z}{\partial \Theta} = \mathbf{0}\ , \quad \frac{\partial \mathbf{E}_Z}{\partial Z} = \mathbf{0}. \end{aligned} \tag{2.21}$$

The displacement vector in cylindrical coordinate is given by

$$\mathbf{U} = U_R \mathbf{E}_R + U_\Theta \mathbf{E}_\Theta + U_Z \mathbf{E}_Z. \tag{2.22}$$

The gradient operator is defined by

$$\nabla = \frac{\partial(\ )}{\partial R} \mathbf{E}_R + \frac{1}{R} \frac{\partial(\ )}{\partial \Theta} \mathbf{E}_\Theta + \frac{\partial(\ )}{\partial Z} \mathbf{E}_Z \tag{2.23}$$

and substituting the displacement vector $\mathbf{U}$ into the eqn. (2.23), we obtain

$$\nabla \cdot \mathbf{U} = \frac{\partial U_R}{\partial R} + \frac{1}{R} U_R + \frac{1}{R} \frac{\partial U_\Theta}{\partial \Theta} + \frac{\partial U_Z}{\partial Z}. \tag{2.24}$$

The gradient of the displacement vector is expressed by

$$\begin{aligned} \nabla \mathbf{U} = &\frac{\partial U_R}{\partial R} \mathbf{E}_R \otimes \mathbf{E}_R + \frac{\partial U_\Theta}{\partial R} \mathbf{E}_\Theta \otimes \mathbf{E}_R + \frac{\partial U_Z}{\partial R} \mathbf{E}_Z \otimes \mathbf{E}_R + \\ &+ \frac{1}{R} \left(\frac{\partial U_R}{\partial \Theta} - U_\Theta \right) \mathbf{E}_R \otimes \mathbf{E}_\Theta + \frac{1}{R} \left(\frac{\partial U_\Theta}{\partial \Theta} + U_R \right) \mathbf{E}_\Theta \otimes \mathbf{E}_\Theta + \\ &+ \frac{1}{R} \frac{\partial U_Z}{\partial \Theta} \mathbf{E}_Z \otimes \mathbf{E}_\Theta + \frac{\partial U_R}{\partial Z} \mathbf{E}_R \otimes \mathbf{E}_Z + \frac{\partial U_\Theta}{\partial Z} \mathbf{E}_\Theta \otimes \mathbf{E}_Z + \frac{\partial U_Z}{\partial Z} \mathbf{E}_Z \otimes \mathbf{E}_Z. \end{aligned} \tag{2.25}$$

Next, we consider the strain tensor for expression through the derivatives of the displacement vector $\mathbf{U}$ in cylindrical coordinates. The components of the deformation tensor are computed as

$$\varepsilon_{ij} = \mathbf{E}_i \cdot \boldsymbol{\varepsilon}\, \mathbf{E}_j,$$

while

$$(\mathbf{E}_i \otimes \mathbf{E}_j)^T = \mathbf{E}_j \otimes \mathbf{E}_i.$$

Consider the normal deformation in direction R

$$\begin{aligned}
\varepsilon_{RR} = \frac{1}{2}\,\mathbf{E}_R \cdot \Bigg(& \frac{\partial U_R}{\partial R}\mathbf{E}_R \otimes \mathbf{E}_R + \frac{\partial U_\Theta}{\partial R}\mathbf{E}_\Theta \otimes \mathbf{E}_R + \dots \\
& + \frac{\partial U_R}{\partial R}\mathbf{E}_R \otimes \mathbf{E}_R + \frac{\partial U_\Theta}{\partial R}\mathbf{E}_R \otimes \mathbf{E}_\Theta + \dots \Bigg)\mathbf{E}_R \\
& = \frac{1}{2}\,\mathbf{E}_R \cdot \Bigg(2\frac{\partial U_R}{\partial R}\mathbf{E}_R + \frac{\partial U_\Theta}{\partial R}\mathbf{E}_\Theta + \frac{\partial U_Z}{\partial R}\mathbf{E}_Z + \\
& + \frac{1}{R}\left(\frac{\partial U_R}{\partial \Theta} - U_\Theta\right)\mathbf{E}_\Theta + \frac{\partial U_R}{\partial Z}\mathbf{E}_Z\Bigg) = \frac{\partial U_R}{\partial R}.
\end{aligned} \tag{2.26}$$

In direction Θ

$$\begin{aligned}
\varepsilon_{\Theta\Theta} = & \frac{1}{2}\,\mathbf{E}_\Theta \cdot \Bigg(\frac{\partial U_R}{\partial R}\mathbf{E}_R \otimes \mathbf{E}_R + \frac{\partial U_\Theta}{\partial R}\mathbf{E}_\Theta \otimes \mathbf{E}_R + \dots \\
& + \frac{\partial U_R}{\partial R}\mathbf{E}_R \otimes \mathbf{E}_R + \frac{\partial U_\Theta}{\partial R}\mathbf{E}_R \otimes \mathbf{E}_\Theta + \dots \Bigg)\mathbf{E}_\Theta = \\
= & \frac{1}{2}\,\mathbf{E}_\Theta \cdot \Bigg(\frac{1}{R}\left(\frac{\partial U_R}{\partial \Theta} - U_\Theta\right)\mathbf{E}_R + \frac{2}{R}\left(\frac{\partial U_\Theta}{\partial \Theta} + U_R\right)\mathbf{E}_\Theta + \\
& + \frac{1}{R}\frac{\partial U_Z}{\partial \Theta}\mathbf{E}_Z + \frac{\partial U_\Theta}{\partial R}\mathbf{E}_R + \frac{\partial U_\Theta}{\partial Z}\mathbf{E}_Z \Bigg) = \\
= & \frac{1}{R}\left(\frac{\partial U_\Theta}{\partial \Theta} + U_R\right).
\end{aligned} \tag{2.27}$$

The other components of the deformation tensor are

$$\begin{aligned}
\varepsilon_{ZZ} &= \frac{\partial U_Z}{\partial Z}, \\
\varepsilon_{R\Theta} &= \frac{1}{2}\left(\frac{1}{R}\left(\frac{\partial U_R}{\partial \Theta} - U_\Theta\right) + \frac{\partial U_\Theta}{\partial R}\right), \\
\varepsilon_{RZ} &= \frac{1}{2}\left(\frac{\partial U_R}{\partial Z} + \frac{\partial U_Z}{\partial R}\right), \\
\varepsilon_{\Theta Z} &= \frac{1}{2}\left(\frac{1}{R}\frac{\partial U_Z}{\partial \Theta} + \frac{\partial U_\Theta}{\partial Z}\right).
\end{aligned} \tag{2.28}$$

Then,

$$
\begin{aligned}
\nabla(\nabla\cdot\mathbf{U}) =& \biggl(\frac{\partial^2 U_R}{\partial R^2} + \frac{\partial^2 U_Z}{\partial R\partial Z} + \frac{1}{R}\biggl(\frac{\partial U_R}{\partial R} + \frac{\partial^2 U_\Theta}{\partial R\partial\Theta} \biggr) - \frac{1}{R^2}\biggl(U_R + \\
&+ \frac{\partial U_\Theta}{\partial\Theta} \biggr)\biggr) \mathbf{E}_R + \biggl(\frac{1}{R}\biggl(\frac{\partial^2 U_R}{\partial R\partial\Theta} + \frac{\partial^2 U_Z}{\partial\Theta\partial Z} \biggr) + \frac{1}{R^2}\biggl(\frac{\partial U_R}{\partial\Theta} + \\
&+ \frac{\partial^2 U_\Theta}{\partial\Theta^2} \biggr)\biggr) \mathbf{E}_\Theta + \biggl(\frac{\partial^2 U_R}{\partial R\partial Z} + \frac{\partial^2 U_Z}{\partial Z^2} + \frac{1}{R}\biggl(\frac{\partial U_R}{\partial Z} + \frac{\partial^2 U_\Theta}{\partial\Theta\partial Z} \biggr)\biggr) \mathbf{E}_Z
\end{aligned}
\tag{2.29}
$$

and the Laplacian is

$$
\begin{aligned}
\nabla\cdot(\nabla\mathbf{U}) =& \left(\frac{\partial^2 U_R}{\partial R^2} + \frac{\partial^2 U_R}{\partial Z^2} + \frac{1}{R}\frac{\partial U_R}{\partial R} + \frac{1}{R^2}\left(\frac{\partial^2 U_R}{\partial\Theta^2} - 2\frac{\partial U_\Theta}{\partial\Theta} - U_R \right)\right) \mathbf{E}_R \\
&+ \left(\frac{\partial^2 U_\Theta}{\partial R^2} + \frac{\partial^2 U_\Theta}{\partial Z^2} + \frac{1}{R}\frac{\partial U_\Theta}{\partial R} + \frac{1}{R^2}\left(\frac{\partial^2 U_\Theta}{\partial\Theta^2} + 2\frac{\partial U_R}{\partial\Theta} - U_\Theta \right)\right) \mathbf{E}_\Theta \\
&+ \left(\frac{\partial^2 U_Z}{\partial R^2} + \frac{\partial^2 U_Z}{\partial Z^2} + \frac{1}{R}\frac{\partial U_Z}{\partial R} + \frac{1}{R^2}\frac{\partial^2 U_Z}{\partial\Theta^2} \right) \mathbf{E}_Z.
\end{aligned}
\tag{2.30}
$$

Subsituting eqn. (2.29) and eqn. (2.30) into eqn. (2.7), we obtain the Navier equation in cylindrical coordinates

$$
\begin{aligned}
&(\lambda+\mu)\left(\frac{\partial^2 U_R}{\partial R^2} + \frac{\partial^2 U_Z}{\partial R\partial Z} + \frac{1}{R}\left(\frac{\partial U_R}{\partial R} + \frac{\partial^2 U_\Theta}{\partial R\partial\Theta} \right) - \frac{1}{R^2}\left(U_R + \frac{\partial U_\Theta}{\partial\Theta} \right)\right) + \\
&+ \mu\left(\frac{\partial^2 U_R}{\partial R^2} + \frac{\partial^2 U_R}{\partial Z^2} + \frac{1}{R}\frac{\partial U_R}{\partial R} + \frac{1}{R^2}\left(\frac{\partial^2 U_R}{\partial\Theta^2} - 2\frac{\partial U_\Theta}{\partial\Theta} - U_R \right)\right) - \\
&+ B_R = \rho\ddot{U}_R, \\[2ex]
&(\lambda+\mu)\left(\frac{1}{R}\left(\frac{\partial^2 U_R}{\partial R\partial\Theta} + \frac{\partial^2 U_Z}{\partial\Theta\partial Z} \right) + \frac{1}{R^2}\left(\frac{\partial U_R}{\partial\Theta} + \frac{\partial^2 U_\Theta}{\partial\Theta^2} \right)\right) + \\
&+ \mu\left(\frac{\partial^2 U_\Theta}{\partial R^2} + \frac{\partial^2 U_\Theta}{\partial Z^2} + \frac{1}{R}\frac{\partial U_\Theta}{\partial R} + \frac{1}{R^2}\left(\frac{\partial^2 U_\Theta}{\partial\Theta^2} + 2\frac{\partial U_R}{\partial\Theta} - U_\Theta \right)\right) - \\
&+ B_\Theta = \rho\ddot{U}_\Theta, \\[2ex]
&(\lambda+\mu)\left(\frac{\partial^2 U_R}{\partial R\partial Z} + \frac{\partial^2 U_Z}{\partial Z^2} + \frac{1}{R}\left(\frac{\partial U_R}{\partial Z} + \frac{\partial^2 U_\Theta}{\partial\Theta\partial Z} \right)\right) + \\
&+ \mu\left(\frac{\partial^2 U_Z}{\partial R^2} + \frac{\partial^2 U_Z}{\partial Z^2} + \frac{1}{R}\frac{\partial U_Z}{\partial R} + \frac{1}{R^2}\frac{\partial^2 U_Z}{\partial\Theta^2} \right) + B_Z = \rho\ddot{U}_Z.
\end{aligned}
\tag{2.31}
$$

In compact form, eqn. (2.31) can be written as

$$\begin{aligned}
&(\lambda+\mu)\frac{\partial}{\partial R}(\nabla\cdot\mathbf{U})+\mu\left(\nabla^2 U_R-\frac{1}{R^2}\left(2\frac{\partial U_\Theta}{\partial\Theta}+U_R\right)\right)+B_R=\rho\ddot{U}_R,\\
&\frac{\lambda+\mu}{R}\frac{\partial}{\partial\Theta}(\nabla\cdot\mathbf{U})+\mu\left(\nabla^2 U_\Theta+\frac{1}{R^2}\left(2\frac{\partial U_R}{\partial\Theta}-U_\Theta\right)\right)+B_\Theta=\rho\ddot{U}_\Theta,\\
&(\lambda+\mu)\frac{\partial}{\partial Z}(\nabla\cdot\mathbf{U})+\mu\nabla^2 U_Z+B_Z=\rho\ddot{U}_Z.
\end{aligned} \tag{2.32}$$

Equation of motion in terms of stress in cylindrical coordinates are

$$\begin{aligned}
&\Sigma_{RR,R}+\frac{1}{R}(\Sigma_{R\Theta,\Theta}+\Sigma_{RR}-\Sigma_{\Theta\Theta})+\Sigma_{RZ,Z}+B_R=\rho\ddot{U}_R,\\
&\Sigma_{\Theta R,R}+\frac{1}{R}(\Sigma_{\Theta\Theta,\Theta}+2\Sigma_{\Theta R})+\Sigma_{\Theta Z,Z}+B_\Theta=\rho\ddot{U}_\Theta,\\
&\Sigma_{ZR,R}+\frac{1}{R}(\Sigma_{Z\Theta,\Theta}+\Sigma_{ZR})+\Sigma_{ZZ,Z}+B_Z=\rho\ddot{U}_Z.
\end{aligned} \tag{2.33}$$

2.1.3 Spherical coordinate

The Cartesian coordinates (X_1, X_2, X_3) are related to the spherical coordinates (R, Θ, Φ) by

$$\begin{aligned}
X_1 =& R\cos\Theta\sin\Phi,\\
X_2 =& R\sin\Theta\sin\Phi,\\
X_3 =& R\cos\Phi
\end{aligned} \tag{2.34}$$

and the coordinates (R, Θ, Φ) in terms of the (X_1, X_2, X_3) by

$$\begin{aligned}
R &= \sqrt{{X_1}^2+{X_2}^2+{X_3}^2},\\
\Theta &= 2\arctan\left(\frac{X_2}{X_1+\sqrt{{X_1}^2+{X_2}^2}}\right),\\
\Phi &= \arccos\frac{X_3}{\sqrt{{X_1}^2+{X_2}^2+{X_3}^2}},
\end{aligned} \tag{2.35}$$

where $R \in [0, \infty)$, $\Theta \in [0, 2\pi)$, and $\Phi \in [0, \pi]$.

The unit vectors are

$$\mathbf{E}_R = \begin{pmatrix} \cos\Theta\sin\Phi \\ \sin\Theta\sin\Phi \\ \cos\Phi \end{pmatrix}, \quad \mathbf{E}_\Theta = \begin{pmatrix} -\sin\Theta \\ \cos\Theta \\ 0 \end{pmatrix}, \quad \mathbf{E}_\Phi = \begin{pmatrix} \cos\Theta\cos\Phi \\ \sin\Theta\cos\Phi \\ -\sin\Phi \end{pmatrix}. \tag{2.36}$$

Partial derivatives of the unit vectors are

$$\begin{aligned} &\frac{\partial \mathbf{E}_R}{\partial R} = \mathbf{0}, && \frac{\partial \mathbf{E}_R}{\partial \Theta} = \sin\Phi\,\mathbf{E}_\Theta, && \frac{\partial \mathbf{E}_R}{\partial \Phi} = \mathbf{E}_\Phi, \\ &\frac{\partial \mathbf{E}_\Theta}{\partial R} = \mathbf{0}, && \frac{\partial \mathbf{E}_\Theta}{\partial \Theta} = -\cos\Phi\,\mathbf{E}_\Phi - \sin\Phi\,\mathbf{E}_R, && \frac{\partial \mathbf{E}_\Theta}{\partial \Phi} = \mathbf{0}, \\ &\frac{\partial \mathbf{E}_\Phi}{\partial R} = \mathbf{0}, && \frac{\partial \mathbf{E}_\Phi}{\partial \Theta} = \cos\Phi\,\mathbf{E}_\Theta, && \frac{\partial \mathbf{E}_\Phi}{\partial \Phi} = -\mathbf{E}_R. \end{aligned} \tag{2.37}$$

Gradient operator is defined as

$$\nabla = \frac{\partial(\ )}{\partial R}\,\mathbf{E}_R + \frac{1}{R}\frac{\partial(\ )}{\partial \Phi}\,\mathbf{E}_\Phi + \frac{1}{R\sin\Phi}\frac{\partial(\ )}{\partial \Theta}\,\mathbf{E}_\Theta \tag{2.38}$$

and vector displacement in spherical coordinates can be written as

$$\mathbf{U} = U_R\mathbf{E}_R + U_\Phi\mathbf{E}_\Phi + U_\Theta\mathbf{E}_\Theta, \tag{2.39}$$

then divergence of the displacement vector is

$$\nabla\cdot\mathbf{U} = \frac{\partial U_R}{\partial R} + \frac{1}{R}\left(U_R + \frac{\partial U_\Phi}{\partial \Phi}\right) + \frac{1}{R\sin\Phi}\left(U_R\sin\Phi + U_\Phi\cos\Phi + \frac{\partial U_\Theta}{\partial \Theta}\right) \tag{2.40}$$

while the vector gradient is

$$\begin{aligned} \nabla\mathbf{U} =& \frac{\partial U_R}{\partial R}\,\mathbf{E}_R\otimes\mathbf{E}_R + \frac{\partial U_\Phi}{\partial R}\,\mathbf{E}_\Phi\otimes\mathbf{E}_R + \frac{\partial U_\Theta}{\partial R}\,\mathbf{E}_\Theta\otimes\mathbf{E}_R \\ &+\frac{1}{R}\left(\frac{\partial U_R}{\partial \Phi} - U_\Phi\right)\mathbf{E}_R\otimes\mathbf{E}_\Phi + \frac{1}{R}\left(U_R + \frac{\partial U_\Phi}{\partial \Phi}\right)\mathbf{E}_\Phi\otimes\mathbf{E}_\Phi + \\ &+\frac{1}{R}\frac{\partial U_\Theta}{\partial \Phi}\mathbf{E}_\Theta\otimes\mathbf{E}_\Phi + \frac{1}{R\sin\Phi}\left(\frac{\partial U_R}{\partial \Theta} - \sin\Phi U_\Theta\right)\mathbf{E}_R\otimes\mathbf{E}_\Theta + \\ &+\frac{1}{R\sin\Phi}\left(\sin\Phi\,U_R + \cos\Phi\,U_\Phi + \frac{\partial U_\Theta}{\partial \Theta}\right)\mathbf{E}_\Theta\otimes\mathbf{E}_\Theta \\ &+\frac{1}{R\sin\Phi}\left(\frac{\partial U_\Phi}{\partial \Theta} - \cos\Phi U_\Theta\right)\mathbf{E}_\Phi\otimes\mathbf{E}_\Theta. \end{aligned} \tag{2.41}$$

In the same way as for cylindrical coordinates we can find the strain-displacement relations for spherical coordinates

$$
\begin{aligned}
\varepsilon_{RR} &= \frac{\partial U_R}{\partial R},\\
\varepsilon_{\Phi\Phi} &= \frac{1}{R}\left(\frac{\partial U_\Phi}{\partial \Phi} + U_R\right),\\
\varepsilon_{\Theta\Theta} &= \frac{1}{R}\left(U_R + \cot\Phi\, U_\Phi\right) + \frac{1}{R\sin\Phi}\frac{\partial U_\Theta}{\partial \Theta},\\
\varepsilon_{R\Phi} &= \frac{1}{2}\left(\frac{\partial U_\Phi}{\partial R} + \frac{1}{R}\left(\frac{\partial U_R}{\partial \Phi} - U_\Phi\right)\right),\\
\varepsilon_{R\Theta} &= \frac{1}{2}\left(\frac{\partial U_\Theta}{\partial R} - \frac{1}{R}U_\Theta + \frac{1}{R\sin\Phi}\frac{\partial U_R}{\partial \Theta}\right),\\
\varepsilon_{\Phi\Theta} &= \frac{1}{2}\left(\frac{1}{R}\left(\frac{\partial U_\Theta}{\partial \Phi} - \cot\Phi\, U_\Theta\right) + \frac{1}{R\sin\Phi}\frac{\partial U_\Phi}{\partial \Theta}\right).
\end{aligned}
\tag{2.42}
$$

Gradient of divergence of the vector displacement $\mathbf{U}$ is

$$
\begin{aligned}
\nabla(\nabla\cdot\mathbf{U}) = &\left(\frac{\partial^2 U_R}{\partial R^2} + \frac{1}{R}\left(2\frac{\partial U_R}{\partial R} + \frac{\partial^2 U_\Phi}{\partial R\partial\Phi}\right) - \frac{1}{R^2}\left(2U_R + \frac{\partial U_\Phi}{\partial \Phi}\right) - \right.\\
&\left. -\frac{\cot\Phi}{R^2}U_\Phi + \frac{\cot\Phi}{R}\frac{\partial U_\Phi}{\partial R} - \frac{1}{R^2\sin\Phi}\frac{\partial U_\Theta}{\partial\Theta} + \frac{1}{R\sin\Phi}\frac{\partial^2 U_\Theta}{\partial R\partial\Theta}\right)\mathbf{E}_R +\\
&+\left(\frac{1}{R}\frac{\partial^2 U_R}{\partial\Phi\partial R} + \frac{1}{R^2}\left(2\frac{\partial U_R}{\partial\Phi} + \frac{\partial^2 U_\Phi}{\partial\Phi^2} + \cot\Phi\frac{\partial U_\Phi}{\partial\Phi} - \right.\right.\\
&\left.\left. -\frac{U_\Phi}{\sin^2\Phi} + \frac{1}{\sin\Phi}\frac{\partial^2 U_\Theta}{\partial\Phi\partial\Theta} - \frac{\cot\Phi}{\sin\Phi}\frac{\partial U_\Theta}{\partial\Theta}\right)\right)\mathbf{E}_\Phi +\\
&+\left(\frac{1}{R\sin\Phi}\frac{\partial^2 U_R}{\partial\Theta\partial R} + \frac{1}{R^2\sin\Phi}\left(\frac{\partial U_R}{\partial\Theta} + \frac{\partial^2 U_\Phi}{\partial\Theta\partial\Phi}\right) + \right.\\
&\left. +\frac{1}{R^2\sin^2\Phi}\frac{\partial^2 U_\Theta}{\partial\Theta^2} + \frac{1}{R^2\sin\Phi}\frac{\partial U_R}{\partial\Theta} + \frac{\cot\Phi}{R^2\sin\Phi}\frac{\partial U_\Phi}{\partial\Theta}\right)\mathbf{E}_\Theta .
\end{aligned}
\tag{2.43}
$$

Laplacian of the vector displacement is

$$
\begin{aligned}
\nabla\cdot\nabla\mathbf{U} =& \Bigg(\frac{\partial^2 U_R}{\partial R^2}+\frac{2}{R}\frac{\partial U_R}{\partial R}+\frac{1}{R^2}\left(\frac{\partial^2 U_R}{\partial \Phi^2}-2\frac{\partial U_\Phi}{\partial \Phi}-2U_R\right)+\\
&+\frac{1}{R^2\sin^2\Phi}\frac{\partial^2 U_R}{\partial \Theta^2}-\frac{2}{R^2\sin\Phi}\frac{\partial U_\theta}{\partial \Theta}+\frac{\cot\Phi}{R^2}\left(\frac{\partial U_R}{\partial \Phi}-2U_\Phi\right)\Bigg)\mathbf{E}_R+\\
&+\Bigg(\frac{\partial^2 U_\Phi}{\partial R^2}+\frac{2}{R}\frac{\partial U_\Phi}{\partial R}+\frac{1}{R^2}\left(\frac{\partial^2 U_\Phi}{\partial \Phi^2}+2\frac{\partial U_R}{\partial \Phi}\right)+\\
&+\frac{1}{R^2\sin^2\Phi}\left(\frac{\partial^2 U_\Phi}{\partial \Theta^2}-U_\Phi\right)-2\frac{\cot\Phi}{R^2\sin\Phi}\frac{\partial U_\Theta}{\partial \Theta}+\frac{\cot\Phi}{R^2}\frac{\partial U_\Phi}{\partial \Phi}\Bigg)\mathbf{E}_\Phi+\\
&+\Bigg(\frac{\partial^2 U_\Theta}{\partial R^2}+\frac{2}{R^2}\frac{\partial U_\Theta}{\partial R}+\frac{1}{R^2}\frac{\partial^2 U_\Theta}{\partial \Phi^2}+\frac{2}{R^2\sin\Phi}\frac{\partial U_R}{\partial \Theta}+2\frac{\cot\Phi}{R^2\sin\Phi}\frac{\partial U_\Phi}{\partial \Theta}\\
&+\frac{1}{R^2\sin^2\Phi}\frac{\partial^2 U_\Theta}{\partial \Theta^2}-\frac{U_\Theta}{R^2\sin^2\Phi}+\frac{\cot\Phi}{R^2}\frac{\partial U_\Theta}{\partial \Phi}\Bigg)\mathbf{E}_\Theta.
\end{aligned}
\tag{2.44}
$$

Substituting eqns. (2.43) and (2.44) into eqn. (2.7), we obtain the Navier equations

$$
\begin{aligned}
&(\lambda+\mu)\Bigg(\frac{\partial^2 U_R}{\partial R^2}+\frac{1}{R}\left(2\frac{\partial U_R}{\partial R}+\frac{\partial^2 U_\Phi}{\partial R\partial \Phi}\right)-\frac{1}{R^2}\left(2U_R+\frac{\partial U_\Phi}{\partial \Phi}\right)-\\
&-\frac{\cot\Phi}{R^2}U_\Phi+\frac{\cot\Phi}{R}\frac{\partial U_\Phi}{\partial R}-\frac{1}{R^2\sin\Phi}\frac{\partial U_\Theta}{\partial \Theta}+\frac{1}{R\sin\Phi}\frac{\partial^2 U_\Theta}{\partial R\partial \Theta}\Bigg)+\\
&+\mu\Bigg(\frac{\partial^2 U_R}{\partial R^2}+\frac{2}{R}\frac{\partial U_R}{\partial R}+\frac{1}{R^2}\left(\frac{\partial^2 U_R}{\partial \Phi^2}-2\frac{\partial U_\Phi}{\partial \Phi}-2U_R\right)+\frac{1}{R^2\sin^2\Phi}\cdot\\
&\frac{\partial^2 U_R}{\partial \Theta^2}-\frac{2}{R^2\sin\Phi}\frac{\partial U_\Theta}{\partial \Theta}+\frac{\cot\Phi}{R^2}\left(\frac{\partial U_R}{\partial \Phi}-2U_\Phi\right)\Bigg)+B_R=\rho\,\ddot{U}_R,\\[2ex]
&(\lambda+\mu)\Bigg(\frac{1}{R}\frac{\partial^2 U_R}{\partial \Phi\partial R}+\frac{1}{R^2}\Bigg(2\frac{\partial U_R}{\partial \Phi}+\frac{\partial^2 U_\Phi}{\partial \Phi^2}+\cot\Phi\frac{\partial U_\Phi}{\partial \Phi}-\frac{U_\Phi}{\sin^2\Phi}+\\
&\frac{1}{\sin\Phi}\frac{\partial U_\Theta}{\partial \Phi\partial \Theta}-\frac{\cot\Phi}{\sin\Phi}\frac{\partial U_\Theta}{\partial \Theta}\Bigg)\Bigg)+\mu\Bigg(\frac{\partial^2 U_\Phi}{\partial R^2}+\frac{2}{R}\frac{\partial U_\Phi}{\partial R}+\frac{1}{R^2}\Bigg(\frac{\partial^2 U_\Phi}{\partial \Phi^2}+\\
&2\frac{\partial U_R}{\partial \Phi}\Bigg)+\frac{1}{R^2\sin^2\Phi}\left(\frac{\partial^2 U_\Phi}{\partial \Theta^2}-U_\Phi\right)-2\frac{\cot\Phi}{R^2\sin\Phi}\frac{\partial U_\Theta}{\partial \Theta}+\frac{\cot\Phi}{R^2}\frac{\partial U_\Phi}{\partial \Phi}\Bigg)-\\
&+B_\Phi=\rho\,\ddot{U}_\Phi,
\end{aligned}
\tag{2.45}
$$

$$
\begin{aligned}
&(\lambda+\mu)\Bigg(\frac{1}{R\sin\Phi}\frac{\partial^2 U_R}{\partial\Theta\partial R}+\frac{1}{R^2\sin\Phi}\left(\frac{\partial U_R}{\partial\Theta}+\frac{\partial^2 U_\Phi}{\partial\Theta\partial\Phi}\right)+\\
&+\frac{1}{R^2\sin^2\Phi}\frac{\partial^2 U_\Theta}{\partial\Theta^2}+\frac{1}{R^2\sin\Phi}\frac{\partial U_R}{\partial\Theta}+\frac{\cot\Phi}{R^2\sin\Phi}\frac{\partial U_\Phi}{\partial\theta}\Bigg)+\mu\Bigg(\frac{\partial^2 U_\Theta}{\partial R^2}+\frac{2}{R^2}\cdot\\
&\frac{\partial U_\Theta}{\partial R}+\frac{1}{R^2}\frac{\partial^2 U_\Theta}{\partial\Phi^2}+\frac{2}{R^2\sin\Phi}\frac{\partial U_R}{\partial\Theta}+2\frac{\cot\Phi}{R^2\sin\Phi}\frac{\partial U_\Phi}{\partial\Theta}+\frac{1}{R^2\sin^2\Phi}\frac{\partial^2 U_\Theta}{\partial\Theta^2}-\\
&-\frac{U_\Theta}{R^2\sin^2\Phi}+\frac{\cot\Phi}{R^2}\frac{\partial U_\Theta}{\partial\Phi}\Bigg)+B_\Theta=\rho\,\ddot{U}_\Theta.
\end{aligned}
$$

The Navier equations can be compactly expressed in spherical coordinates

$$
\begin{aligned}
&(\lambda+\mu)\frac{\partial}{\partial R}\left(\nabla\cdot\mathbf{U}\right)+\mu\Bigg(\nabla^2 U_R-\frac{2}{R^2}\left(\frac{\partial U_\Phi}{\partial\Phi}+U_R\right)-\frac{2}{R^2\sin\Phi}\frac{\partial U_\Theta}{\partial\Theta}-\\
&\qquad\qquad-\frac{2\cot\Phi}{R^2}U_\Phi\Bigg)+B_R=\rho\,\ddot{U}_R,\\
&\frac{\lambda+\mu}{R}\frac{\partial}{\partial\Phi}\left(\nabla\cdot\mathbf{U}\right)+\mu\Bigg(\nabla^2 U_\Phi+\frac{2}{R^2}\frac{\partial U_R}{\partial\Phi}-\frac{U_\Phi}{R^2\sin^2\Phi}-\frac{2\cot\Phi}{R^2\sin\Phi}\cdot\\
&\qquad\qquad\cdot\frac{\partial U_\Theta}{\partial\Theta}\Bigg)+B_\Phi=\rho\,\ddot{U}_\Phi,\\
&\frac{\lambda+\mu}{R\sin\Phi}\frac{\partial}{\partial\Theta}\left(\nabla\cdot\mathbf{U}\right)+\mu\Bigg(\nabla^2 U_\Theta+\frac{2}{R^2\sin\Phi}\frac{\partial U_R}{\partial\Theta}+\frac{2\cot\Phi}{R^2\sin\Phi}\frac{\partial U_\Phi}{\partial\Theta}-\\
&\qquad\qquad-\frac{U_\Theta}{R^2\sin^2\Phi}\Bigg)+B_\Theta=\rho\,\ddot{U}_\Theta.
\end{aligned}
\tag{2.46}
$$

The equations of motion in terms of stress are

$$
\begin{aligned}
&\Sigma_{RR,R}+\frac{1}{R}\Big(\Sigma_{R\Phi,\Phi}-\Sigma_{\Phi\Phi}+2\Sigma_{RR}-\Sigma_{\Theta\Theta}\Big)+\frac{1}{R\sin\Phi}\Big(\Sigma_{R\Theta,\Theta}+\\
&\qquad+\cos\Phi\,\Sigma_{R\Phi}\Big)+B_R=\rho\,\ddot{U}_R,\\
&\Sigma_{\Phi R,R}+\frac{1}{R}\Big(\Sigma_{\Phi\Phi,\Phi}+3\,\Sigma_{R\Phi}\Big)+\frac{1}{R\sin\Phi}\Big(\Sigma_{\Phi\Theta,\Theta}-\cos\Phi\,\Sigma_{\Theta\Theta}+\cos\Phi\,\Sigma_{\Phi\Phi}\Big)-\\
&\qquad+B_\Phi=\rho\,\ddot{U}_\Phi,\\
&\Sigma_{\Theta R,R}+\frac{1}{R}\Big(\Sigma_{\Theta\Phi,\Phi}+3\,\Sigma_{\Theta R}\Big)+\frac{1}{R\sin\Phi}\Big(\Sigma_{\Theta\Theta,\Theta}+2\cos\Phi\,\Sigma_{\Phi\Theta}\Big)-\\
&\qquad+B_\Theta=\rho\,\ddot{U}_\Theta.
\end{aligned}
\tag{2.47}
$$

Chapter 3

Fundamentals of periodic systems

In recent years, the propagation of waves within periodic structures has attracted increasing attention [60]. Since unusual events were discovered in a periodic structure, interest in these structures arises in several areas of science and technology due to their application.

This chapter serves as the background concepts for the study of periodic crystals. First of all, we show how to determine the irreducible Brillouin zone for different lattices and the corresponding dispersion properties. After that, we study the band structure of a thin plate.

3.1 Geometries and Brillouin zones

A Brillouin zone is a specific choice of the reciprocal lattice cell with the smallest area. It is known as the reciprocal lattice's Wigner-Seitz cell. It is constructed as the set of points enclosed area, perpendicular to a connection line from the origin to each lattice point and passing through the midpoint (bisectors). Alternatively, it is defined as the set of points closer to the origin than to any other reciprocal lattice point. The whole reciprocal space may be covered without overlap with copies of such a Brillouin zone and it is sufficient for a complete description of the waves. The construction of primitive unit cells for real and reciprocal space is given in Fig. 3.1).

We start with a 2D lattice composed of same mass particles and spaced at equal distances from one another along two lines intersecting at an arbitrary angle (see

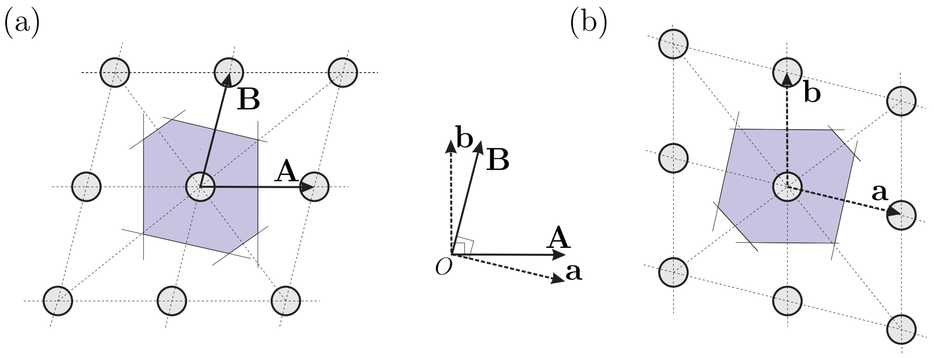

FIGURE 3.1: Construction of the Wigner-Seitz cell in (a) real and (b) reciprocal lattices. **A**, **B** and **a**, **b** are the basis vectors of the real and reciprocal lattices, respectively.

Fig. 3.1). The gray circles represents the masses. We assume that **A**, **B** are the basis vectors drawn from the origin of the real lattice, and for each real lattice vectors we define **a**, **b** as the reciprocal lattice basis vectors, which have to satisfy the condition of orthogonality, where **a** is perpendicular to **B** and **b** is perpendicular to **A**.

Let the basis vectors of direct space **A**, **B** be defined in following form

$$\mathbf{A} = 2\pi \begin{pmatrix} a \\ 0 \end{pmatrix}, \quad \mathbf{B} = 2\pi \begin{pmatrix} \alpha\, a \\ b \end{pmatrix}, \tag{3.1}$$

where α is an arbitrary number. The primitive cell vectors in 2D reciprocal lattice are defined via the following expression from the vectors of direct lattice

$$\begin{aligned} \mathbf{a} =& 2\pi \frac{\mathbf{R}\,\mathbf{B}}{\mathbf{A}\cdot\mathbf{R}\,\mathbf{B}}, \\ \mathbf{b} =& 2\pi \frac{\mathbf{R}\,\mathbf{A}}{\mathbf{B}\cdot\mathbf{R}\,\mathbf{A}}, \end{aligned} \tag{3.2}$$

where **R** is the 90 degree rotation matrix

$$\mathbf{R} = \begin{pmatrix} 0 & -1 \\ 1 & 0 \end{pmatrix}.$$

Then the basis vectors of reciprocal lattice **a**, **b** are defined

$$\mathbf{a} = \begin{pmatrix} 1/a \\ \\ -\alpha/b \end{pmatrix}, \quad \mathbf{b} = \begin{pmatrix} 0 \\ \\ 1/b \end{pmatrix}. \tag{3.3}$$

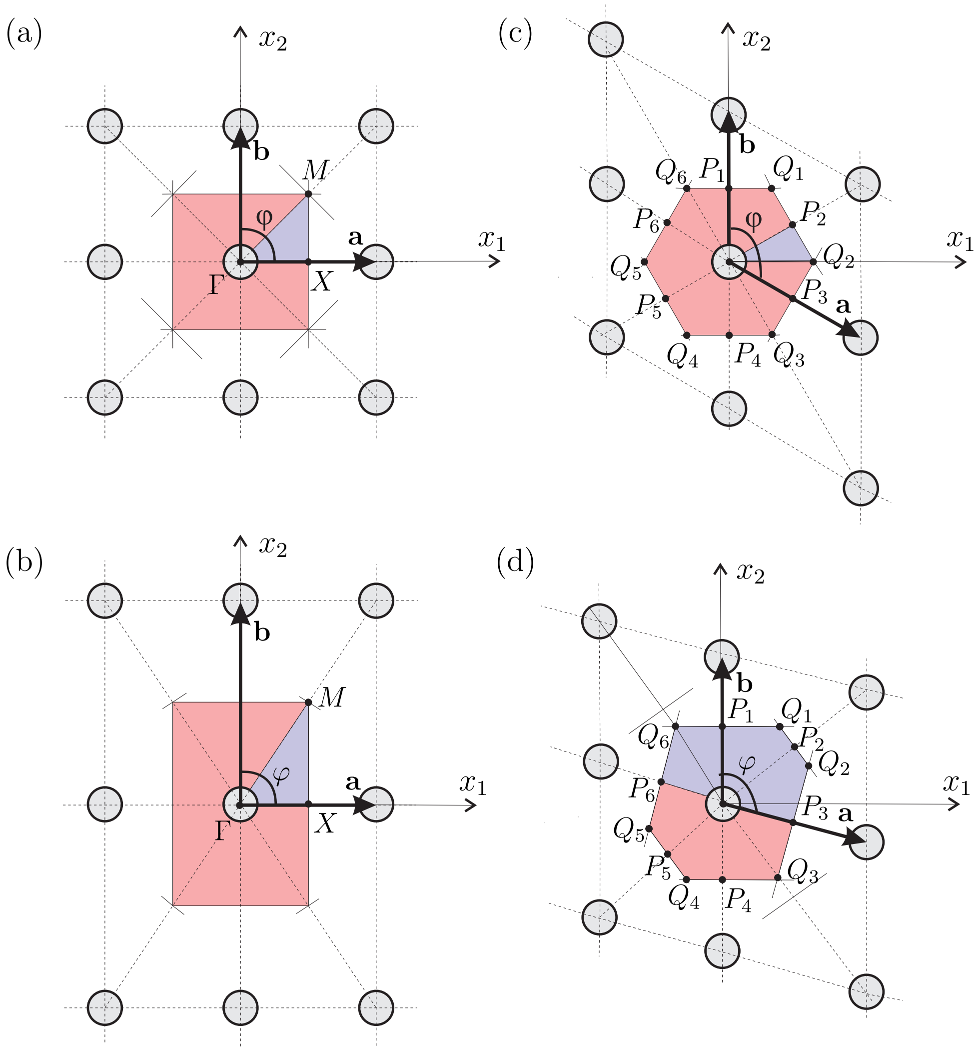

FIGURE 3.2: Brillouin zones (the red region, including the purple region) and corresponding irreducible Brillouin zones (the purple region) of following reciprocal lattices (a) $|\mathbf{a}| = |\mathbf{b}|$, $\varphi = 90°$, square lattice, (b) $|\mathbf{a}| \neq |\mathbf{b}|$, $\varphi = 90°$, rectangular lattice, (c) $|\mathbf{a}| = |\mathbf{b}|$, $\varphi = 120°$, triangular lattice, (d) $|\mathbf{a}| \neq |\mathbf{b}|$, $\varphi \neq 90°$, hexagonal lattice.

The general form of the basis vectors in the real and reciprical spaces, respectively, in the eqns. (3.1) and (3.3), depending on the values of the parameters α, a and b, can represent basis vectors for

- square lattice with $\alpha = 0$, $b = a$,
- rectangular lattice with $\alpha = 0$, $b \neq a$,
- regular hexagonal or triangular lattice with $\alpha = 0.5$, $b = \sqrt{3}a/2$,
- stretched hexagonal lattice $\alpha = 0.5$, $b \neq \sqrt{3}a/2$.

Using the properties of bisector, the coordinates of the vertices P_i of the hexagon (see Figure 3.2d) can be defined

$$\begin{gathered}
P_1\left(0;\frac{1}{2\,b}\right), \qquad P_2\left(\frac{1}{2\,a};\frac{1-\alpha}{2\,b}\right), \qquad P_3\left(\frac{1}{2\,a};-\frac{\alpha}{2\,b}\right) \\
P_4\left(0;-\frac{1}{2\,b}\right), \quad P_5\left(-\frac{1}{2\,a};-\frac{1-\alpha}{2\,b}\right), \quad P_6\left(-\frac{1}{2\,a};\frac{\alpha}{2\,b}\right)
\end{gathered} \tag{3.4}$$

and the coordinates of the point of intersection of the heights Q_i are defined as

$$\begin{aligned}
&Q_1\left(\frac{1}{2\,a}-\frac{\alpha\,a\,(1-\alpha)}{2\,b^2};\frac{1}{2\,b}\right), && Q_2\left(\frac{1}{2\,a}+\frac{\alpha\,a\,(1-\alpha)}{2\,b^2};\frac{1-2\alpha}{2\,b}\right),\\
&Q_3\left(\frac{1}{2\,a}-\frac{\alpha\,a\,(1-\alpha)}{2\,b^2};-\frac{1}{2\,b}\right), && Q_4\left(-\frac{1}{2\,a}+\frac{\alpha\,a\,(1-\alpha)}{2\,b^2};-\frac{1}{2\,b}\right),\\
&Q_5\left(-\frac{1}{2\,a}-\frac{\alpha\,a\,(1-\alpha)}{2\,b^2};-\frac{1-2\,\alpha}{2\,b}\right), && Q_6\left(-\frac{1}{2\,a}+\frac{\alpha\,a\,(1-\alpha)}{2\,b^2};\frac{1}{2\,b}\right).
\end{aligned} \tag{3.5}$$

Knowing the coordinates of the vertices of Brillouin zone, we can check the area of the first Brillouin zone and span the edge of the irreducible Brillouin zone. Area of Brillouin zone should be equal to area of a single primitive cell in the reciprocal lattice, which is given by

$$\mid \mathbf{a}\times\mathbf{b} \mid = a\,b\,\sin\varphi, \tag{3.6}$$

where φ is the angle between the reciprocal lattice basis vectors, a, b are the lengths of reciprocal lattice vectors. We will detail all possible cases in the following.

Knowing the reciprocal lattice vectors **a**, **b** in eqn. (3.3), we can easily compute the area of the first Brillouin zone

$$S_{Bz} = |\mathbf{a}\times\mathbf{b}| = \frac{1}{ab} \tag{3.7}$$

and in terms of the area of the irreducible Brillouin zone

$$S_{Bz} = 2\,S_{IBz}, \tag{3.8}$$

where $S_{IBz} = S_{P_6P_3Q_2Q_2Q_1Q_6}$ and it is the sum of the area of the triangles

$$S_{IBz} = S_{\triangle Q_6OQ_1} + S_{\triangle Q_1OQ2} + S_{\triangle OP_6Q_6} + S_{\triangle OP_3Q_2} = \frac{1}{2ab}. \tag{3.9}$$

We can notice that the area of the Brillouin zone which was defined by the formula (3.7) is equal to the area which is found by the method of coordinates (3.8).

Assume $\alpha = \dfrac{1}{2}$ hexagonal lattice stretched in the directions x_1, x_2. The coordinates of Brillouin zone (3.4), (3.5) are simplified as

$$\begin{gathered}
P_1\left(0; \frac{1}{2b}\right), \quad P_2\left(\frac{1}{2a}; \frac{1}{4b}\right), \quad P_3\left(\frac{1}{2a}; -\frac{1}{4b}\right) \quad P_4\left(0; -\frac{1}{2b}\right), \\
P_5\left(-\frac{1}{2a}; -\frac{1}{4b}\right), \quad P_6\left(-\frac{1}{2a}; \frac{1}{4b}\right), \quad Q_1\left(\frac{1}{2a} - \frac{a}{8b^2}; \frac{1}{2b}\right), \\
Q_2\left(\frac{1}{2a} + \frac{a}{8b^2}; 0\right), \quad Q_3\left(\frac{1}{2a} - \frac{a}{8b^2}; -\frac{1}{2b}\right), \quad Q_4\left(-\frac{1}{2a} + \frac{a}{8b^2}; -\frac{1}{2b}\right), \\
Q_5\left(-\frac{1}{2a} - \frac{a}{8b^2}; -\frac{1-2\alpha}{2b}\right), \quad Q_6\left(-\frac{1}{2a} + \frac{a}{8b^2}; \frac{1}{2b}\right).
\end{gathered} \tag{3.10}$$

The area of the Brillouin zone is the sum of four irreducible Brillouin zone with a shape of a rectangular trapezoid

$$S_{Bz} = 4S_{P_1Q_1Q_2O} = \frac{1}{a\,b}. \tag{3.11}$$

In case when $\alpha = \dfrac{1}{2}$, $b = \dfrac{\sqrt{3}\,a}{2}$, we obtain the regular hexagon Brillouin zone, where the coordinates P_i and Q_i are defined as

$$\begin{gathered}
P_1\left(0; \frac{1}{\sqrt{3}a}\right), \quad P_2\left(\frac{1}{2a}; \frac{1}{2\sqrt{3}a}\right), \quad P_3\left(\frac{1}{2a}; -\frac{1}{2\sqrt{3}a}\right) \\
P_4\left(0; -\frac{1}{\sqrt{3}a}\right), \quad P_5\left(-\frac{1}{2a}; -\frac{1}{2\sqrt{3}a}\right), \quad P_6\left(-\frac{1}{2a}; \frac{1}{2\sqrt{3}a}\right), \\
Q_1\left(\frac{1}{3a}; \frac{1}{\sqrt{3}a}\right), \quad Q_2\left(\frac{2}{3a}; 0\right), \quad Q_3\left(\frac{1}{3a}; -\frac{1}{\sqrt{3}a}\right), \\
Q_4\left(-\frac{1}{3a}; -\frac{1}{\sqrt{3}a}\right), \quad Q_5\left(-\frac{2}{3a}; 0\right), \quad Q_6\left(-\frac{1}{3a}; \frac{1}{\sqrt{3}a}\right).
\end{gathered} \tag{3.12}$$

And corresponding the area of Brillouin zone is defined as the sum of 12 irreducible Brillouin zones of triangular shape

$$S_{Bz} = 12 S_{\triangle P_2 Q_2 O} = 12 \cdot \frac{1}{6a^2\sqrt{3}} = \frac{2}{a^2\sqrt{3}}. \tag{3.13}$$

3.2 Periodic condition and dispersion properties

Dispersion surfaces relate wave vector to the corresponding frequency of the periodic structure. Pass band associated to the itervals of the dispersion surfaces identify a range of frequency in which wave can propagate. In the stop band range associated to the interval which are not covered by the dispersion surfaces where wave can not propagate and wave decays exponencially.Therefore pass- and stop-band analysis is very important, because it can be used to manipulate or control waves in structures.

Hexagonal lattice. The equation of motion of a hexagonal lattice with equal masses of particles, where there are six connections

$$W_{p+1,q} + W_{p-1,q} + W_{p,q+1} + W_{p,q-1} + W_{p+1,q-1} + W_{p-1,q+1} + (\tilde{\omega} - 6) W_{p,q} = 0, \tag{3.14}$$

where the p, q indices denote the position of the mass in the lattice plane, the variable $W_{p,q}$ denotes the displacement of the particle located at site (p, q) orthogonal to the lattice plane, $\tilde{\omega} = m\omega^2/\gamma$ is the frequency parameter, m is the mass, γ is the stiffness, ω is the angular frequency.

The quasi-periodicity is described by the Bloch–Floquet condition, namely

$$W_{p+l,q+n} = W_{p,q}\, e^{i(l\mathbf{a}+n\mathbf{b})\cdot\mathbf{k}}, \quad m, n \in \mathbb{Z}, \tag{3.15}$$

where $\boldsymbol{k} = k_{x_1}\mathbf{e}_1 + k_{x_2}\mathbf{e}_2$ is the wavevector or Bloch vector and $\mathbf{e}_1$, $\mathbf{e}_2$ are unit vectors.

By introducing the periodicity condition (3.15) into (3.14), we obtain the corresponding dispersion relation

$$\omega(k_{x_1}, k_{x_2}) = \sqrt{\frac{2\gamma}{m}\Big[3 - \cos(\mathbf{a}\cdot\mathbf{k}) - \cos(\mathbf{b}\cdot\mathbf{k}) - \cos((\mathbf{a}-\mathbf{b})\cdot\mathbf{k})\Big]}. \tag{3.16}$$

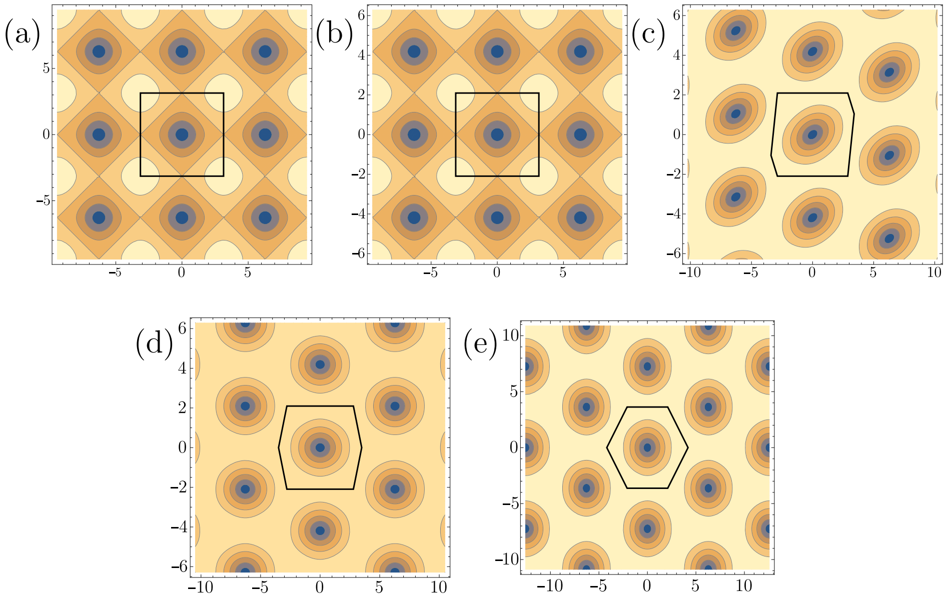

FIGURE 3.3: Contour plots of dispersion surfaces and the corresponding first Brillouin zones. (a) square, $|\boldsymbol{a}| = |\boldsymbol{b}|$, (b) rectangular, $|\boldsymbol{a}| \neq |\boldsymbol{b}|$, (c) stretched hexagonal in x_2 direction, $|\boldsymbol{a}| \neq |\boldsymbol{b}|$, $\alpha = 0.25$, (d) stretched hexagonal in x_1, x_2 directions, $|\boldsymbol{a}| \neq |\boldsymbol{b}|$, $\alpha = 0.5$, (e) regular hexagonal, $|\boldsymbol{a}| = |\boldsymbol{b}| = \sqrt{3}/2a$, $\alpha = 0.5$.

Rectangular lattice. To define a dispersion relation for the rectangular reciprocal lattice, first lets consider the equation of motion for four connections

$$W_{p+1,q} + W_{p-1,q} + W_{p,q+1} + W_{p,q-1} + (\tilde{\omega} - 4)W_{p,q} = 0. \tag{3.17}$$

By applying the Bloch-Floquet condition (3.15), we obtain dispersion relation of the rectangular lattice

$$\omega(k_{x_1}, k_{x_2}) = \sqrt{\frac{2\gamma}{m}\Big[2 - \cos(\mathbf{a}\cdot\mathbf{k}) - \cos(\mathbf{b}\cdot\mathbf{k})\Big]}. \tag{3.18}$$

Inhomogeneous lattices. Now, we assume two dimensional periodic reciprocal lattices with non equal masses. In Fig. 3.5 the open circles have mass M and the solid dots have mass m, all particles are spaced at equal distance a from one another. Then the basis lattice vectors will be given by

$$\mathbf{b} = \begin{pmatrix} 2a \\ 0 \end{pmatrix}, \quad \mathbf{c} = \begin{pmatrix} a \\ a \end{pmatrix} \tag{3.19}$$

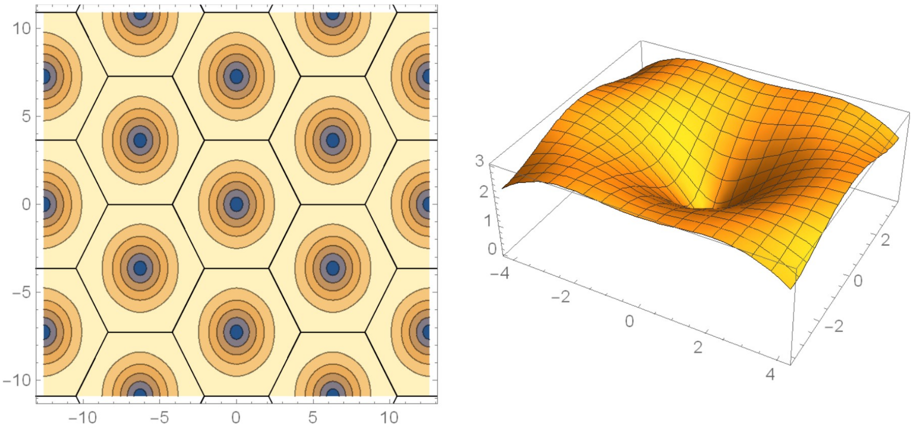

(a) (b)

Figure 3.4: The first Brillouin zone. (a) Dispersion contour plot. (b) Dispersion surface.

and equation of motion for two masses will be written as a system of scalar equations

$$\begin{aligned} v_{p+1,q} + v_{p-1,q} + v_{p,q+1} + v_{p,q-1} - 4u_{p,q} &= \frac{-M\omega^2}{\gamma} u_{p,q}, \\ u_{p+1,q} + u_{p-1,q} + u_{p,q+1} + u_{p,q-1} - 4v_{p,q} &= \frac{-m\omega^2}{\gamma} v_{p,q}, \end{aligned} \tag{3.20}$$

where $u_{p,q}$, $v_{p,q}$ are displacements of the particles with masses M and m, respectively.

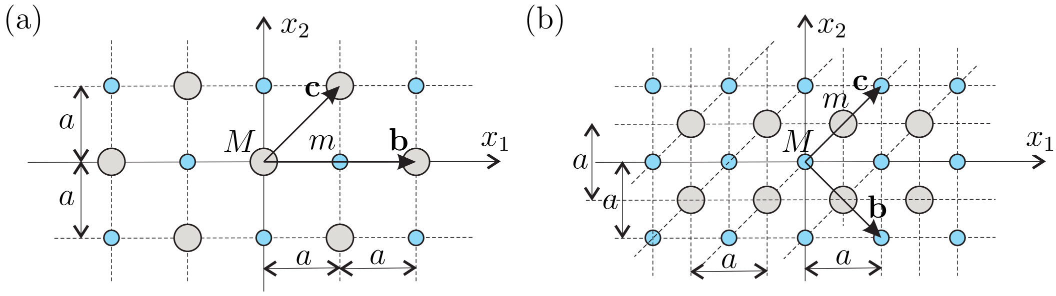

Figure 3.5: Inhomogeneous 2D lattices with two different masses

Bloch-Floquet conditions, describing the motion of the masses M and m, are written by

$$\begin{aligned} u_{p+l,q+n} &= u_{p,q} \exp[i(l\,\mathbf{b} + n\,\mathbf{c}) \cdot \mathbf{k}], \\ v_{p+l,q+n} &= v_{p,q} \exp[i(l\,\mathbf{b} + n\,\mathbf{c}) \cdot \mathbf{k}]. \end{aligned} \tag{3.21}$$

Substituting these expressions in the equations of motion (3.20) and using the relation $\exp[i\mathbf{s}\cdot\mathbf{k}]+\exp[-i\mathbf{s}\cdot\mathbf{k}]=2\,\cos(\mathbf{s}\cdot\mathbf{k})$, we obtain two linear equations in $u_{p,q}$ and $v_{p,q}$

$$\begin{aligned} u_{p,q}\Big(\frac{M\omega^2}{\gamma}-4\Big)+2v_{p,q}\Big(\cos(\mathbf{b}\cdot\mathbf{k})+\cos(\mathbf{c}\cdot\mathbf{k})\Big)&=0,\\ 2u_{p,q}\Big(\cos(\mathbf{b}\cdot\mathbf{k})+\cos(\mathbf{c}\cdot\mathbf{k})\Big)+v_{p,q}\Big(\frac{m\omega^2}{\gamma}-4\Big)&=0. \end{aligned} \tag{3.22}$$

To get the nontrivial solutions for $u_{p,q}$ and $v_{p,q}$, determinant of the coefficients of $u_{p,q}$ and $v_{p,q}$ should be equal to zero. This condition gives us the dispersion relation between radian frequency ω and wavevector $\mathbf{k}$

$$\omega^4-4\gamma\Big(\frac{1}{M}+\frac{1}{m}\Big)\omega^2+\frac{16\gamma^2}{Mm}-\frac{4\gamma^2}{Mm}\Big(\cos(\mathbf{b}\cdot\mathbf{k})+\cos(\mathbf{c}\cdot\mathbf{k})\Big)^2=0 \tag{3.23}$$

and solving the biquadratic equation, we get 4 roots, which are given in Fig. 3.6a. But we know that the frequency must be positive, so instead of four we will take only two branches (see Fig.3.6b)

$$\omega^2=\frac{2\gamma}{Mm}\left[M+m\pm\sqrt{(M+m)^2-4Mm+Mm\Big(\cos(\mathbf{b}\cdot\mathbf{k})+\cos(\mathbf{c}\cdot\mathbf{k})\Big)^2}\right]. \tag{3.24}$$

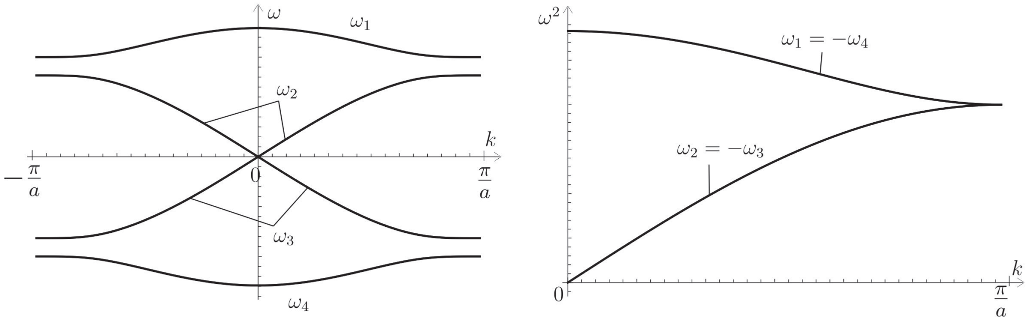

(a) (b)

FIGURE 3.6: Dispersion curves along the ΓX in the Brillouin zone. (a) $M\neq m$, $-\pi/a\leq k\leq\pi/a$, (b) symmetric part, $M=m$, $0\leq k\leq\pi/a$.

When $M=m$ the two branches join at $k\,a=\pi$, the periodicity is doubled, namely $k\,a=2\,\pi$, and the dispersion curve is simply reflected at $k\,a=\pi$.

Repeating the previous procedure, the dispersion relation for the hexagonal lattice with different masses (see Fig.3.5b) reduces to

$$\omega^4+\frac{2\gamma(M+m)}{Mm}\Big[\cos(\mathbf{b}\cdot\mathbf{k})-3\Big]\omega^2+\frac{4\gamma^2}{Mm}\Big[\Big(\cos(\mathbf{b}\cdot\mathbf{k})-3\Big)^2-\Big(\cos(\mathbf{b}\cdot\mathbf{k})+\cos(\mathbf{c}\cdot\mathbf{k})\Big)^2\Big]=0. \tag{3.25}$$

The solution is

$$\omega^2=\frac{\gamma}{Mm}\Bigg(\Big(M+m\Big)\Big(3-\cos(\mathbf{b}\cdot\mathbf{k})\Big)\pm \sqrt{\Big(M+m\Big)^2\Big(3-\cos(\mathbf{b}\cdot\mathbf{k})\Big)^2-4Mm\Big((\cos(\mathbf{b}\cdot\mathbf{k})-3)^2-\Big(\cos(\mathbf{b}\cdot\mathbf{k})+\cos(\mathbf{c}\cdot\mathbf{k})\Big)^2\Big)}\Bigg). \tag{3.26}$$

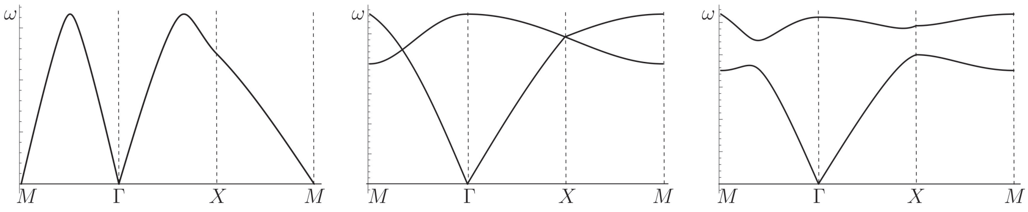

(a) (b) (c)

FIGURE 3.7: Dispersion curves of the irreducible Brillouin zone. (a) The four interactions, (b) $M=m$, the six interactions, (c) $M\neq m$, the six interactions.

3.3 Platonic crystal

Platonic crystals are periodic structures designed to manipulate flexural waves within elastic plates. Wave propagation in a thin plate governed by a partial differential equation of the fourth-order, the biharmonic equation in the time-harmonic regime,as opposed to equations is second-order for other types of crystals.

In this section, we introduce the semi-analytical multipole expansion and the derivation of the dispersion properties for platonic crystals.

3.3.1 Governing equation

We consider flexural vibration in a thin plate. The plate has thickness h, bending stiffness $B = Eh^3/(12(1-v^2))$, with E the Young's modulus and v the Poisson's ratio, and density ρ [61].

Time-harmonic regime is considered and the time dependence $e^{-i\omega t}$, with ω the radian frequency, is neglected in the following for simplicity. Transverse displacement is $W(\mathbf{X})$, where $\mathbf{X} = (X_1, X_2)$. Rotation is the vector $\nabla W(\mathbf{X})$ and curvature is the tensor $\chi(\mathbf{X}) = \nabla\nabla W(\mathbf{X})$. The static quantities are the beding moment symmetric tensor $\mathbf{M}(\mathbf{X})$ and the shear force vector $\mathrm{V}(\mathbf{X})=\nabla\cdot\mathbf{M}(\mathbf{X})$. The constitutive relation between the bending moment tensor $\mathbf{M}(\mathbf{X})$ and the curvature $\chi(\mathbf{X})$ is given by [77]

$$\mathbf{M}(\mathbf{X}) = -\mathbb{D}^{(0)}\chi(\mathbf{X}) \tag{3.27}$$

where, for isotropic plates, the constitive tensor $\mathbb{D}^{(0)}$ has components

$$D^{(0)}_{ijkl} = B\Big[\delta_{ij}\delta_{kl} + \frac{1-v}{2}(\delta_{ik}\delta_{jl} + \delta_{il}\delta_{jk})\Big], \tag{3.28}$$

where δ_{ij} is the Kronecker delta and $i, j, k, l = 1, 2$. Explicitly, for an isotropic and homogeneous plate, the moment-curvature relations are

$$\begin{aligned} M_{11} &= -B\Big(\frac{d^2W}{dX_1^2} + v\frac{d^2W}{dX_2^2}\Big), \\ M_{22} &= -B\Big(\frac{d^2W}{dX_2^2} + v\frac{d^2W}{dX_1^2}\Big), \\ M_{12} &= -B(1-v)\frac{d^2W}{dX_1 dX_2}, \end{aligned} \tag{3.29}$$

where M_{ij} are the components of the moment tensor. Then, the equation of motion for the plate has the form

$$\nabla\cdot[\nabla\cdot\mathbf{M}(\mathbf{X})] + \rho h\omega^2 W(\mathbf{X}) = \nabla\cdot\mathbf{V}(\mathbf{X}) + \rho h\omega^2 W(\mathbf{X}) = 0, \tag{3.30}$$

which, in the isotropic case, simplifies to the well-known bi-harmonic form

$$(\Delta^4 - \beta^4)W(\mathbf{X}) = (\Delta^2 + \beta^2)(\Delta^2 - \beta^2)W(\mathbf{X}) = 0, \tag{3.31}$$

where $\beta = \sqrt[4]{\omega^2\rho\, h/B}$ is the frequency parameter.

The general solution of the above equation admits the representation

$$W(\mathbf{X}) = W^{(1)}(\mathbf{X}) + W^{(2)}(\mathbf{X}), \tag{3.32}$$

where $W^{(1)}$ and $W^{(2)}$ satisfy the Helmholtz and modified Helmholtz equations

$$\begin{aligned}(\Delta^2 + \beta^2)W^{(1)}(\mathbf{X}) &= 0,\\ (\Delta^2 - \beta^2)W^{(2)}(\mathbf{X}) &= 0.\end{aligned}$$

In polar cylindrical coordinates R, Θ, which are associated with Cartesian as $X_1 = R\cos\Theta$, $X_2 = R\sin\Theta$, we use the series representation

$$W(R,\Theta) = \sum_{n=-\infty}^{\infty} W_n(R)e^{in\Theta}, \tag{3.33}$$

where W_n is defined as

$$W_n(R) = A_n J_n(\beta R) + B_n H_n^{(1)}(\beta R) + C_n I_n(\beta R) + D_n K_n(\beta R). \tag{3.34}$$

In eqn. (3.34) J_n is the first kind of Bessel function, $H_n^{(1)}$ is the first kind of Hankel function, I_n, K_n are the first and second kind of modified Bessel functions and A_n, B_n, C_n, D_n are unknown constants to be determined from the boundary and quasi-periodicity conditions.

3.3.2 Boundary conditions

We consider two types of boundary conditions on the hole of radius $R = R_1$ [51]

I. Clamped boundary conditions.

Consider a plate, which is completely clamped along the hole in it. Clamped boundary condition on $R = R_1$ is expressed as

$$\begin{aligned} W\Big|_{R=R_1} &= 0,\\ \frac{\partial W}{\partial r}\Big|_{R=R_1} &= 0. \end{aligned} \tag{3.35}$$

which corresponds to zero transverse displacement and zero rotation along the hole. Substituting the general solution (3.34) into the above equations, we obtain

$$\begin{aligned} &A_n J_n(\beta R_1) + B_n H_n^{(1)}(\beta R_1) + C_n I_n(\beta R_1) + D_n K_n(\beta R_1) = 0, \\ &A_n J_n'(\beta R_1) + B_n H_n^{(1)'}(\beta R_1) + C_n I_n'(\beta R_1) + D_n K_n'(\beta R_1) = 0. \end{aligned} \tag{3.36}$$

II. Free boundary conditions.

We impose free boundary conditions on radial components of the moment and the transverse force for an inclusion of radius R_1, which correspond to vanishing bending moment M_R and shearing stress at the edges of the inclusion [78]

$$\begin{aligned} M_R\Big|_{R=R_1} &= 0, \\ \left(V_R - \frac{1}{R}\frac{\partial M_{R\Theta}}{\partial \Theta}\right)\Bigg|_{R=R_1} &= 0, \end{aligned} \tag{3.37}$$

where M_R the bending moment, V_R the transverse shearing force and $M_{R\Theta}$ the twisting moment are defined as

$$\begin{aligned} M_R &= -B\left[\frac{\partial^2 W}{\partial R^2} + v\left(\frac{1}{R}\frac{\partial W}{\partial R} + \frac{1}{R^2}\frac{\partial^2 W}{\partial \Theta^2}\right)\right], \\ V_R &= -B\frac{\partial}{\partial R}\left[\frac{\partial^2 W}{\partial R^2} + \frac{1}{R}\frac{\partial W}{\partial R} + \frac{1}{R^2}\frac{\partial^2 W}{\partial \Theta^2}\right], \\ M_{R\Theta} &= B(1-v)\left[\frac{1}{R}\frac{\partial^2 W}{\partial R \partial \Theta} - \frac{1}{R^2}\frac{\partial W}{\partial \Theta}\right]. \end{aligned}$$

3.3.3 Bloch-Floquet condition. Dispersion properties

Now consider a doubly periodic infinite array of holes with radii R_1, which are arranged in a square lattice of period d.

The Bloch-Floquet quasi-periodicity conditions

$$W(\mathbf{X} + \mathbf{R}_q) = W(\mathbf{X})\, e^{i\mathbf{R}_q \cdot \mathbf{k}}, \tag{3.38}$$

where $\mathbf{X} = (X_1, X_2)$, for the case of a square lattice $\mathbf{R}_q = q_1\, d\, \mathbf{e}_1 + q_2\, d\, \mathbf{e}_2$ represent the position of holes, $q = \{q_1, q_2\}$ is multi-index, $\mathbf{k}$ is the Bloch vector, $\mathbf{e}_1$, $\mathbf{e}_2$ are unit vectors and d dimension of unit cell.

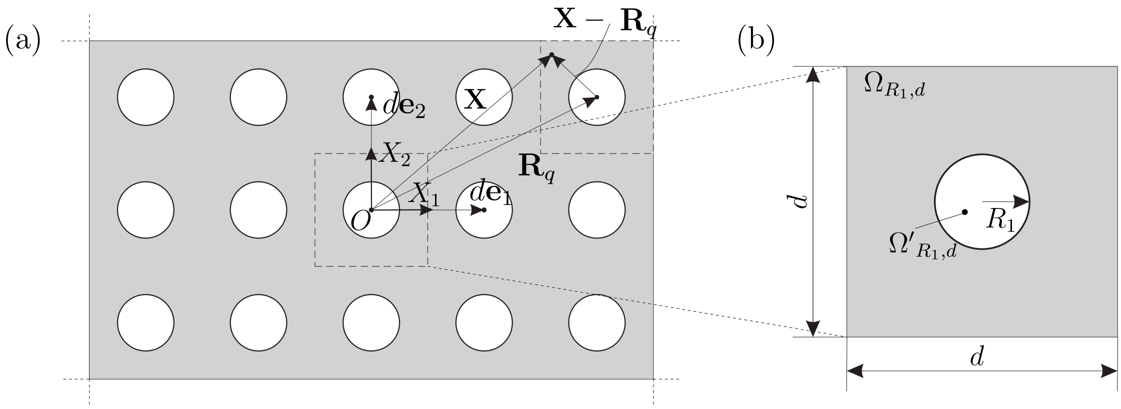

FIGURE 3.8: Outline of a doubly periodic perforated domain with holes R_1 in Cartesian space (X_1, X_2) (a) and (b) unit cell with dimension d.

Quasi-periodicity condition are introduced by the Rayleigh identities for W_1 and W_2 [50, 52, 78], that lead to two relations between A_n and B_l and C_n and D_l as follows

$$\begin{aligned} A_n &= \sum_{l=-\infty}^{\infty} (-1)^{l-n} S^H_{l-n}(\beta, \mathbf{k}) B_l, \\ C_n &= \sum_{l=-\infty}^{\infty} (-1)^{l} S^K_{l-n}(\beta, \mathbf{k}) D_l. \end{aligned} \tag{3.39}$$

The lattice sums, which satisfy the Helmholtz and modified Helmholtz equations, are defined as

$$\begin{aligned} S^H_l(\beta, \mathbf{k}) &= \sum_{q \neq 0,0} H^{(1)}_l(\beta R_q) e^{il\theta_q} e^{i\mathbf{k}\mathbf{R}_q}, \\ S^K_l(\beta, \mathbf{k}) &= \sum_{q \neq 0,0} K_l(\beta R_q) e^{il\theta_q} e^{i\mathbf{k}\mathbf{R}_q}. \end{aligned} \tag{3.40}$$

Substituting the general solution (3.33) using the relations (3.39) into the clamped

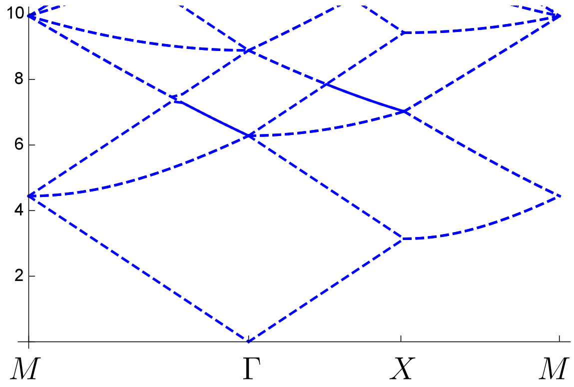

FIGURE 3.9: Dispersion diagram of homogeneous plate

boundary conditions (3.35) allows us to obtain

$$\begin{aligned}&\sum_{l=-\infty}^{\infty}\Big((-1)^{l-n}S^{H}_{l-n}J_n(\beta R_1)+\delta_{ln}H^{(1)}_n(\beta R_1)\Big)B_l+\\&\qquad+\sum_{l=-\infty}^{\infty}\Big((-1)^{l-n}S^{K}_{l-n}I_n(\beta R_1)+\delta_{ln}K_n(\beta R_1)\Big)D_l=0,\\&\sum_{l=-\infty}^{\infty}\Big((-1)^{l-n}S^{H}_{l-n}J'_n(\beta R_1)+\delta_{ln}H^{(1)'}_n(\beta R_1)\Big)B_l+\\&\qquad+\sum_{l=-\infty}^{\infty}\Big((-1)^{l-n}S^{K}_{l-n}I'_n(\beta R_1)+\delta_{ln}K'_n(\beta R_1)\Big)D_l=0\end{aligned}\tag{3.41}$$

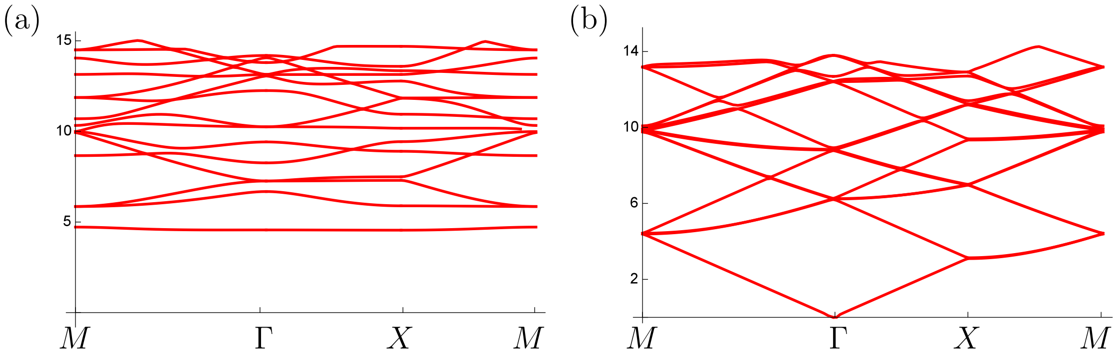

FIGURE 3.10: Dispersion curves of perforated plates with radius $R_1/d = 0.1$ (a) clamped, (b) free boundary conditions. The truncation number is $N = 15$.

and, for free boundary conditions (3.37)

$$\begin{aligned}
&\sum_{l=-\infty}^{\infty}\Bigg[(-1)^{l-n}S^{H}_{l-n}\Big((1-v)\beta R_1 J_n'(\beta R_1)-\Big((1-v)n^2-\beta^2R_1^2\Big)J_n(\beta R_1)\Big)+\\
&+\delta_{ln}\Big((1-v)\beta R_1 H_n^{(1)'}(\beta R_1)-\Big((1-v)n^2-\beta^2R_1^2\Big)H_n^{(1)}(\beta R_1)\Big)\Bigg]B_l+\\
&+\sum_{l=-\infty}^{\infty}\Bigg[(-1)^{l}S^{K}_{l-n}\Big((1-v)\beta R_1 I_n'(\beta R_1)-\Big((1-v)n^2+\beta^2R_1^2\Big)I_n(\beta R_1)\Big)+\\
&+\delta_{ln}\Big((1-v)\beta R_1 K_n'(\beta R_1)-\Big((1-v)n^2+\beta^2R_1\Big)K_n(\beta R_1)\Big)\Bigg]D_l=0,
\end{aligned}$$

$$\begin{aligned}
&\sum_{l=-\infty}^{\infty}\Bigg[(-1)^{l-n}S^{H}_{l-n}\Big((1-v)n^2 J_n(\beta R_1)-\Big(\beta^3R_1^3+(3-v)n^2\beta R_1\Big)J_n'(\beta R_1)\Big)+\\
&+\delta_{ln}\Big((1-v)n^2 H_n^{(1)}(\beta R_1)-\Big(\beta^3R_1^3+(3-v)n^2\beta R_1\Big)H_n^{(1)'}(\beta R_1)\Big)\Bigg]B_l+\\
&+\sum_{l=-\infty}^{\infty}\Bigg[(-1)^{l}S^{K}_{l-n}\Big((1-v)n^2 I_n(\beta R_1)+\Big(\beta^3R_1^3-(1-v)n^2\beta R_1\Big)I_n'(\beta R_1)\Big)+\\
&+\delta_{ln}\Big((1-v)n^2 K_n(\beta R_1)+(\beta^3R_1^3-(1-v)n^2\beta R_1\Big)K_n'(\beta R_1)\Big)\Bigg]D_l=0.
\end{aligned} \tag{3.42}$$

The above eqns. (3.42) are an homogeneous system in the unknown variables B_l and D_l of infinite dimension. The convergent form of lattice sums S_l^Y, S_l^K are given in [50, 79–81], namely

$$\begin{aligned}
S_l^Y=&\frac{1}{J_{l+3}(\beta\lambda)}\Bigg(-\Bigg[Y_3(\beta\lambda)+\frac{1}{\pi}\sum_{n=1}^{3}\frac{(3-n)!}{(n-1)!}\Big(\frac{2}{\beta\lambda}\Big)^{3-2n+2}\Bigg]\delta_{l,0}\Bigg)-\\
&-\frac{4i^l}{d^2}\sum_p\Big(\frac{\beta}{Q_p}\Big)^3\frac{J_{l+3}(Q_p\lambda)}{Q_p^2-\beta^2}e^{il\theta_p}\Bigg),\\
S_l^K=&\frac{1}{I_{l+3}(\beta\lambda)}\Bigg(\Bigg[K_3(\beta\lambda)-\frac{8}{(\beta\lambda)^3}+\frac{1}{\beta\lambda}-\frac{\beta\lambda}{8}\Bigg]\delta_{l,0}+\\
&+\frac{2\pi i^l}{d^2}\sum_p\Big(\frac{\beta}{Q_p}\Big)^3\frac{J_{l+3}(Q_p\lambda)}{Q_p^2+\beta^2}e^{il\theta_p}\Bigg).
\end{aligned} \tag{3.43}$$

Then by truncating the above systems at ±N for indices l and n, we can obtain the finite linear homogeneous system

$$\mathbf{M}(\beta, \mathbf{k}) \begin{pmatrix} \mathbf{B} \\ \mathbf{D} \end{pmatrix} = \mathbf{0} \tag{3.44}$$

and non-trivial solutions correspond to zeros of the determinant of the matrix $\mathbf{M}$ with dimension $4N+2$ by $4N+2$

$$\det[\mathbf{M}(\beta, \mathbf{k})] = 0. \tag{3.45}$$

Note that the process to find zeros of the dispersion equation (3.45) can be difficult. If $\mathbf{k}$ is near the singularity of lattice sums, exposing false roots. The singularities correspond to the dispersion diagram of homogeneous square plate that is shown in Figure 3.9. For computation, we use Meylan's algorithm in complex plane of frequency [82]. In Figure 3.10, we provide the converged dispersion properties of a perforated thin plate with $R_1/d = 0.1$, $\nu = 0.3$ for clamped (3.41) and Free (3.42) boundary conditions.

Chapter 4

Two-dimensional problems. Out of plane shear waves

In this chapter, we give the governing equations of motion for out of plane shear waves, describe the geometric transformations in Cartesian and cylindrical coordinate systems, perform eigenfrequency analyses and provide asymptotic formulations, finally, we describe the analytical and semi-analytical solutions of some transmission and scattering problems. The classical analytical solutions reported in this Chapter has been used to validate the numerical implementation in Comsol.

4.1 Governing equations

The form-invariance of the Helmholtz equation under the geometric transformations allows us to consider wave propagation in a transformed system as propagation in an untransformed coordinate system with a certain functional distribution of the shear modulus μ and density ρ.

4.1.1 Cartesian coordinate

Here, we give the coordinate transformations and the governing equations in Cartesian coordinate systems.

We focus on out of plane shear waves, where the displacement is $\mathbf{U} = (0, 0, U_3(\mathbf{X}, t))^T$ and the position vector in the original untransformed domain is defined as $\mathbf{X} =$

$(X_1 \;\; X_2 \;\; 0)^T$. Wave propagation in a linear elastic medium is governed by [61, 83]

$$\nabla_{\mathbf{X}} \cdot \mathbf{C}^{(0)} \nabla_{\mathbf{X}} U_3(\mathbf{X}, t) - \rho_0 \ddot{U}_3(\mathbf{X}, t) = 0, \tag{4.1}$$

where $\mathbf{C}^{(0)}$ is the second-order stiffness tensor for out of plane motion, ρ_0 the density and $\nabla_{\mathbf{X}}$ the gradient operator in the original domain.

In the transformed domain the governing eqn. (4.1) is mapped into

$$\nabla \cdot \mathbf{C} \nabla u_3(\mathbf{x}, t) - \rho \, \ddot{u}_3(\mathbf{x}, t) = 0, \tag{4.2}$$

where $u_3(\mathbf{x}, t)$ is the transformed displacement, that we assume equal to $U_3(\mathbf{X}, t)$. In addition, $\mathbf{x} = (x_1 \;\; x_2 \;\; 0)^T$ is the transformed domain and the corresponding gradient operator is ∇, ρ and $\mathbf{C}$ the transformed density and stiffness tensor, respectively.

4.1.1.1 Equation of motion

We consider the out of plane displacement distribution in homogeneous, isotropic untransformed domain, where the displacement field is described by $\mathbf{U} = \mathbf{U}(\mathbf{X}, t) = (U_1, U_2, U_3)^T$, where $U_1 = 0$, $U_2 = 0$ and $U_3 = U_3(X_1, X_2, t)$. The corresponding non zero stresses are the shear components

$$\Sigma_{31} = \mu_0 \frac{\partial U_3}{\partial X_1}, \quad \Sigma_{32} = \mu_0 \frac{\partial U_3}{\partial X_2}. \tag{4.3}$$

Then the Navier equation (2.15) is reduced to the scalar wave equation

$$\mu_0 \Delta U_3 - \rho_0 \ddot{U}_3 = 0. \tag{4.4}$$

In the time-harmonic regime, the displacement is described by $U_3 = U(X_1, X_2)\, e^{-i\omega t}$ with ω the radian frequency and t the time, the eqn. (4.4) satisfies

$$\frac{\partial^2 U}{\partial X_1^2} + \frac{\partial^2 U}{\partial X_2^2} + \beta^2 U = 0, \tag{4.5}$$

where $\beta^2 = \dfrac{\rho_0 \, \omega^2}{\mu_0}$ and μ_0, ρ_0 are untransformed homogeneous, isotropic linear elastic the shear modulus and density, respectively, of the material.

4.1.1.2 Transformed equation

We introduce the coordinate transformations $\mathbf{X} = \mathcal{F}(\mathbf{x})$ from the original coordinate $\mathbf{X} = (X_1, X_2)$ to the transformed one $\mathbf{x} = (x_1, x_2)$ and the inverse transformations of the coordinate $\mathbf{x} = \mathcal{F}^{-1}(\mathbf{X})$.

I. Now, introduce a geometric transformation $\mathcal{F}^{-1}(\mathbf{X})$, which transform the small square $\Omega_0^{(0)} = \{\mathbf{X} :\mid X_1 \mid< \epsilon, \mid X_2 \mid< \epsilon\}$ into the square $\Omega_0 = \{\mathbf{x} :\mid x_1 \mid< a, \mid x_2 \mid< a\}$ domain [32, 38], with $\epsilon \ll a$,

$$\left.\begin{aligned} x_1 &= \alpha_1 X_1 + \alpha_2 \\ x_2 &= \alpha_1 X_2 + \alpha_2 X_2/X_1 \end{aligned}\right\} \text{ in } \Omega_1, \qquad \left.\begin{aligned} x_1 &= \alpha_1 X_1 + \alpha_2 X_1/X_2 \\ x_2 &= \alpha_1 X_2 + \alpha_2 \end{aligned}\right\} \text{ in } \Omega_2,$$
$$\left.\begin{aligned} x_1 &= \alpha_1 X_1 - \alpha_2 \\ x_2 &= \alpha_1 X_2 - \alpha_2 X_2/X_1 \end{aligned}\right\} \text{ in } \Omega_3, \qquad \left.\begin{aligned} x_1 &= \alpha_1 X_1 - \alpha_2 X_1/X_2 \\ x_2 &= \alpha_1 X_2 - \alpha_2 \end{aligned}\right\} \text{ in } \Omega_4, \tag{4.6}$$

where $\alpha_1 = b/(a + b - \epsilon)$, $\alpha_2 = (a + b)(a - \epsilon)/(a + b - \epsilon)$ and b is the width of cloak. Accordingly, the deformation gradient $\mathbf{F}$ and the Jacobian J in cartesian coordinate system are given by

$$\mathbf{F} = \begin{bmatrix} \frac{\partial x_1}{\partial X_1} & \frac{\partial x_1}{\partial X_2} \\ \frac{\partial x_2}{\partial X_1} & \frac{\partial x_2}{\partial X_2}, \end{bmatrix}, \quad J = \det \mathbf{F}, \tag{4.7}$$

for each trapezoid region they are defined as

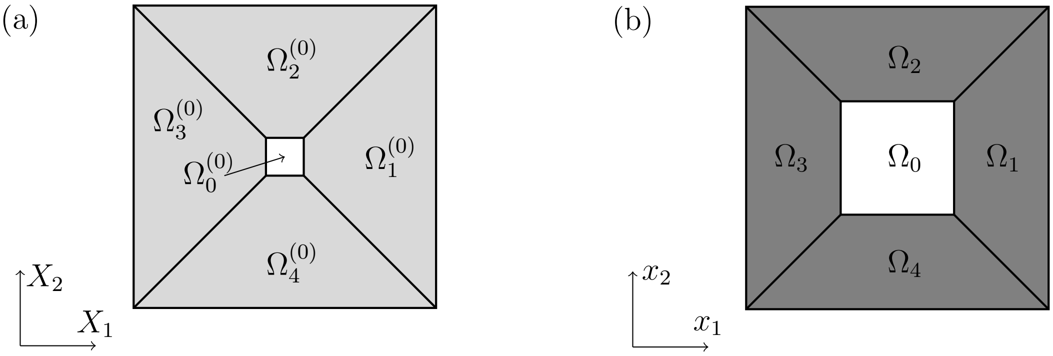

FIGURE 4.1: Geometric transformation of the (a) untransformed homogeneous, isotropic trapezoids $\Omega_1^{(0)}$,$\Omega_2^{(0)}$, $\Omega_3^{(0)}$, $\Omega_4^{(0)}$ with square inclusion $\Omega_0^{(0)}$ into the (b) inhomogeneous, anisotropic deformed trapezoids Ω_1,Ω_2, Ω_3, Ω_4 with the cloaked square Ω_0.

$$
\begin{aligned}
\mathbf{F}_{\Omega_1} &= \begin{bmatrix} \alpha_1 & 0 \\ \dfrac{\alpha_1\alpha_2 x_2}{x_1(\alpha_2 - x_1)} & \dfrac{\alpha_1 x_1}{x_1 - \alpha_2} \end{bmatrix}, \quad J_{\Omega_1} = \det \mathbf{F}_{\Omega_1} = \frac{\alpha_1^2 x_1}{x_1 - \alpha_2}, \\
\mathbf{F}_{\Omega_2} &= \begin{bmatrix} \dfrac{\alpha_1 x_2}{x_2 - \alpha_2} & \dfrac{\alpha_1\alpha_2 x_1}{x_2(\alpha_2 - x_2)} \\ \alpha_1 & 0 \end{bmatrix}, \quad J_{\Omega_2} = \det \mathbf{F}_{\Omega_2} = \frac{\alpha_1^2 x_2}{x_2 - \alpha_2}, \\
\mathbf{F}_{\Omega_3} &= \begin{bmatrix} \alpha_1 & 0 \\ \dfrac{\alpha_1\alpha_2 x_2}{x_1(\alpha_2 + x_1)} & \dfrac{\alpha_1 x_1}{x_1 + \alpha_2} \end{bmatrix}, \quad J_{\Omega_3} = \det \mathbf{F}_{\Omega_3} = \frac{\alpha_1^2 x_1}{x_1 + \alpha_2}, \\
\mathbf{F}_{\Omega_4} &= \begin{bmatrix} \alpha_1 & 0 \\ \dfrac{\alpha_1 x_2}{x_2 + \alpha_2} & \dfrac{\alpha_1\alpha_2 x_1}{x_2(\alpha_2 + x_2)} \end{bmatrix}, \quad J_{\Omega_4} = \det \mathbf{F}_{\Omega_4} = \frac{\alpha_1^2 x_2}{x_2 + \alpha_2}.
\end{aligned} \tag{4.8}
$$

Then, the original equation of motion (4.5) for untransformed regions $\Omega_i^{(0)}$ can be written in deformed coordinates $\mathbf{x}$ for each transformed regions Ω_i, where $i = 1, 2, 3, 4$, as

$$
\nabla \cdot \left(\frac{1}{J_{\Omega_i}} \mathbf{F}_{\Omega_i} \mathbf{C}^{(0)} \mathbf{F}_{\Omega_i}^T \nabla u(x_1, x_2) \right) + \frac{\beta^2}{J_{\Omega_i}} u(x_1, x_2) = 0, \tag{4.9}
$$

where anisotropic stiffness tensors are $\mathbf{C}_{\Omega_i} = \left(\mathbf{F}_{\Omega_i} \mathbf{C}^{(0)} \mathbf{F}_{\Omega_i}^T \right) / J_{\Omega_i}$ and densities are $\rho = \rho_0 / J_{\Omega_i}$.

The expanded form of transformed equation of motion (4.9) for $i = 1$ is

$$
\frac{x_1 - \alpha_2}{x_1} \frac{\partial^2 u}{\partial x_1^2} - \frac{2\alpha_2 x_2}{x_1^2} \frac{\partial^2 u}{\partial x_1 \partial x_2} + \frac{x_1^4 + \alpha_2^2 x_2^2}{x_1^3 (x_1 - \alpha_2)} \frac{\partial^2 u}{\partial x_2^2} + \frac{2\alpha_2 x_2}{x_1^2 (x_1 - \alpha_2)} \frac{\partial u}{\partial x_2} + \frac{\beta^2 (x_1 - \alpha_2)}{\alpha_1^2 \mu_0 x_1} u = 0. \tag{4.10}
$$

Note that the identity gauge has been considered $\mathbf{u}(\mathbf{x}) = \mathbf{U}(\mathbf{X})$. In Figure 4.2 the displacement field generated by an external source without and with the cloak region is shown. The Green's function is derived and shown in Appendix B. Figure 4.2b shows the field when the void is surrounded by the transformation-based trapezoid domains, constructed as described above. It is observed that outside the cloaked region, the cloaked field and unperturbed field are almost coincident, while in Figure 4.2a the field is reflected by the cavity. In order to strongly absorb outgoing waves from the interior of a computational region without reflecting them back into the interior domain, we impose Perfectly Matched Layer (PML) around the computational domain (see Appendix A).

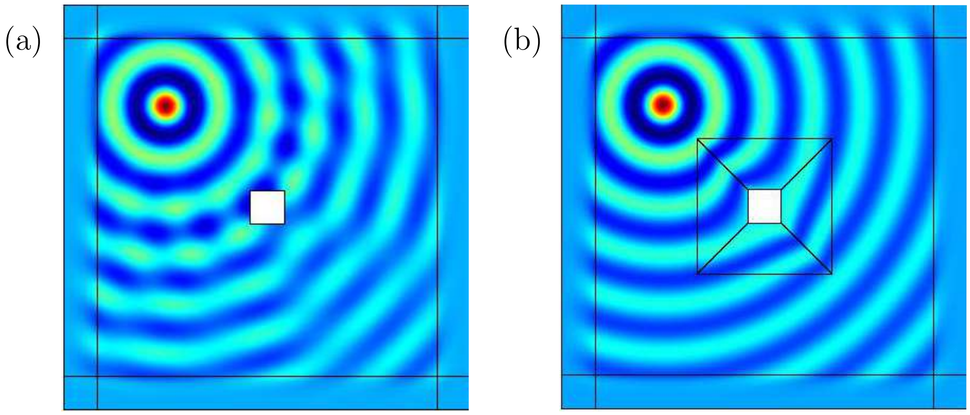

FIGURE 4.2: The displacement field generated by an external source in the presence of (a) an uncloaked and (b) cloaked square cavities.

II. Now, we consider a geometric transformation, which maps the inclined square inclusion $\Omega_0^{(0)} = \{\mathbf{X} :| X_1 |< \epsilon/\sqrt{2}, | X_2 |< \epsilon/\sqrt{2}\}$ into the square inclusion $\Omega_0 = \{\mathbf{x} :| x_1 |< a/\sqrt{2}, | x_2 |< a/\sqrt{2}\}$. Coordinate transformations for each triangle domain Ω_i in Figure 4.3 are expressed as

$$\left.\begin{aligned} x_1 &= \alpha_1 X_1 \\ x_2 &= X_2 \end{aligned}\right\} \text{ in } \Omega_1, \qquad \left.\begin{aligned} x_1 &= \alpha_2 X_1 \\ x_2 &= X_2 - \alpha_2 X_1 \end{aligned}\right\} \text{ in } \Omega_2,$$
$$\left.\begin{aligned} x_1 &= X_1 \\ x_2 &= \alpha_1 X_2 \end{aligned}\right\} \text{ in } \Omega_3, \qquad \left.\begin{aligned} x_1 &= \alpha_2 X_1 \\ x_2 &= X_2 + \alpha_2 X_1 \end{aligned}\right\} \text{ in } \Omega_4, \tag{4.11}$$

where $\alpha_1 = (c - \sqrt{2}\, a)/(c - \sqrt{2}\, \epsilon)$, $\alpha_2 = a/\,\epsilon$, c is the length of cloak and using the

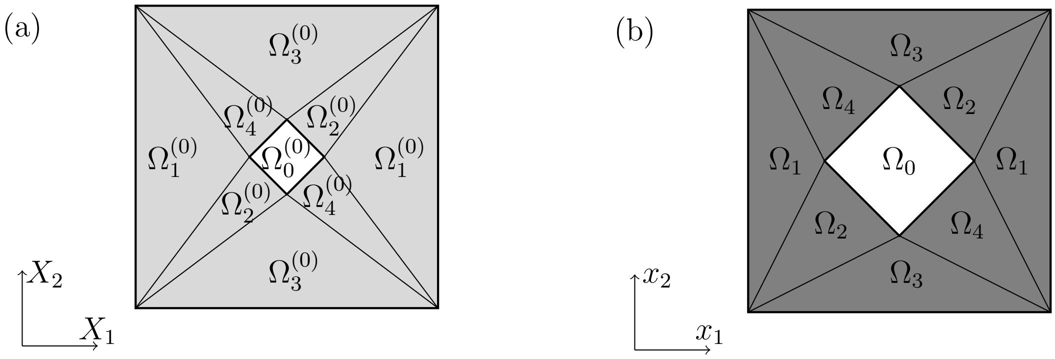

FIGURE 4.3: Geometric transformation of the (a) untransformed triangles $\Omega_1^{(0)}$,$\Omega_2^{(0)}$, $\Omega_3^{(0)}$, $\Omega_4^{(0)}$ with square inclusion $\Omega_0^{(0)}$ into the (b) transformed triangles Ω_1,Ω_2, Ω_3, Ω_4 with square inclusion Ω_0.

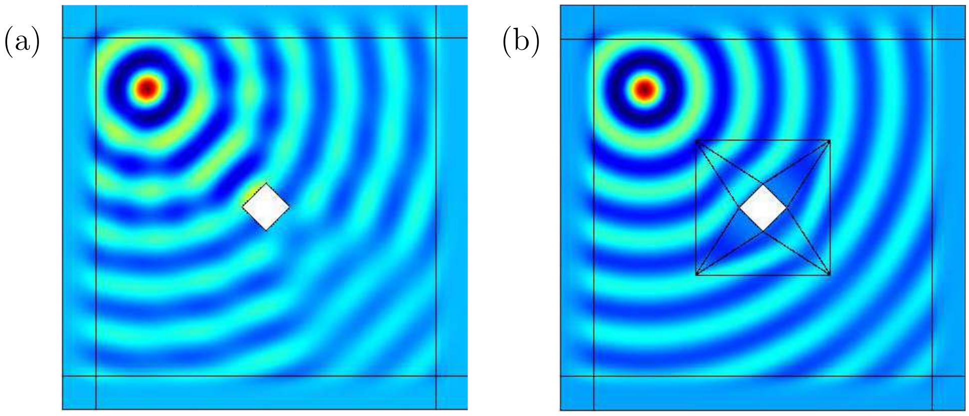

FIGURE 4.4: The displacement field generated by an external source in the presence of (a) an uncloaked and (b) cloaked inclined square cavities.

eqns. (4.7) corresponding deformation gradients are defined as

$$\begin{aligned} \mathbf{F}_{\Omega_1} &= \begin{bmatrix} \alpha_1 & 0 \\ 0 & 1 \end{bmatrix}, \qquad \mathbf{F}_{\Omega_2} = \begin{bmatrix} \alpha_2 & 0 \\ -\alpha_2 & 1 \end{bmatrix}, \\ \mathbf{F}_{\Omega_3} &= \begin{bmatrix} 1 & 0 \\ 0 & \alpha_1 \end{bmatrix}, \qquad \mathbf{F}_{\Omega_4} = \begin{bmatrix} \alpha_2 & 0 \\ \alpha_2 & 1 \end{bmatrix}. \end{aligned} \tag{4.12}$$

Then, the transformed equation of motion

$$\nabla \cdot \Big(\mathbf{C}_{\Omega_i} \nabla u(x_1, x_2) \Big) + \rho_{\Omega_i} \, \omega^2 u(x_1, x_2) = 0, \tag{4.13}$$

where each anisotropic stiffness tensor $\mathbf{C}_{\Omega_i} = \dfrac{1}{J_{\Omega_i}} \mathbf{F}_{\Omega_i} \mathbf{C}^{(0)} \mathbf{F}_{\Omega_i}^T$ and density $\rho_{\Omega_i} = \rho_0 / J_{\Omega_i}$ are now homogeneous. The displacement field excited by the force in a non-transformed and transformed medium is shown in the Figure 4.4.

The expanded form of eqn. (4.13) for the region Ω_1 is

$$\alpha_1 \frac{\partial^2 u}{\partial x_1^2} + \frac{1}{\alpha_1} \frac{\partial^2 u}{\partial x_2^2} + \frac{\beta^2}{\alpha_1 \mu_0} u = 0 \tag{4.14}$$

and for the region Ω_4 is

$$\alpha_2^2 \frac{\partial^2 u}{\partial x_1^2} + (1 + \alpha_2^2) \frac{\partial^2 u}{\partial x_2^2} + 2\alpha_2^2 \frac{\partial^2 u}{\partial x_1 \partial x_2} + \frac{\beta^2}{\mu_0} u = 0. \tag{4.15}$$

4.1.1.3 Eigenfrequency analysis

By separation the variables, we find a particular solution to eqn. (4.5)

$$U(X_1, X_2) = \Big(C_1 \cos k_1 X_1 + C_2 \sin k_1 X_1\Big)\Big(C_3 \cos k_2 X_2 + C_4 \sin k_2 X_2\Big), \quad (4.16)$$

where $k_1^2 + k_2^2 = \beta^2$ and C_1, C_2, C_3, C_4 are arbitrary constants. The rectangle domain $0 \leq X_1 \leq d_1$, $0 \leq X_2 \leq d_2$ with Dirichlet or Neumann boundary conditions on the edges is considered.

Eigenvalues are

$$\beta_{nm}^2 = k_{1,n}^2 + k_{2,m}^2, \quad (4.17)$$

where $k_{1,n} = \pi n/d_1$, $k_{2,m} = \pi m/d_2$ and eigenfrequency is

$$\omega_{nm} = \sqrt{\frac{\mu_0}{\rho_0}}\pi\sqrt{\left(\frac{n}{d_1}\right)^2 + \left(\frac{m}{d_2}\right)^2}.$$

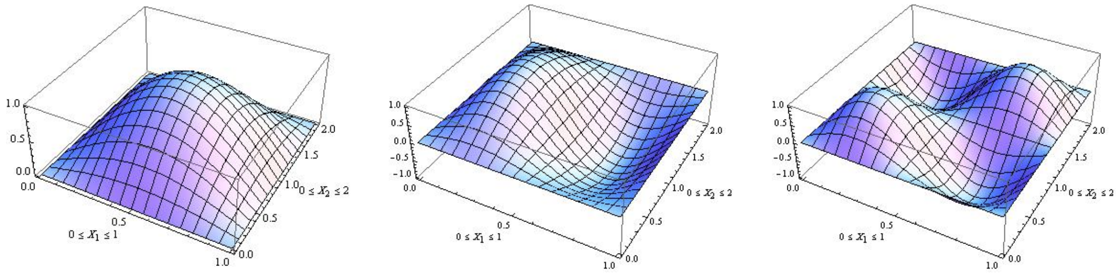

(a) (b) (c)

FIGURE 4.5: Eigenmodes rectangular domain with dimensions $d_1 = 1$, $d_2 = 2$ for Dirichlet boundary conditions (a) $n = 1, m = 1$ (b) $n = 2, m = 1$ (c) $n = 2, m = 2$.

The *eigenfunctions* for Dirichlet and Neumann boundary conditions are

$$\begin{aligned} U &= \sum_{n=1}^{\infty}\sum_{m=1}^{\infty} \sin(k_{1,n}X_1)\sin(k_{2,m}X_2), \\ U &= \sum_{n=1}^{\infty}\sum_{m=1}^{\infty} \cos(k_{1,n}X_1)\cos(k_{2,m}X_2), \end{aligned} \quad (4.18)$$

respectively and eigenmodes are shown in Figure 4.5 and 4.6.

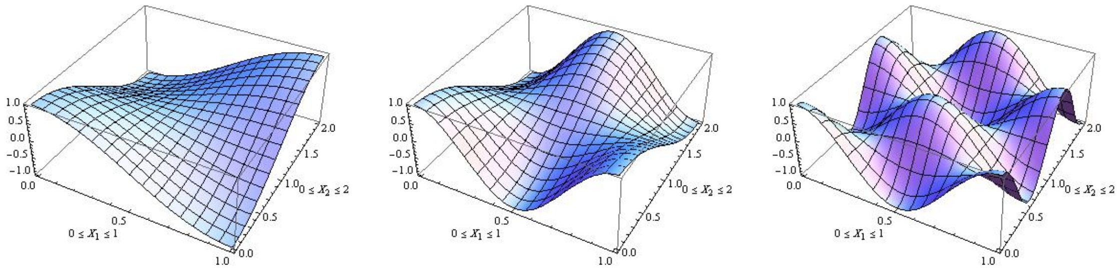

(a) (b) (c)

FIGURE 4.6: Eigenmodes rectangular domain with dimensions $d_1 = 1$, $d_2 = 2$ for Neumann boundary conditions (a) $n = 1, m = 1$ (b) $n = 2$, $m = 1$ (c) $n = 2$, $m = 2$.

4.1.2 Polar coordinate

Here, we give governing equation and coordinate transformation in cylindrical polar coordinate.

4.1.2.1 Equation of motion

In polar coordinates, the Navier equation for out of plane waves is simplified to the Helmholtz equation

$$\frac{\partial^2 U}{\partial R^2} + \frac{1}{R}\frac{\partial U}{\partial R} + \frac{1}{R^2}\frac{\partial^2 U}{\partial \Theta^2} + \beta^2 U = 0, \tag{4.19}$$

where $\beta = \sqrt{\rho_0/\mu_0}\,\omega$ is the frequency parameter. Considering separation of variables method, a general solution is defined

$$U(R,\Theta) = \Big(C_1 J_n(\beta R) + C_2 Y_n(\beta R)\Big)\Big(C_3 \cos(\Theta n) + C_4 \sin(\Theta n)\Big), \tag{4.20}$$

where C_1, C_2, C_3, C_4 are arbitrary amplitude constants.

4.1.2.2 Transformed equation

Circle to annulus transformation. The singular geometric transformation is

$$\begin{aligned} R &= G(r) = R_0 + \alpha_1 (r - R_0), \\ \Theta &= \theta, \end{aligned} \tag{4.21}$$

where $\alpha_1 = \dfrac{R_0}{R_0 - R_2}$.

By application of geometric transformation (4.21), the Helmholtz equation (5.3) is mapped into the equation

$$\frac{\partial^2 u}{\partial r^2} + \frac{1}{r - R_2}\frac{\partial u}{\partial r} + \frac{1}{(r - R_2)^2}\frac{\partial^2 u}{\partial \theta^2} + \frac{\rho_0 \alpha_1^2}{\mu_0}\omega^2 u = 0. \tag{4.22}$$

Annulus to annulus transformation. The geometric transformation is

$$\begin{aligned} R &= G(r) = R_0 + \alpha_1(r - R_0), \\ \Theta &= \theta, \end{aligned} \tag{4.23}$$

where $\alpha_1 = \dfrac{R_0 - R_1}{R_0 - R_2}$.

By application of geometric transformation (5.11), the Helmholtz equation (5.3) is mapped into the equation

$$\frac{\partial^2 u}{\partial r^2} + \frac{\alpha_1}{R_0 + \alpha_1(r - R_0)}\frac{\partial u}{\partial r} + \left[\frac{\alpha_1}{R_0 + \alpha_1(r - R_0)}\right]^2 \frac{\partial^2 u}{\partial \theta^2} + \frac{\rho_0 \alpha_1^2}{\mu_0}\omega^2 u = 0. \tag{4.24}$$

As previous case, solving by separation of variables method, we obtain a general solution

$$u(r,\theta) = \Big[C_1 J_n(\beta G(r)) + C_2 Y_n(\beta G(r))\Big]\Big[C_3 \cos(\theta n) + C_4 \sin(\theta n)\Big], \tag{4.25}$$

where $\beta = \sqrt{\rho_0/\mu_0}\,\omega$ is the frequency parameter and unknown coefficients C_1, C_2, C_3, C_4 must be determined by given boundary conditions, conditions at $r = 0$ or Sommerfield radiation conditions.

4.1.2.3 Eigenfrequency analysis

Circle domain $0 \le R \le R_1$, $0 \le \Theta \le 2\pi$.

Eigenvalues are

$$\beta_{nm} = \frac{k_{nm}}{R_1}, \tag{4.26}$$

where k_{nm} are positive roots of equations $J_n(\beta R_1) = 0$ and $J_n'(\beta R_1) = 0$ for Dirichlet and Neumann boundary conditions, respectively. Corresponding *eigenfrequencies* are $\omega_{nm} = \sqrt{\mu_0/\rho_0}\,k_{nm}/R_1$.

Eigenfunctions are

$$U = \sum_{m=1}^{\infty}\sum_{n=0}^{\infty} J_n(\beta_{nm} R)\begin{Bmatrix}\cos(\Theta n)\\ \sin(\Theta n)\end{Bmatrix}. \tag{4.27}$$

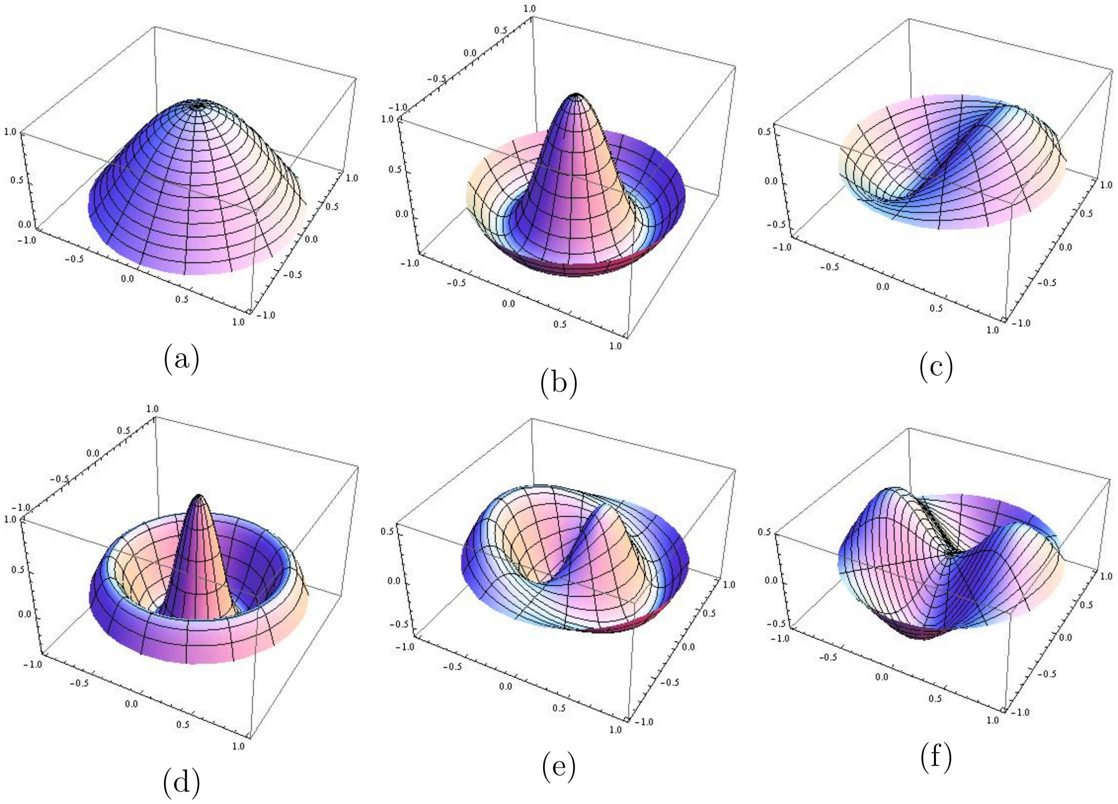

(a) (b) (c) (d) (e) (f)

FIGURE 4.7: Eigenmodes for Dirichlet boundary conditions (a) $n = 0$, $m = 1$ (b) $n = 0$, $m = 2$ (c) $n = 1$, $m = 1$ (d) $n = 0$, $m = 3$ (e) $n = 1$, $m = 2$ (f) $n = 2$, $m = 1$.

Annulus domain The annulus $R_1 \le R \le R_0$, $0 \le \Theta \le 2\pi$ domain maps into the annulus $R_2 \le r \le R_0$, $0 \le \theta \le 2\pi$.

I. On the external $r = R_0$ and internal $r = R_2$ borders the Dirichlet boundary conditions are applied. Then, *eigenvalues* are

$$\beta_{nm} = k_{nm}, \tag{4.28}$$

where k_{nm} are roots of the equation

$$J_n(\beta R_1)Y_n(\beta R_0) - J_n(\beta R_0)Y_n(\beta R_1) = 0. \tag{4.29}$$

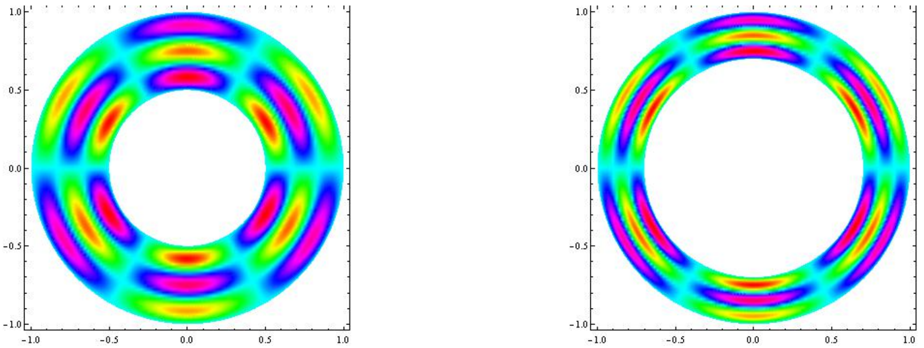

(a) (b)

FIGURE 4.8: (a) Untransformed and (b) transformed eigenmodes for Dirichlet boundary conditions

And *eigenfunctions* are

$$
\begin{aligned}
U &= \sum_{m=1}^{\infty}\sum_{n=0}^{\infty}\Big[Y_n(\beta_{nm}R_1)J_n(\beta_{nm}R) - J_n(\beta_{nm}R_1)Y_n(\beta_{nm}R)\Big]\begin{Bmatrix}\cos(\Theta n)\\ \sin(\Theta n)\end{Bmatrix},\\
u &= \sum_{m=1}^{\infty}\sum_{n=0}^{\infty}\Big[Y_n(\beta_{nm}R_1)J_n(\beta_{nm}G(r)) - J_n(\beta_{nm}R_1)Y_n(\beta_{nm}G(r))\Big]\begin{Bmatrix}\cos(\theta n)\\ \sin(\theta n)\end{Bmatrix}.
\end{aligned}
\tag{4.30}
$$

II. Neumann boundary conditions at $r = R_2$ and $r = R_0$. *Eigenvalues* are

$$
\beta_{nm} = k_{nm}, \tag{4.31}
$$

where k_{nm} are roots of equation

$$
J'_n(\beta R_1)Y'_n(\beta R_0) - J'_n(\beta R_0)Y'_n(\beta R_1) = 0 \tag{4.32}
$$

and *eigenfunctions* are

$$
\begin{aligned}
U &= \sum_{m=1}^{\infty}\sum_{n=0}^{\infty}\Big[Y'_n(\beta_{nm}R_1)J_n(\beta_{nm}R) + J'_n(\beta_{nm}R_1)Y_n(\beta_{nm}R)\Big]\begin{Bmatrix}\cos(\Theta n)\\ \sin(\Theta n)\end{Bmatrix},\\
u &= \sum_{m=1}^{\infty}\sum_{n=0}^{\infty}\Big[Y'_n(\beta_{nm}R_1)J_n(\beta_{nm}G(r)) + J'_n(\beta_{nm}R_1)Y_n(\beta_{nm}G(r))\Big]\begin{Bmatrix}\cos(\theta n)\\ \sin(\theta n)\end{Bmatrix}.
\end{aligned}
\tag{4.33}
$$

III. Mixed boundary conditions, on the inner border Dirichlet boundary condition and on the outer border Neumann boundary condition. *Eigenvalues* are

$$\beta_{nm} = k_{nm}, \tag{4.34}$$

where k_{nm} are roots of equation

$$J_n(\beta R_1)Y_n'(\beta R_0) - J_n'(\beta R_0)Y_n(\beta R_1) = 0 \tag{4.35}$$

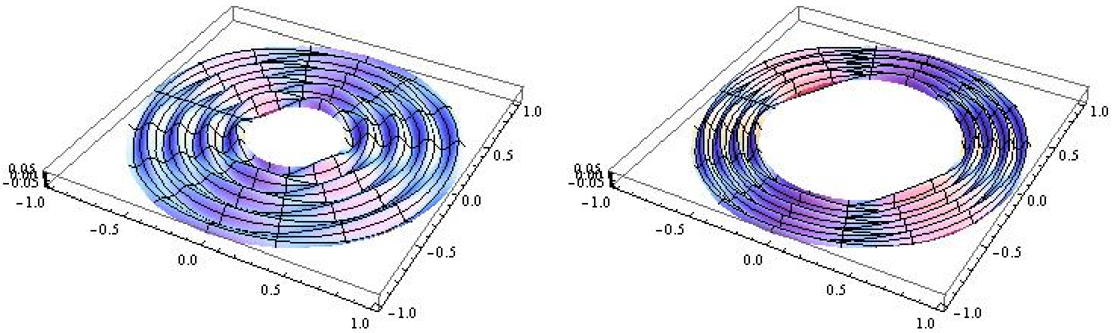

(a) (b)

FIGURE 4.9: (a) Untransformed and (b) transformed eigenmodes for the case $n = 3$, $\beta = 1.00$

and *eigenfunctions* are

$$\begin{aligned} U &= \sum_{m=1}^{\infty}\sum_{n=0}^{\infty}\Big[-Y_n(\beta_{nm}R_1)J_n(\beta_{nm}R) + J_n(\beta_{nm}R_1)Y_n(\beta_{nm}R)\Big]\begin{Bmatrix}\cos(\Theta n)\\ \sin(\Theta n)\end{Bmatrix}, \\ u &= \sum_{m=1}^{\infty}\sum_{n=0}^{\infty}\Big[-Y_n(\beta_{nm}R_1)J_n(\beta_{nm}G(r)) + J_n(\beta_{nm}R_1)Y_n(\beta_{nm}G(r))\Big]\begin{Bmatrix}\cos(\theta n)\\ \sin(\theta n)\end{Bmatrix}. \end{aligned} \tag{4.36}$$

IV. Mixed boundary conditions, on the inner border Neumann boundary condition and on the outer border Dirichlet boundary condition. *Eigenvalues* are

$$\beta_{nm} = k_{nm}, \tag{4.37}$$

where k_{nm} are roots of equation

$$J_n'(\beta R_1)Y_n(\beta R_0) - J_n(\beta R_0)Y_n'(\beta R_1) = 0 \tag{4.38}$$

and *eigenfunctions* are

$$U = \sum_{m=1}^{\infty}\sum_{n=0}^{\infty}\left[Y_n(\beta_{nm}R_0)J_n(\beta_{nm}R) + J_n(\beta_{nm}R_0)Y_n(\beta_{nm}R)\right]\begin{Bmatrix}\cos(\Theta n)\\ \sin(\Theta n)\end{Bmatrix},$$
$$u = \sum_{m=1}^{\infty}\sum_{n=0}^{\infty}\left[Y_n(\beta_{nm}R_0)J_n(\beta_{nm}G(r))) + +J_n(\beta_{nm}R_0)Y_n(\beta_{nm}G(r))\right]\begin{Bmatrix}\cos(\theta n)\\ \sin(\theta n)\end{Bmatrix}. \tag{4.39}$$

Eigenfrequencies are

$$\omega_{nm} = \sqrt{\frac{\mu_0}{\rho_0}}k_{nm}. \tag{4.40}$$

4.2 Analytical and numerical results

In this chapter, in order to better understand the implementation in Comsol, we will give a scheme for solving the problem of the transfer of waves between two different media and the scattering of waves on inclusion. Elastic properties are considered uniform. Please note that the obtained numerical and analytical solutions are precisely the same, I do not show a comparison of the results.

4.2.1 Transmission problems in an infinite medium

Here, we investigate analytically the transmission and reflection of an elastic wave at an interface and through a slab.

4.2.1.1 Transmission and reflection of wave at an interface

We consider an incident time-harmonic plane wave [61, 83] with vector $\mathbf{k}_1$ and frequency ω, θ_I is the angle of incidence. The wave propagates in a medium with elastic properties μ_1, ρ_1. At $x_1 = x_0$ there is a straight interface and for $x_1 \geq x_0$ a second linear elastic homogeneous and isotropic medium has elastic constants μ_2, ρ_2. At $x_1 = x_0$ a reflected wave u_R and a transmitted wave u_T are generated.

The plane incident wave propagating to the right is

$$u_I = e^{ik_1(\cos\theta_I\, x_1 + \sin\theta_I\, x_2)}. \tag{4.41}$$

The reflected and transmitted waves are

$$\begin{aligned} u_R &= A_R\, e^{ik_1(-\cos\theta_I\, x_1 + \sin\theta_I\, x_2)}, \\ u_T &= A_T\, e^{ik_2(\cos\theta_2\, x_1 + \sin\theta_2\, x_2)}, \end{aligned} \tag{4.42}$$

where the angle θ_2 satisfy Shell's law

$$k_1 \sin\theta_I = k_2 \sin\theta_2$$

or

$$\frac{\sin\theta_I}{c_1} = \frac{\sin\theta_2}{c_2} \quad \text{with} \quad c_1 = \sqrt{\frac{\mu_1}{\rho_1}}.,\ c_2 = \sqrt{\frac{\mu_2}{\rho_2}}$$

The unknown amplitude coefficients are obtained from continuity of displacements and tractions

$$\begin{aligned} A_R &= \frac{\mu_1 k_{11} - \mu_2 k_{21}}{\mu_1 k_{11} + \mu_2 k_{21}}\, e^{2ik_{11}x_0}, \\ A_T &= \frac{2\mu_1 k_{11}}{\mu_1 k_{11} + \mu_2 k_{12}} e^{ix_0(k_{11}-k_{12})}, \end{aligned} \tag{4.43}$$

with x_0 is the position of the interface, $k_2 = \omega\sqrt{\rho_2/\mu_2}$, $k_1 = \omega\sqrt{\rho_1/\mu_1}$ are the propagation wavenumbers, $k_{11} = k_1\cos\theta_I$, $k_{12} = k_1\sin\theta_I$, $k_{21} = k_2\cos\theta_2$ are x_1, x_2 components of wavevectors k_1, k_2.

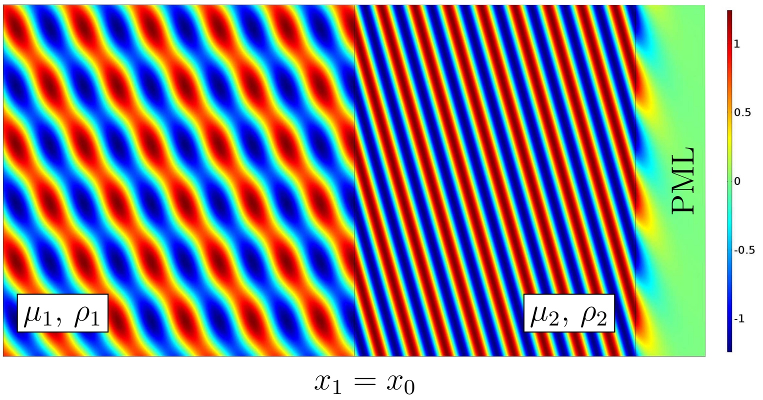

FIGURE 4.10: Scattering of an oblique incident plane wave on the boundary between two medium with shear moduli $\mu_1 = 1$, $\mu_2 = 0.3$ and $\rho_1 = \rho_2$, $\theta_I = 34°$. Perfectly matched layer is applied as infinite domain.

4.2.1.2 Transmission and reflection of wave through a slab

We consider a two interface problem with a slab with elastic properties μ_2, ρ_2 separating semi-infinite media, with material properties μ_1, ρ_1. Width of slab is d

and the two interface are at $x_1 = x_0$ and $x_1 = x_0 + d$.

The incident wave is

$$u_I = e^{ik_1(\cos\theta_i x_1 + \sin\theta_I x_2)} \tag{4.44}$$

and the reflected wave

$$u_R = A_R e^{ik_1(-\cos\theta_I x_1 + \sin\theta_I x_2)}. \tag{4.45}$$

Inside the slab there are two waves propagating to the left and to the right

$$\begin{aligned} u_1 &= B_1 e^{ik_2(\cos\theta_2 x_1 + \sin\theta_2 x_2)}, \\ u_2 &= B_2 e^{ik_2(-\cos\theta_2 x_1 + \sin\theta_2 x_2)} \end{aligned} \tag{4.46}$$

and, again $k_1 \sin\theta_I = k_2 \sin\theta_2$. The transmitted wave is

$$u_T = A_T e^{ik_1(\cos\theta_I x_1 + \sin\theta_I x_2)}. \tag{4.47}$$

Imposing the continuity condition at the interfaces $x_1 = x_0$ and $x_1 = x_0 + d$,

$$\begin{aligned} &\left.\begin{aligned} u_I + u_R &= u_1 + u_2 \\ \mu_1\left(\frac{\partial u_I}{\partial x_1} + \frac{\partial u_R}{\partial x_1}\right) &= \mu_2\left(\frac{\partial u_1}{\partial x_1} + \frac{\partial u_2}{\partial x_1}\right) \end{aligned}\right\} \quad \text{on } x_1 = x_0 \\ &\left.\begin{aligned} u_1 + u_2 &= u_T \\ \mu_2\left(\frac{\partial u_1}{\partial x_1} + \frac{\partial u_2}{\partial x_1}\right) &= \mu_1 \frac{\partial u_T}{\partial x_1} \end{aligned}\right\} \quad \text{on } x_1 = x_0 + d \end{aligned} \tag{4.48}$$

we define

$$\begin{aligned} A_R &= -\frac{e^{2\,i\,x_0\,k_{11}}(e^{2\,i\,d\,k_{21}} - 1)(\mu_2 k_{21} - \mu_1 k_{11})(\mu_2 k_{21} + \mu_1 k_{11})}{e^{2\,i\,d\,k_{21}}(\mu_2 k_{21} - \mu_1 k_{11})^2 - (\mu_2 k_{21} + \mu_1 k_{11})^2}, \\ A_T &= -\frac{4\,e^{i\,d(k_{21} - k_{11})}\mu_1 \mu_2 k_{11} k_{21}}{e^{2\,i\,d\,k_{21}}(\mu_2 k_{21} - \mu_1 k_{11})^2 - (\mu_2 k_{21} + \mu_1 k_{11})^2}, \\ B_1 &= -\frac{2 k_{11} \mu_1 (k_{11}\mu_1 + k_{21}\mu_2) e^{i x_0 (k_{11} - k_{21})}}{e^{2\,i\,d\,k_{21}}(\mu_2 k_{21} - \mu_1 k_{11})^2 - (\mu_2 k_{21} + \mu_1 k_{11})^2}, \\ B_2 &= \frac{2 k_{11} \mu_1 (k_{11}\mu_1 - k_{21}\mu_2) e^{i((x_0 + 2d)k_{21} + x_0 k_{11})}}{e^{2\,i\,d\,k_{21}}(\mu_2 k_{21} - \mu_1 k_{11})^2 - (\mu_2 k_{21} + \mu_1 k_{11})^2}, \end{aligned} \tag{4.49}$$

where the components of wavevectors are $k_{11} = k_1 \cos\theta_I$, $k_{21} = k_2 \cos\theta_2$, $k_{12} = k_1 \sin\theta_I$, $k_{22} = k_2 \sin\theta_2$.

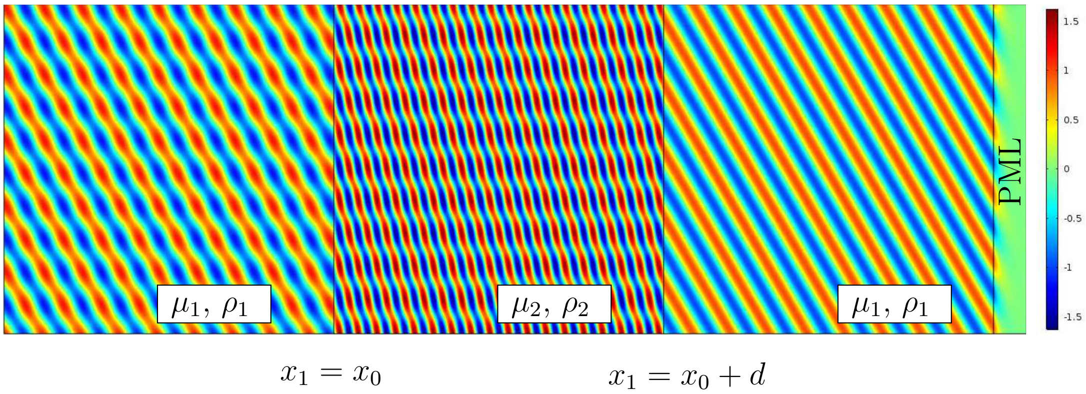

FIGURE 4.11: Reflection and transmission of a plane wave trough a slab with μ_2, ρ_2. $\rho_1 = \rho_2$, $\theta_i = 30°$, $\mu_1 = 1$, $\mu_2 = 0.3$. The left domain is perfectly matched layer, which approximates infinite extension. Displacent field along the line at $X_2 = 0$ is given in Figure 4.12

In Comsol, to implement the scattering problem in multi-phase medium, I must use the incidence field as the sum of the incident and reflected waves. For the results in Figures 4.10 and 4.11, Floquet boundary conditions are applied to the upper and lower boundaries to impose infinite sample expansions, and perfectly matched layer representing semi-infinite extension in horizontal direction is applied on left side. Comparison of displacement field along the line at $X_2 = 0$ obtained by analytical and semi-analytical methods are given in Figure 4.12.

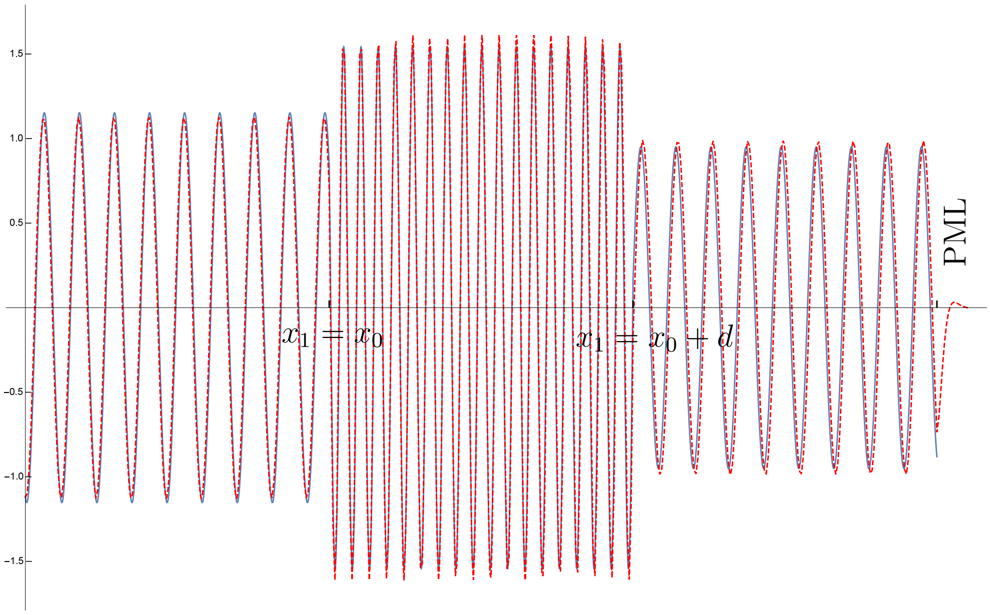

FIGURE 4.12: Displacement field. Comparison of analytical (blue) and semi-analytical (red dashed) solutions along the line at $X_2 = 0$ in Figure 4.11

.

4.2.2 Scattering of waves by a single inclusion

The analytical solution for a circular scatterer of radius R_0 and its implementation is detailed.

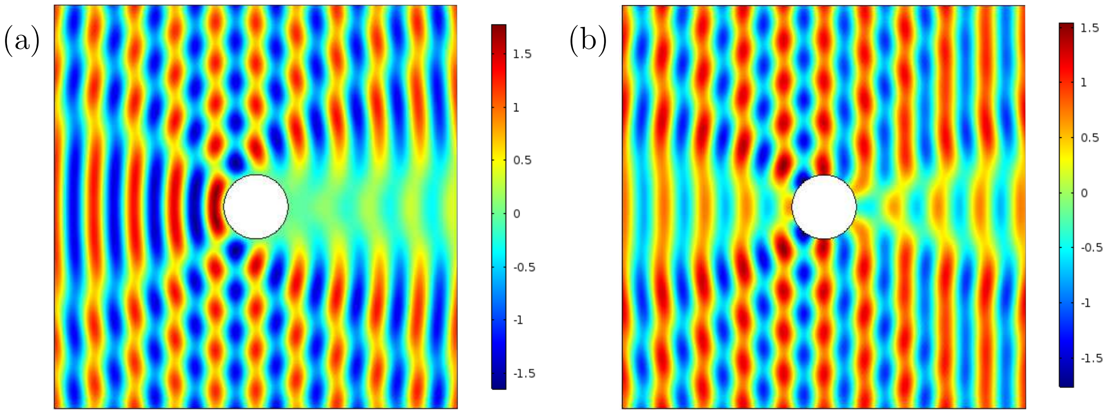

FIGURE 4.13: The displacement field for an incident plane wave scattered by a circular hole with radius $R_0 = 1$ and frequency $\omega = 5$ Hz. (a) Dirichlet boundary conditions, (b) Neumann boundary conditions.

The incident plane wave with unit amplitude and angle of incidence θ_I is expanded in the following form

$$u_I = e^{ik_1(\cos\theta_I x_1 + \sin\theta_I x_2)} = \sum_{n=-\infty}^{\infty} A_n J_n(k_1 r) e^{in\theta}, \tag{4.50}$$

where the amplitudes $A_n = i^n e^{-in\theta_I}$ and the frequency parameter $k_1 = \sqrt{\rho_1/\mu_1}\,\omega$, μ_1, ρ_1 are shear modulus and density of external domain, respectively.

The interior field u_2 of the circular domain $r < R_0$ has the form

$$u_2 = \sum_{n=-\infty}^{\infty} \bar{A}_n J_n(k_2 r) e^{in\theta}, \tag{4.51}$$

where the frequency parameter $k_2 = \sqrt{\rho_2/\mu_2}\,\omega$ with shear modulus μ_2 and density ρ_2 material parameters of internal domain.

The total field for $r > R_0$ is the sum of the incident and the scattered one. It is given in the form

$$u_t = \sum_{n=-\infty}^{\infty} \left[A_n J_n(k_1 r) + B_n H_n^{(1)}(k_1 r) \right] e^{in\theta}. \tag{4.52}$$

In absence of the interior domain, for Dirichlet boundary condition on $r = R_0$

$$B_n = -\frac{J_n(k_1 R_0)}{H_n^{(1)}(k_1 R_0)} A_n, \tag{4.53}$$

while for Neumann boundary condition

$$B_n = -\frac{J_n'(k_1 R_0)}{H_n^{(1)'}(k_1 R_0)} A_n. \tag{4.54}$$

In presence of an elastic inclusion with parameters μ_2, ρ_2, the continuity conditions between two domains at $r = R_0$ lead to

$$\begin{aligned} B_n &= -\frac{q J_n'(k_1 R_0) J_n(k_2 R_0) - J_n(k_1 R_0) J_n'(k_2 R_0)}{q H_n^{(1)'}(k_1 R_0) J_n(k_2 R_0) - H_n^{(1)}(k_1 R_0) J_n'(k_2 R_0)} A_n, \\ \bar{A}_n &= \frac{q\left[A_n J_n'(k_1 R_0) + B_n H_n^{'(1)}(k_1 R_0)\right]}{J_n'(k_2 R_0)}, \end{aligned} \tag{4.55}$$

where

$$q = \frac{\mu_1\, k_1}{\mu_2\, k_2} = \sqrt{\frac{\mu_1\, \rho_1}{\mu_2\, \rho_2}}. \tag{4.56}$$

The $\mu_1 = \mu_2$ and $\rho_1 = \rho_2$ corresponds to homogeneous case $B_n = 0$, $\bar{A}_n = A_n$, while $\mu_2 \to \infty$ corresponds to Dirichlet boundary conditions and $\mu_2 = 0$ to Neumann boundary conditions.

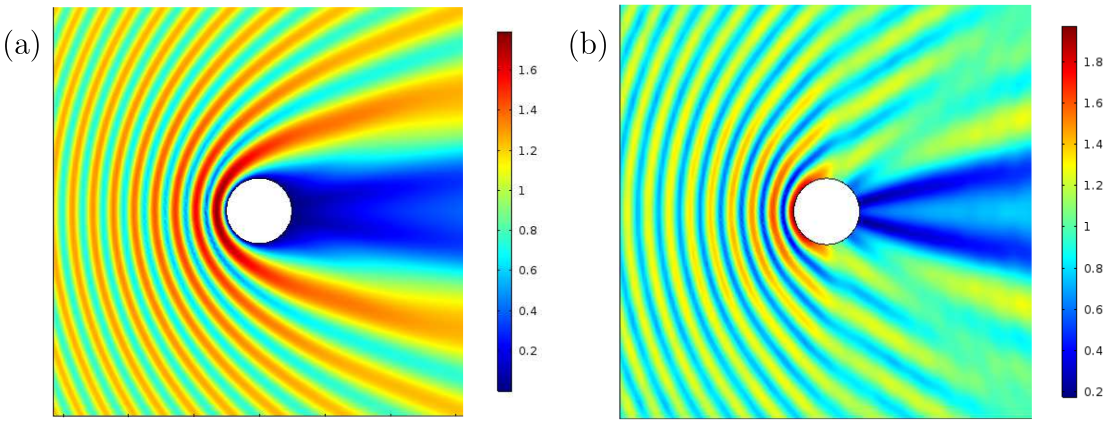

FIGURE 4.14: Amplitude of the scattered field for a plane wave scattered by a circular hole of radius $R_0 = 1$, frequency $\omega = 5$ Hz (a) Dirichlet boundary conditions, (b) Neumann boundary conditions.

In Table 4.1, the incident, scattered and total fields are given for incidence angle $\theta_I = 0$ and $\theta_I = \pi/4$. Dirichlet and Neumann boundary conditions are imposed on the boundary of holes $R_0 = 1$.

	The incident field	The scattered field	The total field
0	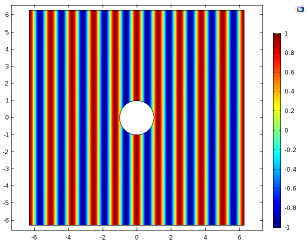	(a) 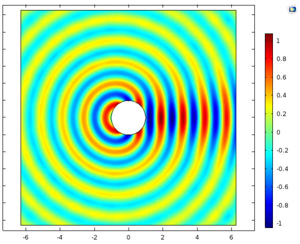 (b) 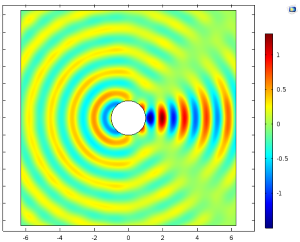	(a) 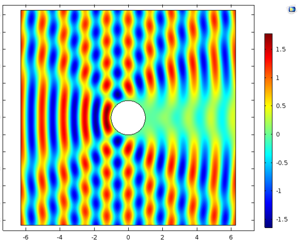 (b) 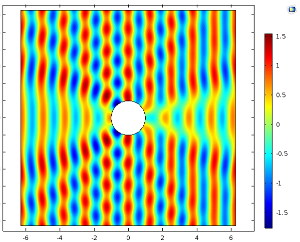
$\pi/4$	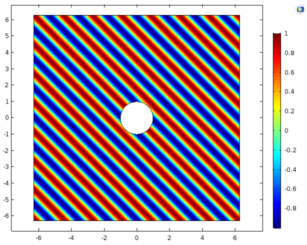	(a) 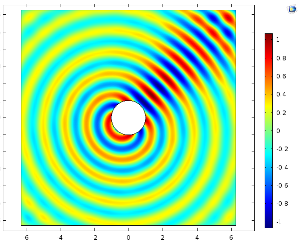 (b) 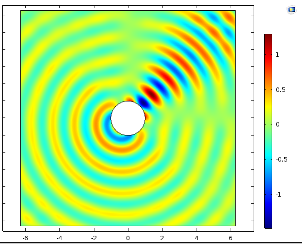	(a) 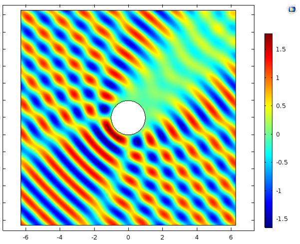 (b) 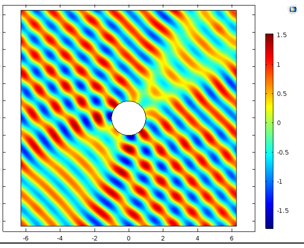

TABLE 4.1: Scattering of a wave by a circular hole. The incident, scattered and total fields are given for different angle of incidence. The radius of holes is $R_0 = 1$. (a) Dirichlet and (b) Neumann boundary conditions are considered.

In order to verify the implementation of the designed geometric transformation, we demonstrate wave scattering by a single inclusion surrounded by anisotropic transformation-based shell domain. This implementation will also be used to generate numerically a Gaussian beam. In Figure 4.16 the displacement fields in homogeneous (see Figure 4.16a) and perforated domains (see Figure 4.16 b-e) are given. The wave is excited by an external force at the position $r_0 = 0.3$, $\theta_0 = \pi/4$. In Comsol to avoid the back scattering, we introduce the perfectly matched layer (PML), where the model is based on transformation optics techniques. The derivation of Green function and implementation of PML are given in

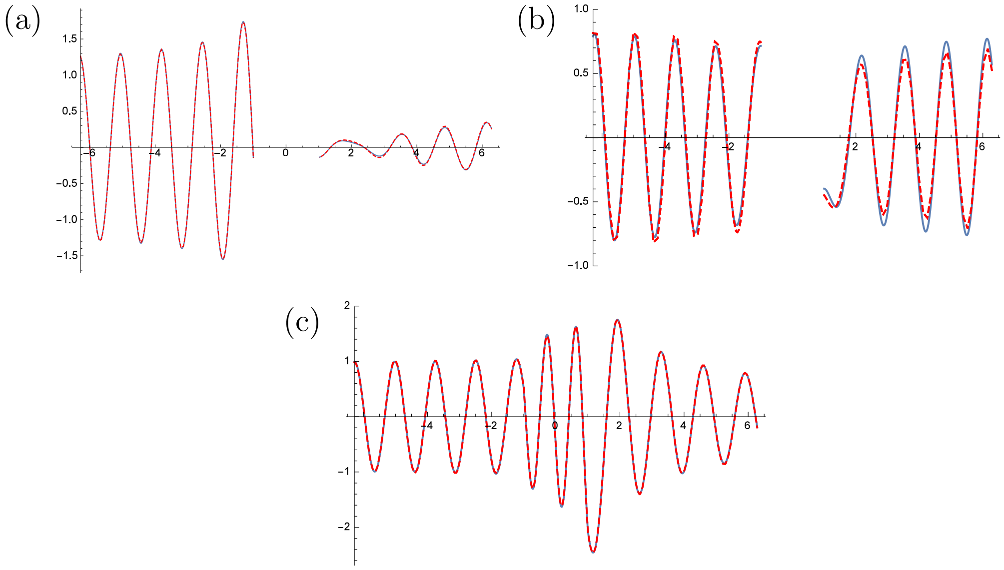

FIGURE 4.15: Comparison of displacement field at line $X_2 = 0$ in Fig.4.13 obtained by analytical (blue) and numerical (red dashed) methods. Perforated hole with (a) Dirichlet and (b) Neumann boundary conditions of hole with radius $R_1 = 0.1$. (c) An inclusion domain with shear modulus $\mu_2 = 0.5$ and matrix domain $\mu_1 = 1$, densities are same $\rho_1 = \rho_2$.

Appendices A and B. In Figure 4.16b and Figure 4.16c the uncloaked and cloaked circular inclusions with radii 0.1. Figure 4.16d shows the localised resonance at the interface between the shell and matrix domain where material property of anisotropic annulus domain is defined by unfolding transformation with parameters $R_0/d = 0.2$, $R_1/d = 0.27$, $R_2/d = 0.1$. And in the Figure 4.16e, we show how to avoid the localisation in Figure 4.16d introducing the same radial stiffness with small dissipation term.

In Comsol, to realize scattering of plane wave by a hole, we define an incident wave as the background field. To avoid back scattering, we can use perfectly matched layers (see Figure 4.16) or absorbing boundary conditions (see Figures 4.13 and 4.14) around domain in *Electromagnetic Waves* package. In Figure 4.15, the comparison of displacement field at line $X_2 = 0$ scattered by a single inclusion with radii $R_1 = 1$ is shown. In Figures 4.15a and 4.15b, Dirichlet and Neumann boundary conditions are considered on holes, which correspond to $\mu_2 \to \infty$ and $\mu_2 \to 0$, respectively. In Figure 4.15c, the shear modulus of inclusion domain is $\mu_2 = 0.5$.

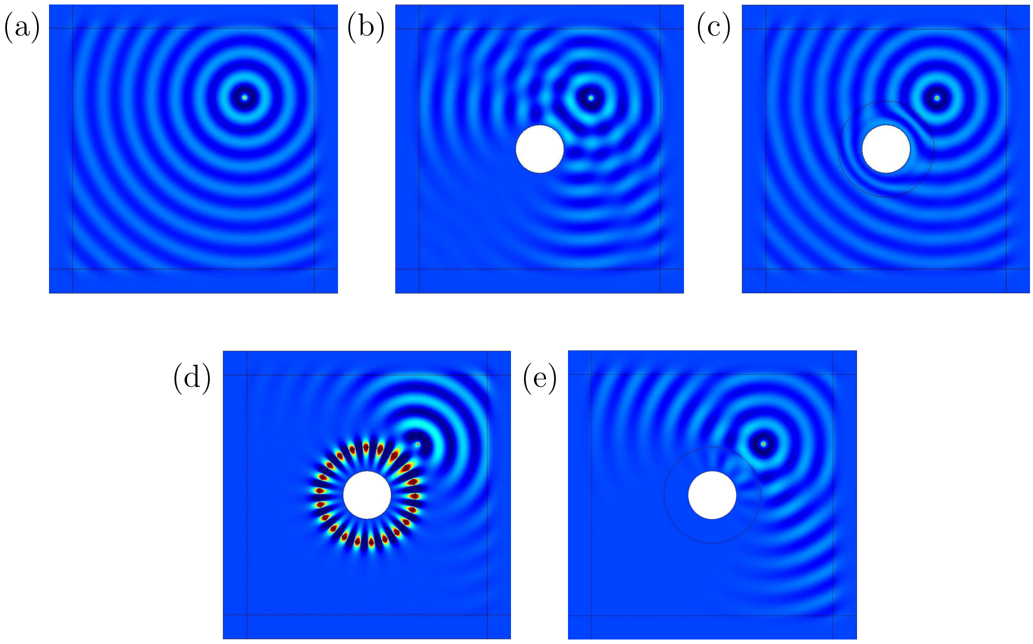

FIGURE 4.16: Displacement field excited by an external force applied in the position $r_0 = 0.3$, $\theta_0 = \pi/4$. (a) Homogeneous domain. (b) Wave scattering by a single hole with radius $r/d = 0.1$. (c) Cloaked hole $R_2/d = 0.1$ with parameters $R_1/d = 0.001$, $R_0/d = 0.2$. (d) Unfolding transformation based shell domain with $R_0/d = 0.2$, $R_1/d = 0.27$, $R_2/d = 0.1$. (e) Unfolding transformation based shell domain with $R_0/d = 0.2$, $R_1/d = 0.27$, $R_2/d = 0.1$, where radial stiffness with small dissipation term.

Chapter 5

Control of elastic shear waves by transformation-based periodically perforated systems

A doubly periodic geometric transformation is applied to the problem of out of plane shear wave propagation in a doubly periodic perforated elastic medium. The technique leads to the design of a system of radially anisotropic and inhomogeneous shells surrounding the void inclusions, that can be tuned to give the desired filtering properties.

For a regular transformation, the transformed elastic system displays the same dispersion properties than the original homogeneous one, but for overlapping and unfolding transformations new filtering properties can be obtained, which include anomalous resonances at zero and finite frequencies. Low-frequency homogenisation reveals how it is possible to tune the phase and group velocity in the long-wave limit at any value, or to obtain a zero frequency band gap for Neumann boundary conditions. The dispersion properties of the medium are studied both semi-analytically by the multipole expansion and numerically by the finite element methods.

Several applications are shown, including the transmission problem throughout a grating of void inclusions and an interface in a waveguide, where the capability of the proposed model is quantitatively demonstrated by computing the transmitted power flow. Finally, we gave a demonstration of defect modes in a waveguide and of tuning the transformation for the research of Dirac points.

5.1 Out of plane shear waves in a doubly periodic medium

We consider the doubly periodic medium shown in Figure 5.1a, it consists of a square distribution of cylindrical holes of radius R_1. The centers of the holes in each unit cell have the position

$$\mathbf{Y}^{\mathbf{h}} = h_1\mathbf{a}_1 + h_2\mathbf{a}_2, \qquad \mathbf{a}_1 = \begin{pmatrix} d \\ 0 \\ 0 \end{pmatrix}, \ \mathbf{a}_2 = \begin{pmatrix} 0 \\ d \\ 0 \end{pmatrix}, \tag{5.1}$$

where d is the dimension of the edge of the unit cell and $\mathbf{h} = (h_1, h_2)^T$, with $h_1, h_2 \in \mathbb{Z}$, a multi-index.

5.1.1 Governing equations

We analyze wave propagation in the time-harmonic regime, the time dependence $e^{-i\omega t}$, with ω the radian frequency and t the time, is not indicated for ease of notation. We focus on out of plane shear waves, the displacement is

$$\mathbf{U} = \begin{pmatrix} 0 \\ 0 \\ U(\mathbf{X}) \end{pmatrix}, \tag{5.2}$$

where $\mathbf{X} = (X_1 \ \ X_2 \ \ 0)^T$ is the position vector.

Wave propagation in a linear elastic medium is governed by the Helmholtz equation [61]

$$\nabla_{\mathbf{X}} \cdot \mathbf{C}^{(0)} \nabla_{\mathbf{X}} U(\mathbf{X}) + \rho_0 \omega^2 U(\mathbf{X}) = 0, \qquad \text{for } \mathbf{X} \in \Omega_{R_1,d}, \tag{5.3}$$

where $\mathbf{C}^{(0)}$ is the second-order stiffness tensor for out of plane motion[1], ρ_0 the density and $\nabla_{\mathbf{X}}$ the gradient operator in the original domain. The domain

$$\Omega_{R_1,d} = \mathbb{R}^2 \setminus \Omega'_{R_1,d}, \tag{5.4}$$

---

[1] With respect to the full fourth-order stiffness tensor $\mathcal{C}^{(0)}$, we have $C^{(0)}_{ij} = 2\,\mathcal{C}^{(0)}_{i3j3}$, where $i, j = 1, 2$ in cartesian coordinates and $i, j = R, \Theta$ in cylindrical ones.

where the complement

$$\Omega'_{R,d} = \bigcup_{h_1,h_2=-\infty}^{+\infty} S(\mathbf{Y^h}, R), \quad \text{with} \quad S(\mathbf{Y^h}, R) = \{\mathbf{X} : |\mathbf{X} - \mathbf{Y^h}| < R\}. \tag{5.5}$$

For later use we also define

$$Q(\mathbf{Y^h}, d) = \{\mathbf{X} : 0 \le X_1 - {Y_1}^{\mathbf{h}} \le d,\, 0 \le X_2 - {Y_2}^{\mathbf{h}} \le d\}, \tag{5.6}$$

so that the domain of the generic unit cell is

$$\Omega^{\mathbf{h}}_{R_1,d} = \overline{Q(\mathbf{Y^h}, d)} \setminus S(\mathbf{Y^h}, R_1), \tag{5.7}$$

where the bar indicates the closure.

The linear momentum balance (5.3) is complemented by either Neumann or Dirichlet boundary conditions on $\partial\Omega_{R_1,d}$, namely

$$\mathbf{C}^{(0)}\nabla_{\mathbf{X}}U(\mathbf{X}) \cdot \mathbf{n} = \mathbf{0} \quad \text{or} \quad U(\mathbf{X}) = \mathbf{0}\,. \tag{5.8}$$

For an isotropic medium, eqn. (5.3) reduces to the classical Helmholtz equation

$$\Delta_{\mathbf{X}}U(\mathbf{X}) + \beta^2 U(\mathbf{X}) = 0, \qquad \mathbf{X} \in \Omega_{R_1,d}, \tag{5.9}$$

with $\beta = \omega/c_0$ the frequency parameter, $c_0 = \sqrt{\mu_0/\rho_0}$ the phase velocity, μ_0 the shear modulus and $\Delta_{\mathbf{X}}$ the Laplacian operator in the original domain. The associated Neumann boundary conditions are

$$\mu_0 \nabla_{\mathbf{X}}U(\mathbf{X}) \cdot \mathbf{n} = \mathbf{0} \quad \text{on} \quad \partial\Omega_{R_1,d}\,, \tag{5.10}$$

while Dirichlet conditions remain as in (5.8).

5.1.2 Transformed Geometry

A radial geometric transformation is applied in each unit cell, that is the shell centred at $\mathbf{Y^h}$, with internal and external radii R_1 and R_0, respectively, is mapped into the shell centred at $\mathbf{y^h} = \mathbf{Y^h}$, with internal and external radii R_2 and R_0, respectively (see Figure 5.1c). The linear radial mapping $\mathbf{x} = \mathcal{F}(\mathbf{X})$, for $\mathbf{X} \in$

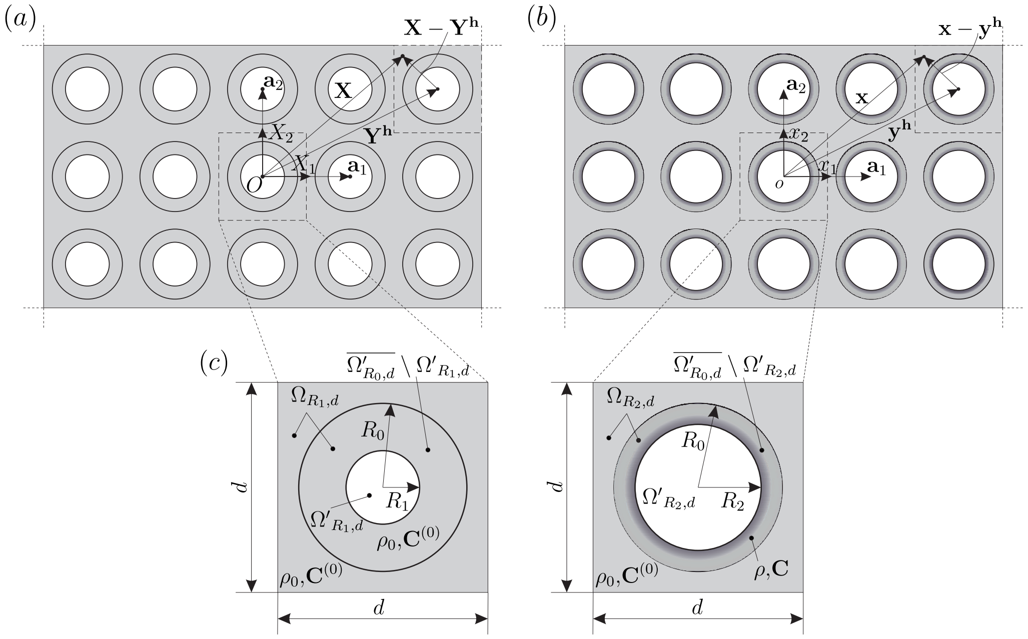

FIGURE 5.1: (a) Original and (b) transformed doubly periodic perforated domains. (c) Unit cells. The linear isotropic and homogeneous elastic material in the shell $R_1 < R < R_0$ is transformed into the linear anisotropic and inhomogeneous elastic material in the region $R_2 < r < R_0$.

$\overline{\Omega'_{R_0,d}} \setminus \Omega'_{R_1,d}$, in each cell is

$$\begin{cases} r^{\mathbf{h}} = g(R^{\mathbf{h}}) = R_0 + \alpha_1 (R^{\mathbf{h}} - R_0), \\ \theta^{\mathbf{h}} = \Theta^{\mathbf{h}}, \end{cases} \tag{5.11}$$

where

$$\alpha_1 = \frac{R_0 - R_2}{R_0 - R_1},$$

and

$$R^{\mathbf{h}} = |\mathbf{X} - \mathbf{Y}^{\mathbf{h}}|, \;\; \Theta^{\mathbf{h}} = 2 \arctan\left(\frac{X_2 - Y_2^{\mathbf{h}}}{X_1 - Y_1^{\mathbf{h}} + R^{\mathbf{h}}} \right),$$

$$r^{\mathbf{h}} = |\mathbf{x} - \mathbf{y}^{\mathbf{h}}|, \;\; \theta^{\mathbf{h}} = 2 \arctan\left(\frac{x_2 - y_2^{\mathbf{h}}}{x_1 - y_1^{\mathbf{h}} + r^{\mathbf{h}}} \right). \tag{5.12}$$

We stress that the transformed geometry maintains the same periodicity as the original one, but it can be easily expanded to non-periodic transformations. The inverse transformation $\mathbf{X} = \mathcal{F}^{-1}(\mathbf{x})$, for $\mathbf{x} \in \overline{\Omega'_{R_0,d}} \setminus \Omega'_{R_2,d}$, is

$$\begin{cases} R^{\mathbf{h}} = G(r^{\mathbf{h}}) = g^{-1}(r^{\mathbf{h}}) = R_0 + \dfrac{r^{\mathbf{h}} - R_0}{\alpha_1}, \\ \Theta^{\mathbf{h}} = \theta^{\mathbf{h}}. \end{cases} \tag{5.13}$$

5.1.3 Transformed equation of motion

Restricting the attention to the cell identified by $h_1 = h_2 = 0$, with $\mathbf{Y^0} = \mathbf{y^0} = \mathbf{0}$, the governing eqn. (5.3) is transformed into

$$\nabla \cdot \mathbf{C} \nabla u(\mathbf{x}) + \rho\, \omega^2 u(\mathbf{x}) = 0, \tag{5.14}$$

where $u(\mathbf{x})$ is the transformed displacement, that we assume equal to $U(\mathbf{X})$. In addition, ∇ is the gradient operator in the transformed domain and ρ and $\mathbf{C}$ the transformed density and stiffness tensor, respectively [32, 33]. They can be given in terms of the Jacobian of the transformation, which can be expressed in cylindrical coordinates as

$$\mathbf{F}(\mathbf{X}) = \begin{bmatrix} g'(R) & 0 \\ 0 & \frac{g(R)}{R} \end{bmatrix} = \begin{bmatrix} \frac{1}{G'(r)} & 0 \\ 0 & \frac{r}{G(r)} \end{bmatrix}, \tag{5.15}$$

where the superscript $\mathbf{^0}$ will not be indicated in the following for ease of notation. Thus,

$$\mathbf{C} = \frac{1}{J} \mathbf{F}\, \mathbf{C}^{(0)}\, \mathbf{F}^T, \ \ \rho = \frac{\rho_0}{J}, \tag{5.16}$$

with

$$J = \det \mathbf{F} = \frac{g'(R)\, g(R)}{R} = \frac{r}{G(r)G'(r)}. \tag{5.17}$$

The transformed Helmholtz eqn. (5.14) represents a linear anisotropic and inhomogeneous material. If $\mathbf{C}^{(0)}$ is isotropic, under transformation (5.11) the transformed material is radially anisotropic and the governing equation (5.14) takes the form

$$\frac{\partial^2 u}{\partial r^2} + \frac{G'(r)}{G(r)} \frac{\partial u}{\partial r} + \left[\frac{G'(r)}{G(r)}\right]^2 \frac{\partial^2 u}{\partial \theta^2} + [G'(r)\beta]^2 u = 0. \tag{5.18}$$

5.2 Dispersion properties

Here, we analyze dispersion properties for both original and transformed geometries. The dispersion properties have been computed both numerically, using the finite element package *Comsol Multiphysics 5.3*, and semi-analytically, implementing the multipole expansion method. The semi-analytical approach, while of more difficult implementation, shows in closed form the relationship between the dispersion properties of the original and transformed geometries and is used to obtain Dirac points through a recursive algorithm.

The multipole expansion method is fully detailed in [49, 50, 78]. For completeness, we briefly present the method in the following together with the application to the case of transformed geometry.

5.2.1 Multipole expansion method

The displacement is expressed by separation of variables. In the transformed geometry, the problem is governed by the equation of motion (5.18), and the displacement can be given by

$$u(r,\theta) = \begin{cases} \displaystyle\sum_{n=-\infty}^{\infty} \left[A_n^s J_n(\beta\, G(r)) + B_n^s H_n^{(1)}(\beta\, G(r))\right] e^{in\theta}\,, & \text{in} \quad \overline{\Omega'_{R_0,d}} \setminus \Omega'_{R_2,d}\,, \\ \displaystyle\sum_{n=-\infty}^{\infty} \left[A_n^m J_n(\beta\, r) + B_n^m H_n^{(1)}(\beta\, r)\right] e^{in\theta}, & \text{in} \quad \Omega_{R_0,d}\,. \end{cases} \tag{5.19}$$

In the shell domains $\overline{\Omega'_{R_0,d}} \setminus \Omega'_{R_2,d}$, $G(r)$ is as in eqn. (5.13). In (5.19) $H_n^{(1)} = J_n + iY_n$ is the Hankel function, J_n,Y_n are the Bessel functions of the first and second kind [84] and the unknown coefficients $A_n^{s,m}$, $B_n^{s,m}$ must be determined from the boundary and interface conditions. The superscripts m and s indicate the matrix and the shell domains.

The interface boundary conditions on $\partial\Omega_{R_0,d}$ ($r = R_0$), imposing continuity of displacements and shear tractions between the anisotropic shells and the isotropic matrix, imply that

$$A_n^m = A_n^s, \quad B_n^m = B_n^s, \qquad n \in \mathbb{Z}. \tag{5.20}$$

Neumann boundary conditions on $\partial\Omega_{R_2,d}$ ($r = R_2$, see Figure 5.1c) impose that

$$A_n^s = -\frac{H'^{(1)}_n(\beta G(R_2))}{J'_n(\beta G(R_2))} B_n^s, \qquad n \in \mathbb{Z}\,, \tag{5.21}$$

while quasi-periodicity conditions have been obtained from a Rayleigh identity [51, 85], giving

$$A_n^s = \sum_{l=-\infty}^{\infty} (-1)^{l-n} S^H_{l-n}(\beta, \mathbf{k}) B_n^s, \qquad n \in \mathbb{Z}\,. \tag{5.22}$$

The lattice sums have the following properties [50, 79–81]

$$\begin{aligned} S^H_{l-n}(\beta, \mathbf{k}) &= S^J_l(\beta, \mathbf{k}) + i S^Y_l(\beta, \mathbf{k}), \\ S^J_l(\beta, \mathbf{k}) &= -\delta_{l,0}, \\ S^Y_{-l}(\beta, \mathbf{k}) &= \left[S^Y_l(\beta, \mathbf{k})\right]^* \end{aligned}$$

with δ the Kronecker delta and $k = |\mathbf{k}|$ the magnitude of the Bloch vector. In [86] different ways of evaluating the non-trivial lattice sum are reviewed. Here, we adopt the representation given by Chin et al. [81], obtained by repeated integration to accelerate convergence

$$\begin{aligned} S^Y_l(\beta, \mathbf{k}) = -\frac{1}{J_{l+q}(\beta\lambda)} \Bigg(& \left[Y_q(\beta\lambda) + \frac{1}{\pi} \sum_{n=1}^{q} \frac{(q-n)!}{(n-1)!} \left(\frac{2}{\beta\lambda}\right)^{q-2n+2} \right] \delta_{l,0} + \\ & + 4 i^l \sum_{\substack{h_1,h_2=-\infty \\ \mathbf{h}\neq\mathbf{0}}}^{+\infty} \left(\frac{\beta d}{Q_{\mathbf{h}}}\right)^q \frac{J_{l+q}(Q_{\mathbf{h}}\lambda)}{Q_{\mathbf{h}}^2 - (\beta d)^2} e^{i l \eta_{\mathbf{h}}} \Bigg) \end{aligned} \tag{5.23}$$

where $\mathbf{Q_h} = (k_1 d + 2\pi h_1, k_2 d + 2\pi h_2)$ and $\eta_{\mathbf{h}} = \arctan(\mathbf{Q_h})$. The parameter λ is arbitrary and taken equal to d, the acceleration parameter q is typically chosen between 3 and 7 and, as shown in [51], increasing it makes the series converge more rapidly for large $Q_{\mathbf{h}}$, but delays the onset of rapide convergence; for our case, we took $q = 3$.

Notice that the singularities $Q_{\mathbf{h}}^2 - \beta^2 = 0$ correspond to the dispersion equation of a homogeneous plate.

Eqns. (5.21) and (5.22) lead to the following system

$$\left[\sum_{l=-\infty}^{\infty}(-1)^{l-n}S^{H}_{l-n}(\beta,\mathbf{k})J'_n(\beta G(R_2))+H'^{(1)}_n(\beta G(R_2))\right]B^s_n=0. \tag{5.24}$$

The system (5.24) has infinite dimension and is truncated at N to give the finite system

$$\mathbf{M}(\beta,\mathbf{k})\mathbf{B}=\mathbf{0}, \tag{5.25}$$

having dimension $(2N+1, 2N+1)$. The dispersion relation is the characteristic equation

$$\det[\mathbf{M}(\beta,\mathbf{k})]=0. \tag{5.26}$$

of the spectral problem (6.8).

For Dirichlet boundary conditions on $\partial\Omega_{R_2,d}$, first derivatives J'_n and $H'^{(1)}_n$ are substituted by J_n and $H^{(1)}_n$ in eqns. (5.21) and (5.24).

In the original geometry, where the problem is governed by the equation of motion (5.9), the displacement is given in the form

$$U(R,\Theta)=\sum_{n=-\infty}^{\infty}\left[A_nJ_n(\beta R)+B_nH^{(1)}_n(\beta R)\right]e^{in\Theta}. \tag{5.27}$$

The dispersion relation (5.26) is obtained following the procedure detailed in eqns. (5.21-5.26), where $G(R_2)$ is replaced by R_1 and A^s_n and B^s_n by A_n and B_n, respectively.

Dispersion surfaces have been computed fixing the wave vector $\mathbf{k}$ and searching for the frequencies satisfying the dispersion relation. A comparison between results obtained implementing the multipole expansion method and *Comsol Multiphysics* is reported in Appendix D.

5.2.2 Dispersion properties of transformed and untransformed domains

5.2.2.1 The case $R_0 < 0.5\,d$. Regular transformations

The dispersion properties of untransformed and transformed geometries are analysed here. In Figure 5.2, we compare the dispersion diagrams for the case in which

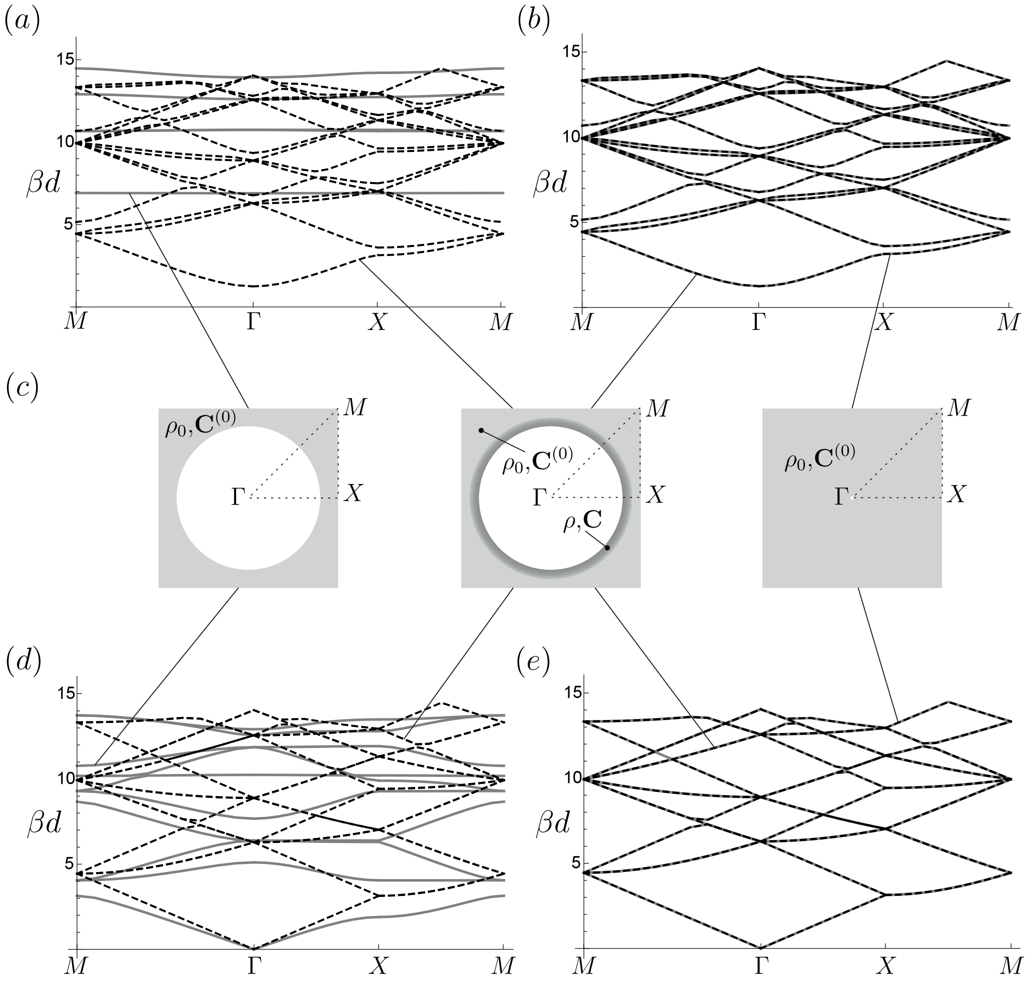

FIGURE 5.2: Dispersion diagrams. Results correspond to Dirichlet (a)-(b) and Neumann (d)-(e) boundary conditions in the central inclusions. (c) Homogeneous untransformed domains with internal radii $R_1/d = 0.4$ (left), $R_1/d = 0.005$ (right) and inhomogeneous transformed domain, with $R_0/d = 0.45$, $R_2/d = 0.4$, $R_1/d = 0.005$ (center). In the diagrams, grey continuous lines indicate untransformed geometries, dashed lines the transformed ones.

$R_0/d < 0.5$. In the transformed geometry $R_0/d = 0.45$, $R_1/d = 0.005$, $R_2/d = 0.4$. In the untransformed geometry, with homogeneous matrix, the internal relative radii of the holes are $R_1/d = 0.4$ and $R_1/d = 0.005$, respectively. Both Neumann and Dirichlet boundary conditions are considered at the internal void boundaries. Following [87], the usual path in the reciprocal space is taken, where $\Gamma = (0, 0)$, $X = (\pi/d, 0)$, $M = (\pi/d, \pi/d)$.

It is evident that the dispersion properties for untransformed and transformed geometries with the same voids' radii $R_1/d = 0.4$ and $R_2/d = 0.4$, respectively, are strongly different. This is clearly associated to the distribution of the mechanical properties in the non-homogeneous shells ($R_2 \leq r \leq R_0$). On the contrary, we show on the right column the perfect match between the dispersion diagrams of

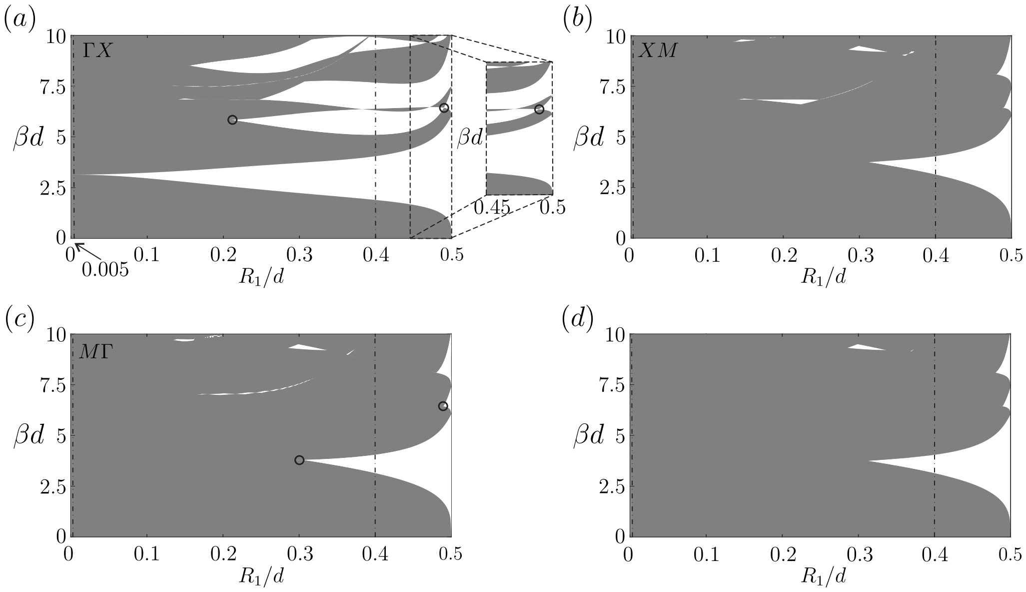

FIGURE 5.3: Band distribution of the periodic system as a function of the radius R_1/d. Grey regions are the pass bands along (a) ΓX, (b) XM, (c) $M\Gamma$ in the reciprocal space, in (d) the band distribution in the first Brillouin zone is reported. In the computation $R_0/d = 0.45$, $R_2/d = 0.4$. Some Dirac points are indicated in parts (a) and (c) with circles. The inset in part (a) shows a magnification with the Dirac point at $R_1/d = 0.489726$ and $\beta d = 6.43503$. Dot-dashed lines indicate the cases $R_1/d = 0.005$, 0.4.

the transformed geometry and the untransformed one with hole's radius $R_1/d = 0.005$. The agreement between dispersion curves for the transformed geometry and the untransformed one with $R_1/d = 0.005$ can be explained by considering the interface conditions at $r = R_0$ satisfied by the equalities (5.20) and that, in eqn. (5.21), $G(R_2) = R_1$, as imposed by the mapping (5.13).

Thus, we have shown that, implementing the geometric transformation detailed in Section 5.1.2, it is possible to mimic the dispersion properties of a periodic system with homogeneous matrix having holes of internal radius R_1, with a periodic system with non-homogeneous shells with internal radius R_2.

In the second part of the work, we are going to show several applications. In particular, in Figure 5.3, we report the band distribution, along the paths ΓX (a), XM (b) and $M\Gamma$ (c) and in the full first Brillouin zone (d) for Neumann boundary conditions at the voids. We see that, by modulating the transformation, it is possible to obtain the desired filtering properties increasing the reflectance or the transmittance in a broadband frequency interval. The dependence of the dispersion diagram on the radius R_1 can be also appreciated in the Figure 5.3.

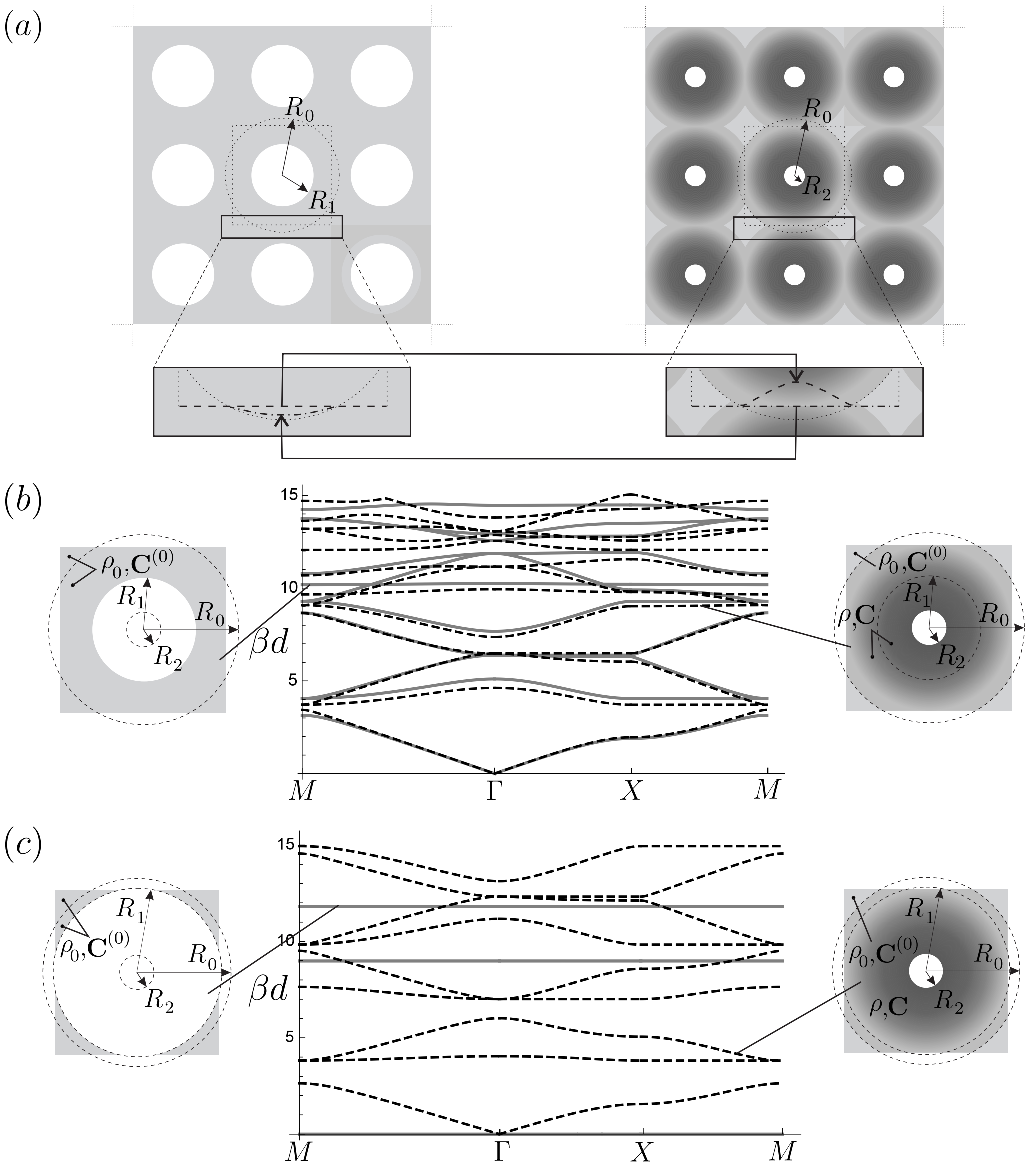

FIGURE 5.4: Overlapping transformation, $R_0 > 0.5\,d$. (a) Original and transformed geometries. In the inset the direct (5.11) and inverse (5.13) mappings of the boundaries of the central unit cell are shown in dashed and dashed-dotted lines, respectively. Dispersion diagrams for untransformed (grey lines) and transformed (black dashed lines) geometries: (b) $R_0 = 0.564\,d > 0.5\,d$, $R_1 = 0.4\,d < 0.5\,d$, $R_2 = 0.1\,d$. (c) $R_0 = 0.6\,d > 0.5\,d$, $R_1 = 0.55\,d > 0.5\,d$, $R_2 = 0.1\,d$.

5.2.2.2 The case $R_0 > 0.5\,d$. Overlapping transformations

In Figure 5.4 we show the comparisons between initial and transformed geometries in the case where the external radius $R_0 > 0.5\,d$. Two different initial geometries are considered: in part (a) $R_1 = 0.4\,d < 0.5\,d$, in part (b) $R_1 = 0.55\,d > 0.5\,d$. In the transformed geometries $R_2 = 0.1\,d$. It is evident that the dispersion diagrams show differences; this is due to the fact that the inhomogeneous shell $R_2 < r < R_0$ intersects the boundary of the unit cell and quasi-periodicity conditions are applied

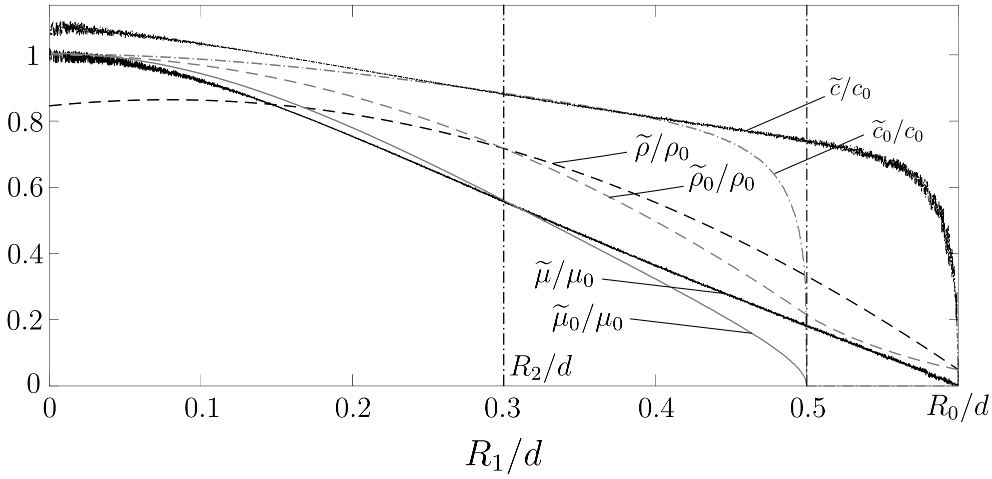

FIGURE 5.5: Effective properties in the quasi-static limit as a function of the radius R_1 (Figure 6.1). The effective density and shear moduli are given for the untransformed ($\widetilde{\rho}_0$ and $\widetilde{\mu}_0$) and transformed ($\widetilde{\rho}$ and $\widetilde{\mu}$) domains, together with the effective low-frequency phase velocities $\widetilde{c}$ and $\widetilde{c}_0$. The geometrical parameters $R_0 = 0.6\,d > 0.5\,d$, $R_2 = 0.3\,d$ are considered.

on two sets which are not mapped by the transformations (5.11) or (5.13). In the bottom of part (a) of Figure 5.4, it is possible to see the direct and inverse mapping of the boundary of the unit cell. We note from Figure 5.4 part (b) that, even in the case where the solid phase in the original geometry is not connected ($R_1 > 0.5\,d$), the dispersion properties of the transformed geometry maintain the 'classical' structure with stop and pass band of finite size. In particular, the local mechanical properties in the orthotropic domains are

$$\begin{aligned}\mu_r = C_{rr} &= \frac{G(r)}{G'(r)r}\mu_0 = \frac{r(R_0-R_1)+R_0(R_1-R_2)}{r(R_0-R_1)}\mu_0,\\ \mu_\theta = C_{\theta\theta} &= \frac{G'(r)r}{G(r)}\mu_0 = \frac{r(R_0-R_1)}{r(R_0-R_1)+R_0(R_1-R_2)}\mu_0,\end{aligned} \tag{5.28}$$

and

$$\rho = \frac{G'(r)G(r)}{r}\rho_0 = \frac{r(R_0-R_1)+R_0(R_1-R_2)}{r(R_0-R_2)^2}(R_0-R_1)\rho_0. \tag{5.29}$$

From eqns. (5.28) and (5.29), since $\min(R_2,R_0) \le r \le \max(R_2,R_0)$ and $\min(R_1,R_0) \le G(r) \le \max(R_1,R_0)$, r and $G(r)$ are always positive quantities. Thus, the positiveness of μ_r, μ_θ and ρ are governed by the factor $G'(r) = \alpha_1^{-1} = (R_0-R_1)/(R_0-R_2)$, which is also a positive quantity in the present and previous cases .

We also note the interesting relation $\mu_0 = \sqrt{\mu_r\mu_\theta}$, which is mathematically analogous to the exact result $\tilde{\mu} = \sqrt{\mu_1\mu_2}$ for the effective shear modulus $\tilde{\mu}$ of an isotropic bi-phase composite, with phase shear moduli μ_1 and μ_2, having material symmetry as, for example, a checkerboard structure. This was shown by Dykhne [88] for the conductivity problem, by making use of the 'phase interchange' relation [89, 90]. The same relation holds for the effective shear modulus of a macroscopically isotropic polycrystal, with periodically or randomly distributed microstructure, in which each anisotropic phase has principal shear moduli μ_1 and μ_2.

The effective properties in the quasi-static limit are shown in Figure 5.6. For the antiplane shear problem, the behavior is isotropic. The effective mass densities in the untransformed and transformed domains are

$$\tilde{\rho}_0 = \frac{1}{|\Omega^{(0,0)}_{R_1,d}|}\int_{\Omega^{(0,0)}_{R_1,d}} \rho_0 \, dA, \qquad \tilde{\rho} = \frac{1}{|\Omega^{(0,0)}_{R_2,d}|}\int_{\Omega^{(0,0)}_{R_2,d}} \rho \, dA. \tag{5.30}$$

The effective shear moduli have been computed by applying affine Dirichlet boundary conditions on the unit cell associated to a macroscopic strain $\tilde{\varepsilon}_{13}$ and evaluating the macroscopic stress

$$\tilde{\sigma}_{13} = \frac{1}{|\Omega^{(0,0)}_{R_i,d}|}\int_{\Omega^{(0,0)}_{R_i,d}} \sigma_{13} \, dA, \tag{5.31}$$

with $i = 1, 2$ in the original and transformed domains, respectively. Then,

$$\hat{\mu} = \frac{\tilde{\sigma}_{13}}{\tilde{\varepsilon}_{13}} \tag{5.32}$$

where $\hat{\mu}$ is $\tilde{\mu}_0$ or $\tilde{\mu}$. The effective shear modulus can be computed numerically or semi-analytically following the homogenisation scheme detailed in [91, 92].

As expected, the effective properties are not negative; $\tilde{\rho} > \tilde{\rho}_0$ and $\tilde{\mu} > \tilde{\mu}_0$ ($\tilde{\rho} < \tilde{\rho}_0$ and $\tilde{\mu} < \tilde{\mu}_0$) for $R_1 > R_2$ ($R_1 < R_2$). When $R_1/d > 0.5$, $\tilde{\mu}_0 = 0$, since the homogeneous solid phase is not connected.

The results on the transformed geometry show how it is possible to easily tune, at least in the quasi-static regime, the effective mechanical properties of the periodic system. If we compare two periodic systems with the same internal radius R_2, the first with a homogeneous solid phase and the second with a functionally graded material interface designed following the geometric transformation (5.13), we see that by tuning the geometrical parameter of the transformation and, in particular R_1, we can stiffen the composite ($R_1 < R_2$) or soften it ($R_1 > R_2$) up to the limit

$R_1 \to R_0$, when the transformation (5.11) is singular and the group and phase velocities approach zero in the quasi-static limit.

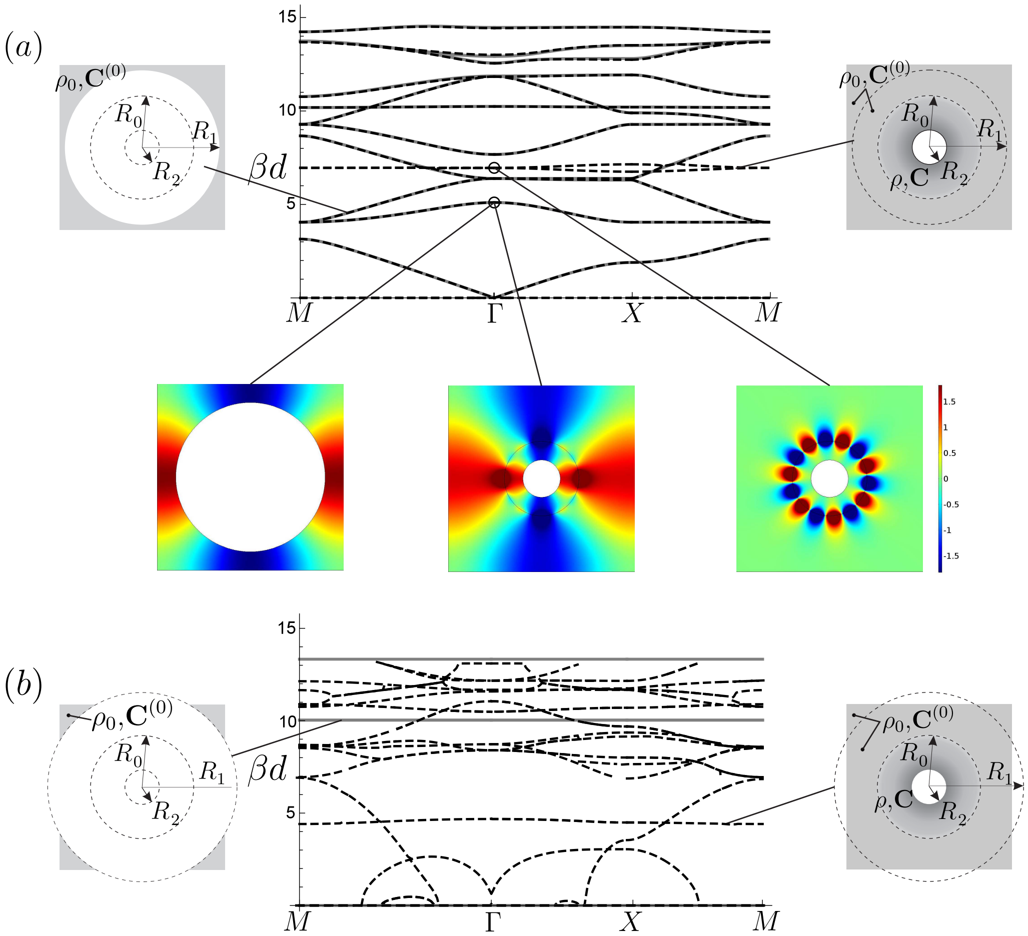

FIGURE 5.6: Unfolding transformation. Comparisons of dispersion diagrams for untransformed (grey lines) and transformed (black dashed lines) domains. (a) $R_1 = 0.4\,d < 0.5\,d$, $R_0 = 0.2\,d$, $R_2 = 0.1\,d$. (b) $R_1 = 0.564\,d > 0.5\,d$, $R_0 = 0.4\,d$, $R_2 = 0.1\,d$.

5.2.2.3 The case $R_1 > R_0$. Unfolding transformation

We consider now an unfolding transformation corresponding to $R_1 > R_0 > R_2$. The initial and transformed geometries are shown in Figure 5.6, part (a), when $R_1/d < 0.5$. In the unit cell, the solid phase in the transformed geometry is homogenous for $r > R_0$ and inhomogeneous in the shell $R_2 \leq r \leq R_0$, with local properties defined as in eqns. (5.28) and (5.29). Since $G'(r)$ is now negative, the density and shear modulus are negative in the shell. The reader can now argue if it makes physical sense to have negative properties. In order to answer this question, we first follow the Veselago approach, who proposed in 1968 a theoretical model concerning the electrodynamics properties of materials with simultaneously negative dielectric permittivity and magnetic permeability [6]. Nevertheless, negative index materials addressed as left-handed material, backward-wave media, double negative metamaterials were proposed only after three decades [1, 93, 94]. In general relativity, the concept of negative inertial and gravitational masses is known [95]. In Newtonian mechanics a negative stiffness can be found in the incremental behavior of a nonlinear system: the snap-through mechanism is probably the simplest example of a multi-stable structural system that, due to geometric nonlinearity, may show an incremental negative stiffness in a specific range of deformation. Alternatively, by structuring the microstructure on a scale which is small compared to the wavelength, it is possible to obtain negative properties on the mesoscale, in particular, in the dynamic regimes where internal resonances can occur [96–98].

In Figure 5.6 we compare the dispersion diagrams for untransformed and transformed domains. In part (a) the case $R_1 < 0.5\,d$ is reported; we note that the periodic system with inhomogeneous solid phase is capable to reproduce the same dispersion curves as the untransformed one, plus some additional ones. In the considered example, the additional curves are at $\beta d = 0$ and at a finite frequency $\beta d = 6.95$. Some of the eigenmodes at $\mathbf{k} = (0, 0)$ are also shown in Figure 5.6a. The two eigenmodes at $\beta d = 5.10$ have the same displacement distribution in the region $r > R_0$. In addition, for the transformed case, $u(r_A) = u(r_B)$, when $R_2 \leq r_A = g(r_B) \leq R_0$.

The eigenmode on the bottom right of Figure 5.6a is associated to the two additional dispersion curves at $\beta d \simeq 6.95$. It represents an anomalous localised resonance, also named plasmonic resonance in electromagnetism. They have been studied in electromagnetism in the quasi-static limit for a single coated inclusion [44], a square array of coated cylinders [43] and regular and disordered arrangements of coated cylinders and spheres [99]. In the quasi-static limit, Milton et al. [46, 100] have shown that the resonant field generated by a polarizable line or point dipole acts back on the polarizable line or point dipole and effectively cancels the field acting on it from outside sources. The dispersion curves for the transformed case at $\beta d \simeq 0$ confirm the quasi-static results in the literature. The analysis has been extended to consider the effect of a finite wavelength for a single coated inclusion with homogeneous shell in [45] and numerical analyses at finite frequencies for different geometric transformations are given in [101]. In the following, we report the result of a semi-analytical approach. In order to better evidence the anomalous resonance effect, we consider the unfolding transformation on a single inclusion.

Anomalous localized resonance. A single hole of radius R_2 in a infinite domain is considered. The hole is surrounded by a non-homogeneous shell with internal radius R_2 and external one R_0. The external matrix $r > R_0$ is homogeneous. The matrix has shear modulus μ_0 and density ρ_0, the shear modulus and the density in the shell are given by eqns. (5.28) and (5.29), with $R_2/R_0 = 0.5$ and $R_1/R_0 = 1.35 > 1$. A concentrated load is applied at $\mathbf{x}_F$, where $\mathbf{x}_F = (r_F, \theta_F)$, with $r_F = 3R_0/2$ and $\theta_F = \pi/4$, in cylindrical coordinates. The Green's function for Helmholtz equation describing the out of plane shear problem is

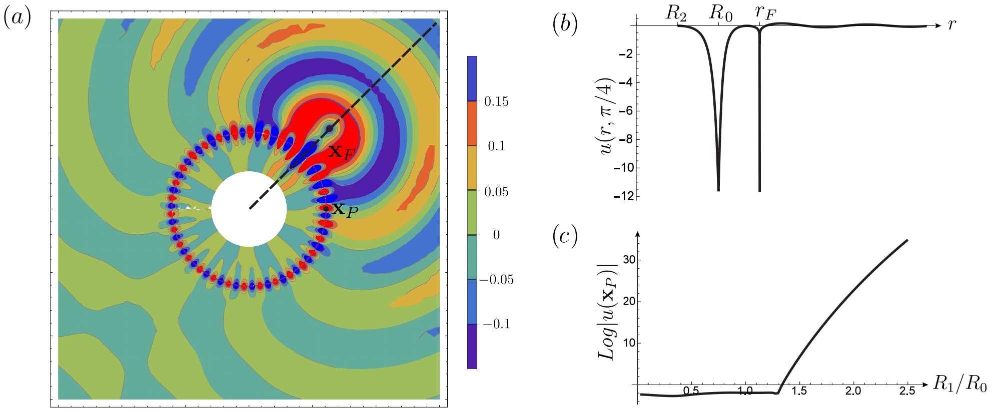

FIGURE 5.7: Anomalous localised resonance as a result of the unfolding transformation. (a) Contour plot of the displacement u is given for $R_2/R_0 = 0.5$ and $R_1/R_0 = 1.35$. (b) Displacement distribution along the dashed line indicated in part (a). (c) Displacement amplitude in the point $\mathbf{x}_P$ as a function of the ratio R_1/R_0.

$$F(\hat{r}) = -\frac{i}{4} H_0^{(1)}(\beta \hat{r}), \tag{5.33}$$

where $\hat{r} = |\mathbf{x} - \mathbf{x}_F|$. The general solution is

$$\begin{cases} u^s(r,\theta) = \displaystyle\sum_{n=-\infty}^{\infty} \left[A_n^s J_n(\beta\, G(r)) + B_n^s H_n^{(1)}(\beta\, G(r)) \right] e^{in\theta}\,, \quad \text{for} \quad r < R_0\,, \\ u^m(r,\theta) = \displaystyle\sum_{n=-\infty}^{\infty} \left[A_n^m J_n(\beta r) + B_n^m H_n^{(1)}(\beta\, r) \right] e^{in\theta}, \quad \text{for} \quad r > R_0\,. \end{cases} \tag{5.34}$$

Using the Graf's addition theorem [84], the Hankel function in eqn. (5.33) can be expressed as

$$H_0^{(1)}(\beta \hat{r}) = \sum_{n=-\infty}^{\infty} H_0^{(1)}(\beta r_F) J_n(\beta r) e^{in(\pi - \theta + \theta_F)}, \tag{5.35}$$

for $r < r_F$, leading to

$$A_n^m = 0.25\, i\, (-1)^{n+1} H_n^{(1)}(\beta r_F) e^{-in\theta_F}. \tag{5.36}$$

The remaining coefficients are obtained from the interface conditions

$$u^m(R_0, \theta) = u^s(R_0, \theta), \qquad \mu_0 \frac{\partial u^m}{\partial r}\bigg|_{r=R_0} = \mu \, \frac{\partial u^s}{\partial r}\bigg|_{r=R_0}, \tag{5.37}$$

and the Neumann boundary condition

$$\mu \, \frac{\partial u^s}{\partial r}\bigg|_{r=R_2} = 0. \tag{5.38}$$

They have the following expressions

$$\begin{aligned} A_n^s &= 0.25\, i\, (-1)^{n+1}\, H_n^{(1)}(\beta r_F) e^{-in\theta_F}, \\ B_n^s &= B_n^m = -\frac{J_{n+1}(\beta R_1) - J_{n-1}(\beta R_1)}{H_{n+1}^{(1)}(\beta R_1) - H_{n-1}^{(1)}(\beta R_1)} A_n^s. \end{aligned} \tag{5.39}$$

The real part of the displacement $u(r, \theta)$ is shown in Figure 5.7. In the computation, the sums in the representation (5.34) have been truncated at $N = 30$ and $\beta r_F = 6$. The amplitude amplification in the neighborhood of the interface between the shell and the external matrix ($r = R_0$) is fully visible both from the contour plot in part (a) and the displacement distribution in part (b), shown along the radial line indicated in part (a) of Figure 5.7. In order to show the effect of unfolding in part (c) of the figure, the displacement amplitude in the point $\mathbf{x}_P = (R_0, 0)$ indicated in part (a), is given as a function of the initial radius R_1. We remember that unfolding corresponds to $R_1/R_0 > 1$. The results, in logarithmic scale, indicated an amplification on the shell-matrix interface when $R_1/R_0 \gtrsim 1.3$. We obtained an amplification at approximately the same threshold also for $\beta r_F = 12$ and $\beta r_F = 30$.

The case $R_1 > d/2 > R_0$. The dispersion diagrams for the case of unfolding transformation, where the initial radius R_1 is greater than the half-dimension $d/2$ of the unit cell, is shown in Figure 5.6b. As for the case of regular transformation reported in Figure 5.4b, the dispersion diagrams before and after transformation are strongly different. In this case, there are additional interesting features at low-frequency. First of all, some of the branches intersect the zero frequency axis

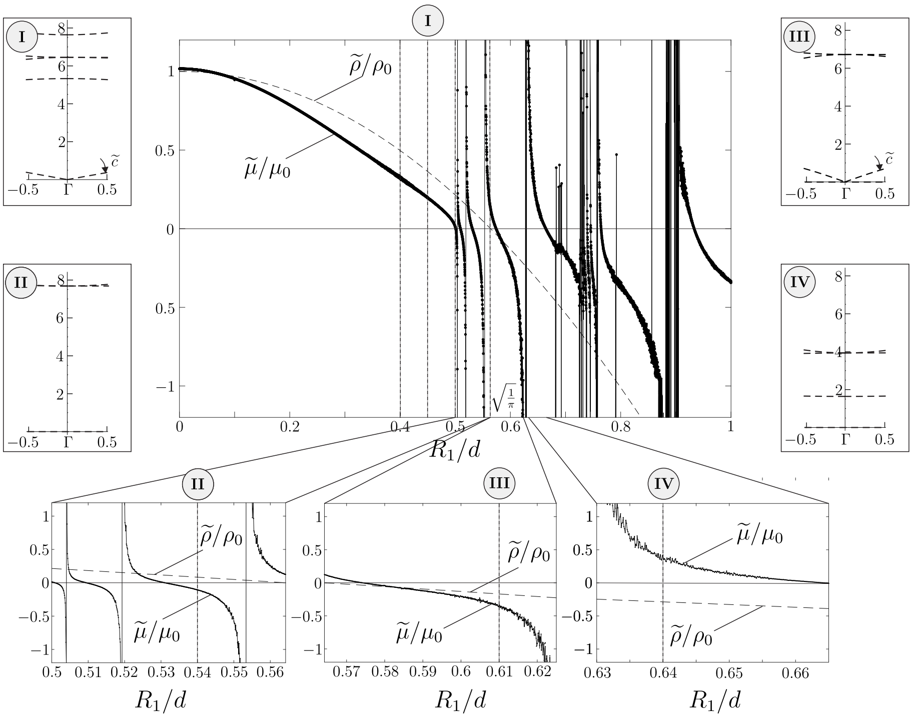

FIGURE 5.8: Low-frequency effective shear modulus and density as a function of the radius R_1. Results are given for $R_0 = 0.4\,d$, $R_2 = 0.1\,d$. Solid and dashed lines correspond to relative effective shear modulus $\widetilde{\mu}/\mu_0$ and density $\widetilde{\rho}/\rho_0$, respectively. Scaled curves are given at the bottom. The dispersion diagrams in the neighborhood of Γ are given in the four insets indicated with roman numbers **I**, **II**, **III** and **IV**; the corresponding values of R_1/d are also reported with dashed-dotted lines in the $\widetilde{\mu}/\mu_0$, $\widetilde{\rho}/\rho_0$ vs R_1/d plots.

$\beta d = 0$ at finite amplitudes of the wavenumber **k** within the irreducible Brillouin zone. In prestressed flexural beams or plates such points indicate static buckling [102]; here, they are associated to anomalous internal resonance at zero frequency.

In addition, it appears that changing the initial radius R_1, it is possible to modulate the phase and group velocity in the low-frequency $\beta d \to 0$, low wavenumber $\mathbf{k} \to \mathbf{0}$ limit. In this regime, the homogenised shear modulus $\widetilde{\mu}$ and density $\widetilde{\rho}$ are shown in Figure 5.8 as a function of the initial radius R_1, where $R_0 = 0.4\,d$ and $R_2 = 0.1\,d$. They have been computed following the procedure detailed at the end of Section 5.2.2.2, eqns. (5.30.2) and (5.32). In particular, when $R_0 < d/2$,

$$\widetilde{\rho} = \rho_0 \left(1 - \frac{\pi R_1^2}{d^2}\right). \tag{5.40}$$

The results show that both $\widetilde{\mu}$ and $\widetilde{\rho}$ can change in sign. Thus, there is the possibility to have propagation, when $\widetilde{\mu}/\widetilde{\rho} > 0$, or no propagation, when $\widetilde{\mu}/\widetilde{\rho} < 0$. Note that negative values of $\widetilde{\mu}$ and $\widetilde{\rho}$ have been associated to a negative refractive index

[103]. Different cases are shown in the four insets in Figure 5.8, indicated with the roman numbers **I**, **II**, **III** and **IV**. The dispersion curves correspond to the different values of R_1/d, indicated with dashed-dotted lines, labelled with the same roman numbers in the effective properties plots of Figure 5.8. At $R_1/d = 0.45$ (case **I**) and $R_1/d = 0.61$ (case **III**), there are locally linear dispersion curves departing from Γ at $\beta d = 0$, with phase and group velocity $\widetilde{c} = \sqrt{\widetilde{\mu}/\widetilde{\rho}}$, since in case **I** both $\widetilde{\mu}$ and $\widetilde{\rho}$ are positive and in case **III** both properties are negative. At $R_1/d = 0.54$ (case **II**) and $R_1/d = 0.64$ (case **IV**), a low-frequency finite stop band is present in the neighborhood of Γ, since $\widetilde{\mu} \lesseqgtr 0$ and $\widetilde{\rho} \gtreqless 0$ in cases **II** and **IV**, respectively. Note also that a zero frequency curve is present when $\widetilde{\mu} < 0$ or $\widetilde{\rho} < 0$.

Finally, we stress that the initial radius R_1 can be used as a design parameter in order to modulate the low-frequency phase and group velocities in the neighborhood of Γ, ranging from low or zero values when $\widetilde{\mu} \to 0$ to large or unbounded ones when $\widetilde{\rho} \to 0$.

5.3 Numerical results

In this Section, we show possible implementations of the proposed design based on periodic transformation.

5.3.1 Transmission problem in an infinite medium

The transmission problem for a slab composed of three layers of inclusions surrounded by non-homogeneous shells is analysed numerically. The computational domain is shown in Figure 5.9a. The incident wave has the angle of incidence $\theta_I = \pi/6$, while the mechanical properties of the shells are designed following the transformation (5.11). In part (c) the parameters are $R_1/d = 2.2\bar{2} \cdot 10^{-4}$, $R_2/d = 0.22\bar{2}$, $R_0/4 = 0.44\bar{4}$, while in part (d) $R_1/d = 0.44\bar{4}$, $R_2/d = 9.88 \cdot 10^{-3}$, $R_0/d = 0.494$.

The numerical models have been implemented in *Comsol Multiphysics 5.3*. Details on the implementation of the numerical code are reported in Appendices C and E. We applied an incident Gaussian beam u_I and computed the scattered field u_S; the total field $u = u_I + u_S$ is shown in Figure 5.9 parts (b), (c) and (d) and Figure

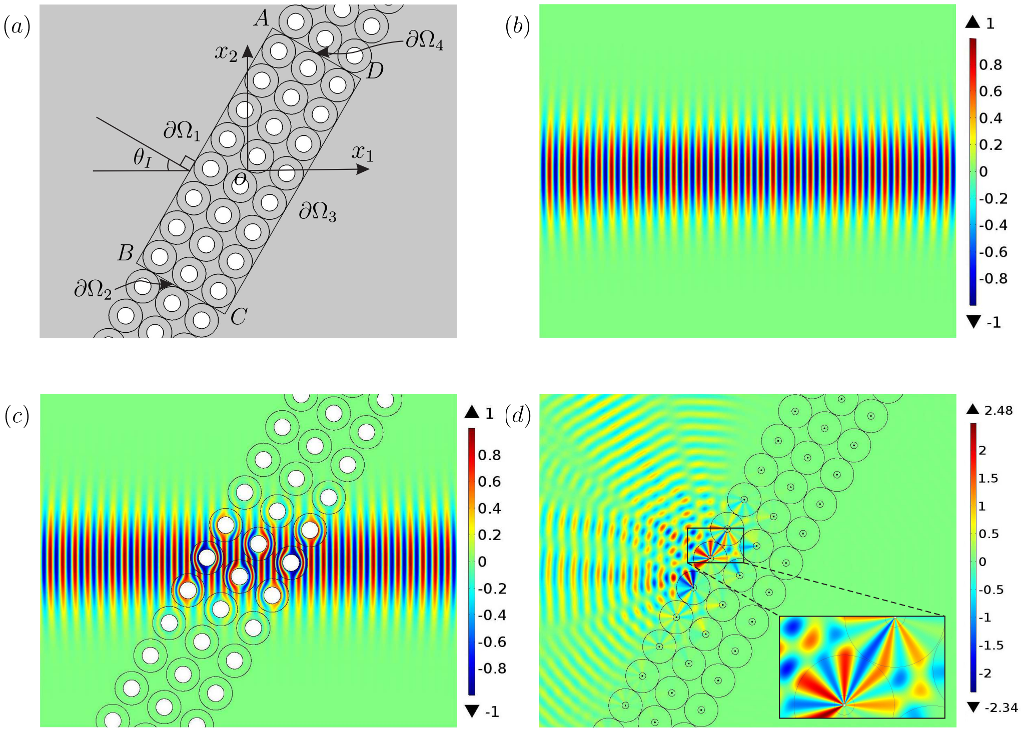

FIGURE 5.9: Transmission problem. (a) Computational domain for an oblique incident wave with angle of incidence θ_I. The interface is composed of three layers of inclusions surrounded by non-homogeneous shells. The power flux has been computed along the edges $\partial\Omega_1$, $\partial\Omega_2$, $\partial\Omega_3$ and $\partial\Omega_4$ of the rectangle $ABCD$. (b) Displacement generated by Gaussian beam in a homogeneous domain (see eqn. (5.41)). (c), (d) Displacement generated by a Gaussian beam interfering with the slab. The shells parameters are: (c) $R_1/d = 2.2\bar{2} \cdot 10^{-4}$, $R_2/d = 0.22\bar{2}$, $R_0/d = 0.44\bar{4}$, (d) $R_1/d = 0.44\bar{4}$, $R_2/d = 9.88 \cdot 10^{-3}$, $R_0/d = 0.494$. The size of the computational domain is $(12d \times 10d)$.

1.1, with $\beta d = 17.2$. Non-scattering boundary conditions are imposed on the external boundary of the computational domain. The Gaussian beam in cartesian coordinates is given by

$$u_I(x_1, x_2) = \left(1+\xi^2\right)^{-\frac{1}{4}} \exp\left[-\frac{x_2^2}{b_0^2(1+\xi^2)}\right] \exp\left[-i\left(\beta x_1 + \beta\frac{x_2^2}{2\chi} - \frac{\arctan\xi}{2}\right)\right] \tag{5.41}$$

where $\chi = x_1(1+\xi^{-2})$ is the radius of curvature of the beam's wavefront at x_1, $\xi = x_1/x_0$, $x_0 = \beta\, b_0^2/2$, with b_0 the beam or waist radius. In the computations, we assumed $b_0 = 1.25d$. The propagation of a Gaussian beam in a homogeneous medium is reported in Figure 5.9b.

In Figure 5.9c we show the results where the interface is an array of holes of finite size $R_2/d = 0.22\bar{2}$. The comparative results with the homogeneous case in Figure 5.9b show a negligible scattering produced by the interface associated to nearly full transmission. On the contrary in Figure 5.9d we show the results where the interface is an array of holes of negligibly small size $R_2/d = 9.88 \cdot 10^{-3}$. In such case, as a result of the design introduced by the geometric transformation, the interface is capable to reflect the incoming wave to a large extent. Thus, the slab can be designed in order to cloak the array of holes or as a full reflecting interface.

In Figure 1.1 we show that it is possible to obtain practically full transmission, also in the extreme case of very large holes, where $R_2/d = 0.44\bar{4}$, with $R_1/d = 2.47 \cdot 10^{-4}$ and $R_0/d = 0.494$. In the inset of the figure, it is possible to recognize from the contour plot of the displacement distribution, that the Gaussian beam can propagate in the homogeneous part of the slab practically undistorted, while in the transformed shells around each void inclusion $u(\mathbf{x}) = u(\mathcal{F}(\mathbf{X}))$.

5.3.1.1 Power flow

The performance in term of transmission and reflection has been assessed quantitatively by determining the power flow of the mechanical wave throughout the boundaries $\partial\Omega_i$ $(i = 1, \cdots, 4)$ of the rectangular domain $ABCD$, indicated in Figure 5.9a. The time-averaged (over a period $T = 2\pi/\omega$) rate of energy flux passing through a surface, with local outward normal $\mathbf{n}$, in a position $\mathbf{x}$, is [104]

$$P(\mathbf{x}) = \frac{1}{2} Re[\tau_{3j} n_j \dot{u}^*], \quad j = 1, 2\,, \tag{5.42}$$

where $\tau_{3j} = \mu \partial u/\partial x_j$ are the out of plane shear stress components, $\dot{u}^*$ the complex conjugate of velocity and n_j the components of the normal to the surface. Then, the power flow (per unit thickness) across each boundary $\partial\Omega_i$ $(i = 1, \cdots, 4)$, is calculated integrating the local flow per unit area as follows

$$\mathcal{P}_i = \int_{\partial\Omega_i} P ds, \tag{5.43}$$

where s is a local curvilinear coordinate defined in each boundary $\partial\Omega_i$. All the fluxes have been normalised by the power flow across $\partial\Omega_3$ in the homogenous case $\mathcal{P}_3^H$ (see Figure 5.9b), therefore

$$\hat{\mathcal{P}}_i = \frac{\mathcal{P}_i}{\mathcal{P}_3^H}. \tag{5.44}$$

The power flow $\mathcal{P}_3^H$ can be easily computed for a propagating Gaussian beam from the expression (5.41); the length of the boundary $\partial\Omega_3$ have been fixed in order to have a difference less than 1% with respect to a straight boundary $\partial\Omega_3^\infty \supset \partial\Omega_3$ of infinite length. In the following, when this condition is not satisfied, results will not be shown. The normals $\mathbf{n}_i$ to $\partial\Omega_i$ $(i = 1, \cdots, 4)$ are as follows

$$\mathbf{n}_{1,3} = (\mp\cos\theta_I, \pm\sin\theta_I)^T, \qquad \mathbf{n}_{2,4} = (\mp\sin\theta_I, \mp\cos\theta_I)^T . \tag{5.45}$$

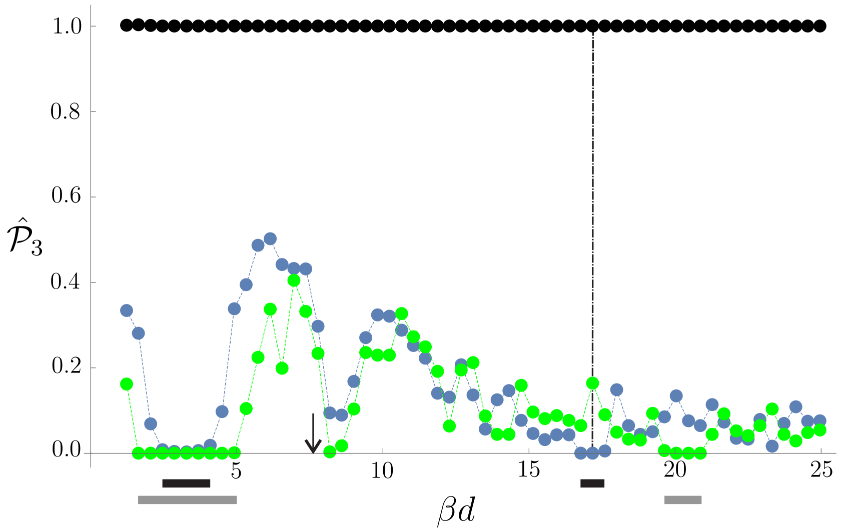

FIGURE 5.10: Rate of transmitted energy $\hat{\mathcal{P}}_3$ across $\partial\Omega_3$ as a function of the normalised frequency βd. Black dots correspond to Figure 5.9c, blue dots to Figure 5.9d, green dots to the same parameter of Figure 5.9d except for $R_1/d = 0.484$. The dash-dotted line corresponds to the frequency $\beta d = 17.2$ adopted in Figure 5.9. Thick black and grey lines at the bottom indicate the partial stop band intervals.

We identify with $\hat{\mathcal{P}}_3$ the transmitted power flow, while $\hat{\mathcal{P}}_2$ and $\hat{\mathcal{P}}_4$ give an indication of the energy radiated into the interface. The transmitted power flow $\hat{\mathcal{P}}_3$ is shown in Figure 5.10 as a function of the normalised frequency βd. From the black points, we note that when the small void inclusions of radius $R_1/d = 2.2\bar{2} \cdot 10^{-4}$ are mapped to the larger inclusions of radius $R_2/d = 0.22\bar{2}$ the transmitted flow $\hat{\mathcal{P}}_3 \simeq 1$ at all frequencies, meaning that the Gaussian beam can propagate within the slab practically unperturbed, in the all frequency spectrum that we have considered. On the contrary, when initial relatively large voids of radius $R_1/d = 0.44\bar{4}$ are mapped into the small voids of radius $R_2/d = 9.88 \cdot 10^{-3}$ (blue dots in Figure 5.10), high reflectance is generated. The reflection is maximized in the frequency intervals corresponding to the stop bands of the periodic structure for propagation along the direction determined by the angle θ_I of the incident wave. They roughly correspond to the frequencies where $\hat{\mathcal{P}}_3 \simeq 0$. In any case, in the considered frequency spectrum, $\hat{\mathcal{P}}_3 < 0.5$. By varying the initial radius R_1, it is possible to modulate the amount of reflection; in Figure 5.10 we have shown in green dots the results for the case where the final geometry is the same, but the properties of the shells surrounding the voids are designed from the different initial radius $R_1/d = 0.484$. As a results, it is possible to decrease the amount of transmission with respect to the previous case (see $\beta d = 8.2$), to increase the frequency interval corresponding to negligible transmission (see $1.6 < \beta d < 4.9$), but also to shift such frequency interval (see $16.8 < \beta d < 17.6$ and $19.6 < \beta d < 20.9$).

In all the performed computations $\hat{\mathcal{P}}_2$ and $\hat{\mathcal{P}}_4$ are negligible, their moduli being always less than 10^{-5}. While they cancel each other when there is high transmission, namely $\hat{\mathcal{P}}_4 \simeq -\hat{\mathcal{P}}_2$, they are both positive when there is high reflection indicating, albeit small, some radiation into the interface.

5.3.2 Waveguides

In this Section, we consider out of plane elastic waves propagating along the longitudinal direction x_1 in a two dimensional waveguide of width d. The upper and lower boundaries at $x_2 = \pm d/2$ are clamped.

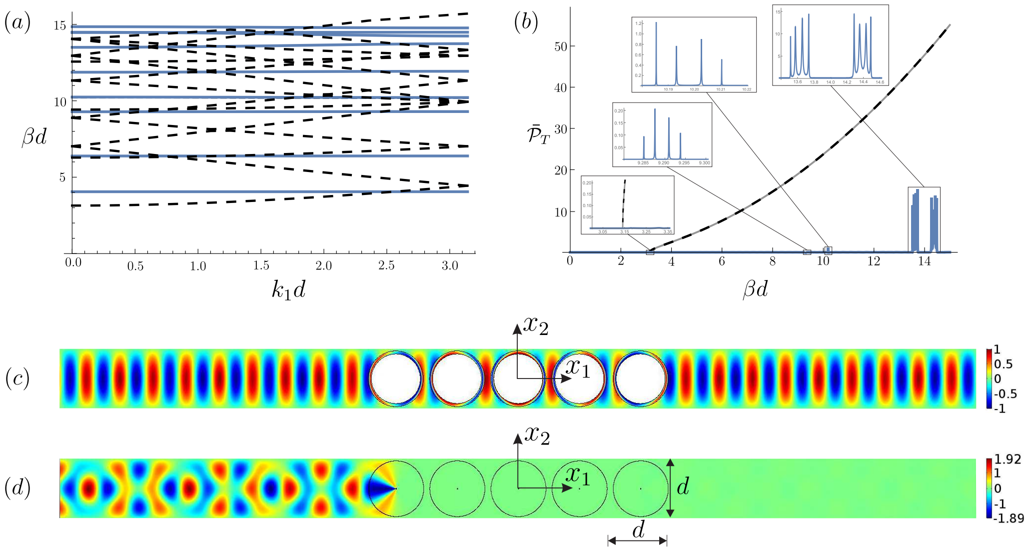

FIGURE 5.11: Wave propagation in a waveguide throughout a five units interface. (a) Dispersion curves for propagation along direction x_1. (b) Transmitted power flow $\bar{\mathcal{P}}_T = \mathcal{P}d/(c_0\mu_0)$ as a function of the normalised frequency βd. (c), (d) Out of plane displacement field for an incident wave $u_I = Re[u_1]$ (see eqn.(5.46)), with $\beta d = 12$. Black dashed lines and part (c) correspond to $R_1/d = 0.005$, $R_2/d = 0.4$ and $R_0/d = 0.45$, blue lines and part (d) to $R_1/d = 0.4$, $R_2/d = 0.005$ and $R_0/d = 0.45$ and the gray line in part (b) to the homogeneous waveguide.

The propagating wave in the homogeneous waveguide has the form [105]

$$u_n(x_1, x_2) = e^{ik_1 x_1} f_n(x_2)\,, \tag{5.46}$$

where the real wavenumber

$$k_1 = \sqrt{\beta^2 - n^2\pi^2/d^2}, \quad n \in \mathbb{N}\,, \tag{5.47}$$

and

$$f_{2m-1}(x_2) = \cos\left(\frac{(2m-1)\pi x_2}{d}\right), \quad f_{2m}(x_2) = \sin\left(\frac{2m\pi x_2}{d}\right), \quad m = 1, 2, \cdots . \tag{5.48}$$

We introduce into the waveguide a 5 units interface. Each unit has a void inclusion surrounded by a shell having material parameters defined by means of the geometric transformation (5.11). On the void inclusion Neumann boundary conditions are applied, while on the upper and lower boundaries of each cell (where $\mathbf{n} = (0, \pm 1)$) Dirichlet boundary conditions are imposed.

The numerical computations have been performed in *Comsol Multiphysics 5.3*, with non reflecting boundary conditions imposed on the left and right boundaries (where $\mathbf{n} = (\pm 1, 0)$) for the transmission problem.

In Figure 5.11c, we consider large voids of radius $R_2/d = 0.4$. The dispersion diagram, shown in black dashed lines in part (a), approaches the dispersion diagram for a homogeneous waveguide, for which the dispersion relation satisfies eqn. (5.47).

For the transmission problem, we consider the incident wave

$$u_I = u_1 = e^{ik_1 x_1} \cos\left(\frac{\pi x_2}{d}\right), \tag{5.49}$$

with $k_1 = \sqrt{\beta^2 - \pi^2/d^2}$. Again, the wave propagates throughout the interface without any evident perturbation, showing full transmission with the shells acting as cloaking interfaces. The full transmission is detailed in Figure 5.11b, where the curve showing transmitted power flow in the waveguide with large voids (dashed black line) is practically coincident with the transmitted power flow in a homogeneous waveguide (grey line). In the homogeneous waveguide, following the eqns. (5.43) and (5.44), the transmitted power flow throughout a generic cross-section

$x_1 = \text{const}$, is [2]

$$\mathcal{P} = \frac{\mu_0\, c_0}{4d} Re[\beta d \sqrt{(\beta d)^2 - \pi^2}], \tag{5.50}$$

which is positive above the cutoff frequency $\beta d = \pi$.

The opposite behavior is retrieved in Figure 5.11d, where the case of small voids of radius $R_2/d = 0.005$ is studied. The dispersion properties, shown in blue lines in part (a), evidence large stop bands separated by tiny pass bands, characterised by nearly horizontal dispersion curves. The transmission problem in part (d) evidences the capability of the interface to reflect the incident wave. In Figure 5.11b we show (in blue lines) that the reflection is maximised in the full frequency interval and to a much larger amount with respect to the continuous case analysed in Section 5.3.1.1. In the insets of Figure 5.11b, we also detailed the typical Fabry-Perot resonance oscillations in correspondence of the tiny pass bands and the transmitted flow in the neighborhood of the cutoff frequency.

5.3.2.1 Defect modes

Here, we consider the same infinite waveguide with small voids as in Figure 5.11d, with an interface with units obtained employing the transformation (5.11), with $R_1/d = 0.4$, $R_2/d = 0.005$ and $R_0/d = 0.45$. With respect to the previous case, we do not introduce the central unit, so that the waveguide is homogeneous in the domain $(x_1, x_2) \in (-d/2, d/2) \times (-d/2, d/2)$.

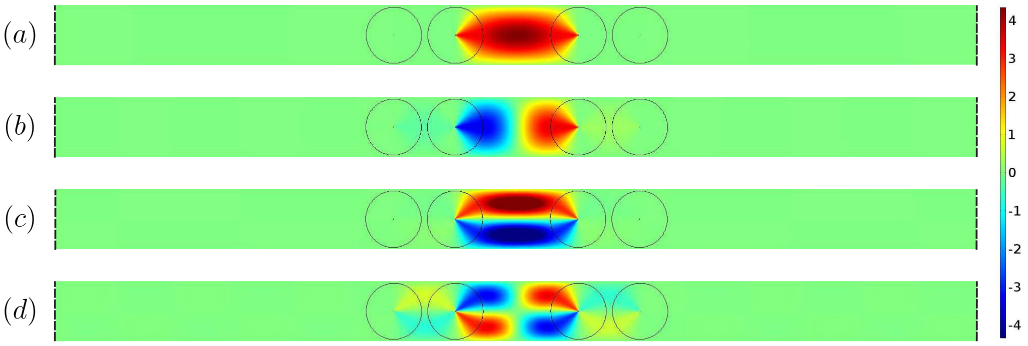

FIGURE 5.12: Defect modes in an infinite waveguide. The modes correspond to (a) $\beta d = 3.38$, (b) $\beta d = 4.40$, (c) $\beta d = 6.47$ and (d) $\beta d = 7.09$.

---

[2] In this case, we preferred not to show the normalised values, since in the homogenous case the power flow can be zero.

The infinite waveguide present a set of distinct internal resonance or defect modes, some of which, symmetric and skew-symmetric about the x_1 and x_2 axes, are shown in Figure 5.12.

These modes are generated by the inhomogeneous and anisotropic distribution of mechanical parameters designed following (5.11), since in a homogeneous waveguide, with the same four voids, these defect modes are not present, at last in the broad frequency interval $0 \leq \beta d \leq 15$.

5.3.3 Dirac Points

The dispersion diagrams for the periodic system may evidence Dirac points [106], where the system (6.8) displays degeneracies. From Dirac points at least two dispersion surfaces emerge as Dirac cones or Dirac-like cones [107], with finite group velocities at their vertices. The case of multiple Dirac-like cones at one Dirac point has been shown in [108].

In Figure 5.13 a Dirac point is shown. The presence of these points is associated with particular values of the initial radius R_1; the existence and the emergence of these points can be also retrieved from the Figure **??**.

Here, fixing the final geometry ($R_2/d = 0.375$, $R_0/d = 0.4$), we search for the properties in the shells $R_2 \leq r \leq R_0$ leading to Dirac points by changing the parameter R_1.

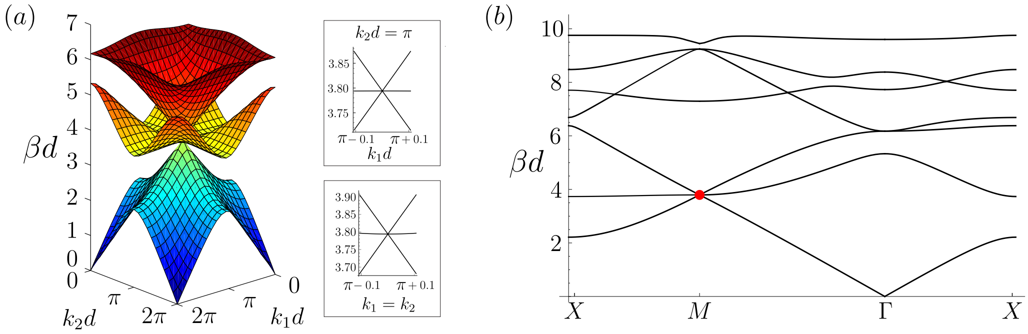

FIGURE 5.13: (a) First three dispersion surfaces with a Dirac cone at M and $\beta d = 3.79409$. (b) Dispersion diagram with Dirac point (red point). The initial radius is $R_1/d = 0.305318$. In the insets of part (a) cross sections of the dispersion surfaces are shown.

In this respect, it was convenient to make use of the multipole expansion method together with the Meylan approach [82] to find the targeted values of R_1. Dirac points are located at Γ and M in the reciprocal space. Fixing the position in the reciprocal space, we started with small values of $R_1/d = 0.005$, iterating on R_1 up to the values at which multiple eigenfrequencies were found. The coincidence of eigenfrequencies was checked up to the first 7 digits. The multipole expansion method was implemented with $N = 15$, while the Meylan method was considered by imposing close paths in the complex plane of the frequency β, centred on the positive real axis. We also checked some of the solutions obtained with the multipole expansion method with a similar implementation in *Comsol Multiphysics*; we found the same values, but we report that, in the second case, it was not always possible to find all the eigenfrequencies implementing an iterative procedure. In particular, we found that, depending on the number of eigenfrequencies searched, the FEM package could miss some low-frequency eigensolutions.

In Figure 5.13b we report the dispersion diagram for $R_1/d = 0.305318$, where we indicate with a red dot the Dirac-like point at M and $\beta d = 3.794098$. A triple root of the dispersion relation (5.26) was found in the Dirac-like point. In part (a) of Figure 5.13 the first three dispersion surfaces are shown together with dispersion curves in the neighborhood of M as a function of k_1 for $k_2 = \pi$ and $k_2 = k_1$, respectively. The Dirac-like cones are evident.

R_1	$\mathbf{k}d$	βd	RM
0.211357	$\Gamma \equiv (0, 0)$	5.835796	3
0.305318	$M \equiv (\pi, \pi)$	3.794098	3
0.489726	$M \equiv (\pi, \pi)$	5.429890	2
0.489726	$\Gamma \equiv (0, 0)$	6.435974	3

TABLE 5.1: Degeneracies of the system (6.8). Initial radius R_1, normalised position in the reciprocal space $\mathbf{k}d$, normalised frequency βd and root multiplicity RM.

Finally, in Table 5.1 we report the values of R_1, the position in the reciprocal space, the frequencies and the multiplicity of the root solving the dispersion relation (5.26). Triple roots correspond to the Dirac-like points indicated in Figure 5.3 parts (a) and (c). At the double root at $\beta d = 5.429890$, two dispersion surfaces are tangent in a local minimum for both surfaces. Again, we stress that the transformation (5.11) can be tuned in order to obtain the Dirac points.

Chapter 6

Wave propagation in curved beam structures

In this chapter, we analyse propagation of low-frequency waves along curved Euler-Bernoulli beam elements. The main attention is on the coupling between longitudinal and transverse waves. First, we characterize the dispersion properties of curved beams with uniform curvature and we obtain three different propagating regimes. We then analyze a transmission problem for a curved element joining to semi-infinite straight beams. The problem is analyzed by implementing a transfer matrix approach. Energy transmission is described as a function of the curvature κ, frequency Ω and total angle α. In particular, we find a separation between high frequency/low curvature regime, where the incident wave is practically totally transmitted, and low frequency/high curvature regime where, in addition to reflection there is a strong coupling between longitudinal and flexural waves. The dispersion properties confirm the results reported in [71], with the determination of four propagating regimes. Here, we give a complete formalism, with explicit derivations of wavenumbers solving the dispersion relation, a unified analysis of the evolution of the eigensolutions in the complex plane, showing in particular, a zero-frequency buckled mode, and the analysis of the eigensolutions, describing the coupling between the longitudinal and transverse modes.

6.1 Dynamics of a curved beam

We consider the in-plane motion of the thin, uniform, curved Euler-Bernoulli beam with constant curvature shown in Figure 6.1. The motion is constrained to the plane containing the centroid axis of the beam. The coupled equations of motion, namely the balance of linear momentum, for free vibrations in the radial and tangential directions have the form [59]

$$\begin{cases} EJ\left(\frac{1}{R}\frac{\partial^3 U}{\partial s^3} - \frac{\partial^4 W}{\partial s^4}\right) - \frac{EA}{R}\left(\frac{W}{R} + \frac{\partial U}{\partial s}\right) & = \rho A\frac{\partial^2 W}{\partial t^2}, \\ \frac{EJ}{R}\left(\frac{1}{R}\frac{\partial^2 U}{\partial s^2} - \frac{\partial^3 W}{\partial s^3}\right) + EA\left(\frac{1}{R}\frac{\partial W}{\partial s} + \frac{\partial^2 U}{\partial s^2}\right) & = \rho A\frac{\partial^2 U}{\partial t^2}. \end{cases} \tag{6.1}$$

where $U(s,t)$ is the longitudinal component of the displacement and $W(s,t)$ the transverse component, with s the embedded curvilinear coordinate along the centroid axis and t the time. The beam has centroid axis with constant radius of curvature R, density ρ, bending stiffness EJ and longitudinal stiffness EA, with E the Young's modulus of the linear elastic isotropic material, A the cross-sectional area and J the second-moment of area.

In the time-harmonic regime $U(s,t) = u(s)e^{i\omega t}$, $W(s,t) = w(s)e^{i\omega t}$, with ω the angular frequency, and the equations of motion (6.1) reduce to the following system of two coupled ordinary differential equations

$$\begin{cases} EJ\left(\frac{1}{R}\frac{d^3 u}{ds^3} - \frac{d^4 w}{ds^4}\right) - \frac{EA}{R}\left(\frac{w}{R} + \frac{du}{ds}\right) + \rho A\,\omega^2 w & = 0, \\ \frac{EJ}{R}\left(\frac{1}{R}\frac{d^2 u}{ds^2} - \frac{d^3 w}{ds^3}\right) + EA\left(\frac{1}{R}\frac{dw}{ds} + \frac{d^2 u}{ds^2}\right) + \rho A\,\omega^2 u & = 0. \end{cases} \tag{6.2}$$

Additionally, we define the rotation

$$\phi = -\frac{u}{R} + \frac{dw}{ds}. \tag{6.3}$$

and the internal actions. The axial force N, the bending moment M, and the shear force Q are expressed as

$$N = EA\left(\frac{w}{R} + \frac{du}{ds}\right), \; M = EJ\left(\frac{1}{R}\frac{du}{ds} - \frac{d^2 w}{ds^2}\right), \; Q = EJ\left(\frac{1}{R}\frac{d^2 u}{ds^2} - \frac{d^3 w}{ds^3}\right) \tag{6.4}$$

They follow the sign convention reported in Figure 6.1.

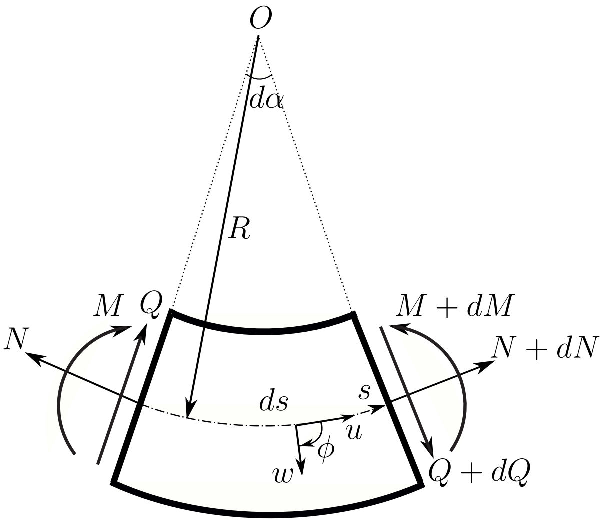

FIGURE 6.1: Sign convention and force resultants on an elementary thin curved beam element

For $R \to \infty$ the corresponding expressions for straight beam are retrieved. In particular, eqns. (6.3) and (6.4) reduce to

$$\phi = \frac{dw}{ds}, \quad N = EA\frac{du}{ds}, \quad M = -EJ\frac{d^2w}{ds^2}, \quad Q = -EJ\frac{d^3w}{ds^3}. \tag{6.5}$$

The equations of motion (6.1) are simplified into the classical second- and fourth-order uncoupled equations for longitudinal and transverse vibrations, respectively, namely

$$\begin{cases} \dfrac{d^2u}{ds^2} + k_l^2 u &= 0, \\ \dfrac{d^4w}{ds^4} - k_b^4 w &= 0, \end{cases} \tag{6.6}$$

where

$$k_l = \frac{\omega}{\omega_0}, \qquad k_b = \sqrt[4]{\frac{\rho A\,\omega^2}{EJ}}, \tag{6.7}$$

with $\omega_0 = \sqrt{E/\rho}$, are the longitudinal and flexural wavenumbers.

6.1.1 Dispersion properties

The dispersion relation is derived assuming the longitudinal and transfer displacements of the form

$$U(s,t) = C_u e^{i(ks-\omega t)}, \qquad W(s,t) = C_w e^{i(ks-\omega t)}, \tag{6.8}$$

where C_u, C_w are amplitude constants and k the wavenumber. Substituting into eqns. (6.1) gives the homogeneous system

$$\begin{bmatrix} -\dfrac{ik\,E(Jk^2+A)}{R} & -EJk^4-\dfrac{EA}{R^2}+\rho A\,\omega^2 \\ -\dfrac{EJk^2}{R^2}-EAk^2+\rho A\,\omega^2 & \dfrac{ik\,E(Jk^2+A)}{R} \end{bmatrix} \begin{pmatrix} C_u \\ C_w \end{pmatrix} = 0. \tag{6.9}$$

The corresponding dispersion relation, requirement of non-trivial solutions for C_u, C_w, is

$$k^6-\left(\frac{2}{R^2}+\frac{\rho\,\omega^2}{E}\right)k^4+\left(\frac{1}{R^4}-\frac{\rho A\,\omega^2}{EJ}-\frac{\rho\,\omega^2}{ER^2}\right)k^2+\frac{\rho^2 A\,\omega^4}{E^2 J}-\frac{\rho A\,\omega^2}{EJR^2}=0. \tag{6.10}$$

The dispersion equation gives three pairs of wavenumbers k as a function of the frequency ω. In a straight beam, they correspond to uncoupled propagating longitudinal waves ($k=\pm k_l$) and propagating and evanescent transverse waves ($k=\pm k_b$ and $k=\pm ik_b$). For a curved beam we are going two show that each wavenumber is associated to coupled longitudinal and transverse waves and different regimes, in particular at low frequencies, arise.

6.1.1.1 Normalisation

We introduce the dimensionless wavenumber κ, angular frequency Ω and curvature χ

$$\kappa=\varrho k, \qquad \Omega=\varrho\frac{\omega}{\omega_0}, \qquad \chi=\frac{\varrho}{R}, \tag{6.11}$$

where $\varrho=\sqrt{J/A}$ is the radius of gyration of the cross section. Thus, the dispersion relation eqn. (6.10) can be rewritten in non-dimensional form

$$\kappa^6-(2\chi^2+\Omega^2)\kappa^4+(\chi^4-\Omega^2-\Omega^2\chi^2)\kappa^2+\Omega^4-\Omega^2\chi^2=0. \tag{6.12}$$

6.1.1.2 Analytical solution

In order to determine the roots of the dispersion equation (6.12), we introduce the variable $z=\kappa^2$, such that the dispersion equation is

$$z^3+b_2z^2+b_1z+b_0=0, \tag{6.13}$$

where $b_2 = -(2\chi^2 + \Omega^2)$, $b_1 = \chi^4 - \Omega^2 - \Omega^2\chi^2$ and $b_0 = \Omega^4 - \Omega^2\chi^2$. Introducing the parameters

$$\begin{gathered} q = \frac{1}{3}\left(b_1 - \frac{1}{3}b_2^2\right), \qquad r = \frac{1}{6}(b_1 b_2 - 3b_0) - \frac{1}{27}b_2^3, \qquad \triangle = q^3 + r^2, \\ p_1 = \sqrt[3]{r + \sqrt{\triangle}}, \qquad p_2 = \sqrt[3]{r - \sqrt{\triangle}}, \end{gathered} \tag{6.14}$$

the 3 roots of the cubic equation (6.13) are [109]

$$\begin{aligned} z_1 &= p_1 + p_2 - \frac{b_2}{3}, \\ z_2 &= -\frac{1}{2}(p_1 + p_2) - \frac{b_2}{3} + \frac{i\sqrt{3}}{2}(p_1 - p_2), \\ z_3 &= -\frac{1}{2}(p_1 + p_2) - \frac{b_2}{3} - \frac{i\sqrt{3}}{2}(p_1 - p_2), \end{aligned} \tag{6.15}$$

and

$$\kappa_1 = -\kappa_2 = \sqrt{z_1}, \quad \kappa_3 = -\kappa_4 = \sqrt{z_2}, \quad \kappa_5 = -\kappa_6 = \sqrt{z_3}. \tag{6.16}$$

6.1.1.3 Frequency regimes

For non-zero curvature χ, we distinguish different regimes associated with the wavenumbers and the dispersion curves shown in Figures 6.2 and 6.3, respectively. The dispersion curves for different values of the curvature χ are reported in Figure 6.4.

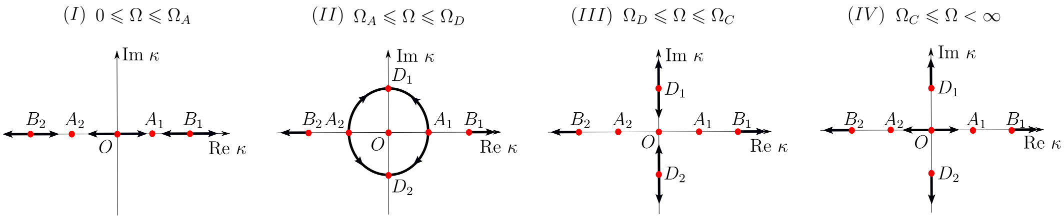
$(I)\ 0 \leqslant \Omega \leqslant \Omega_A$ $(II)\ \Omega_A \leqslant \Omega \leqslant \Omega_D$ $(III)\ \Omega_D \leqslant \Omega \leqslant \Omega_C$ $(IV)\ \Omega_C \leqslant \Omega < \infty$

FIGURE 6.2: Tracking of the path of wavenumbers κ_1, κ_2, $\cdots$, κ_6 in the complex plane as a function of the frequency Ω.

In the quasi-static regime, at $\Omega = 0$, $\Delta = 0$ (see eqn. (6.14)), $z_1 = \kappa_1 = \kappa_2 = 0$ and $z_2 = z_3 = \kappa_3^2 = \kappa_4^2 = \kappa_5^2 = \kappa_6^2 = \chi^2$, the non zero solutions corresponding to the points B_1 and B_2 in Figures 6.2 and 6.3. At such a point, a deformed configuration is possible in the static regime and in absence of any external loading, a situation analogous to the bifurcated configuration in classical Euler buckling [110].

Regime (I). In the low frequency $0 < \Omega < \Omega_A$, $\triangle < 0$, the roots $z_1 > z_2 > z_3 > 0$ are all real, distinct and positive, so that there are three couple of real solution for the wavenumbers κ corresponding to propagating waves. This is a remarkable difference with respect to the case of straight beams, where only two propagating waves are present associated with longitudinal and flexural vibrations. Note that the wavenumbers $\kappa_3 = -\kappa_4 = \sqrt{z_2}$ are associated with a negative group velocity.

When $\Omega = \Omega_A$, $\triangle = 0$ and $z_2 = z_3 > 0$. This corresponds to the points A_1 and A_2 in Figure 6.2 and to A_1, A_2, A_3 and A_4 in Figure 6.3. These points are associated with standing waves and zero group velocity.

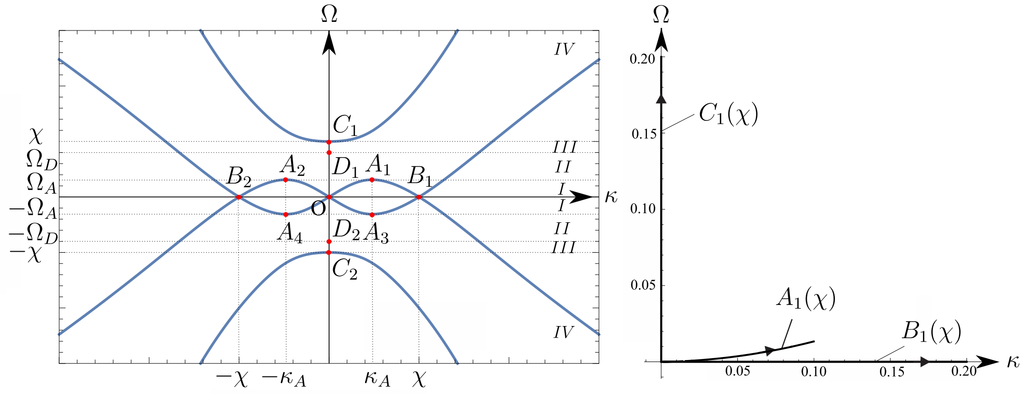

FIGURE 6.3: Dispersion diagram for the curved beam. The wavenumbers in the frequency regimes (I), (II), (III) and (IV) are reported in Figure 6.2. On the right the evolution of the positions of the critical points A_1, B_1 and C_1 in the (κ, Ω)-space, as a function of the curvature χ.

Regimes (II) and (III). In the frequency regime $\Omega_A < \Omega < \Omega_D$, $\triangle > 0$ and the roots z_2 and z_3 are complex conjugate, while z_1 remains real and positive. In this regime there is only a single couple of propagating waves associated with $\kappa_1 = -\kappa_2 = \sqrt{z_1}$, while evanescent oscillating waves correspond to the complex wavenumbers $\kappa_3 = -\kappa_4$ and $\kappa_5 = -\kappa_6$. The two roots z_2 and z_3 coalesce into a double real negative root at $\Omega = \Omega_D$, where $\triangle = 0$. In the interval $\Omega_D < \Omega < \Omega_C = \chi$, $\triangle < 0$ and the real roots are $z_2 < z_3 < 0 < z_1$. Again, there is a single couple of propagating waves associated with wavenumbers $\kappa_1 = -\kappa_2 = \sqrt{z_1}$, while evanescent waves correspond to the imaginary wavenumbers $\kappa_3 = -\kappa_4 = i\sqrt{-z_2}$ and $\kappa_5 = -\kappa_6 = i\sqrt{-z_3}$.

At $\Omega = \Omega_c = \chi$, κ_5 and κ_6 coalesce at $z_3 = \kappa_5 = \kappa_6 = 0$. Again, a standing wave can be excited at this frequency.

Regime (IV). In the high frequency regimes $\Omega > \Omega_C = \chi$, $\triangle < 0$ and real roots are $z_2 < 0 < z_3 < z_1$. As for the case of straight beam, there are two couples of propagating waves, associated here with $\kappa_1 = -\kappa_2 = \sqrt{z_1}$ and $\kappa_5 = -\kappa_6 = \sqrt{z_3}$. At large frequency $\Omega \gg 1$, $\kappa_1 \sim \Omega$ and $\kappa_5 \sim \sqrt{\Omega}$, equal to longitudinal and flexural wavenumbers for $\chi = 0$.

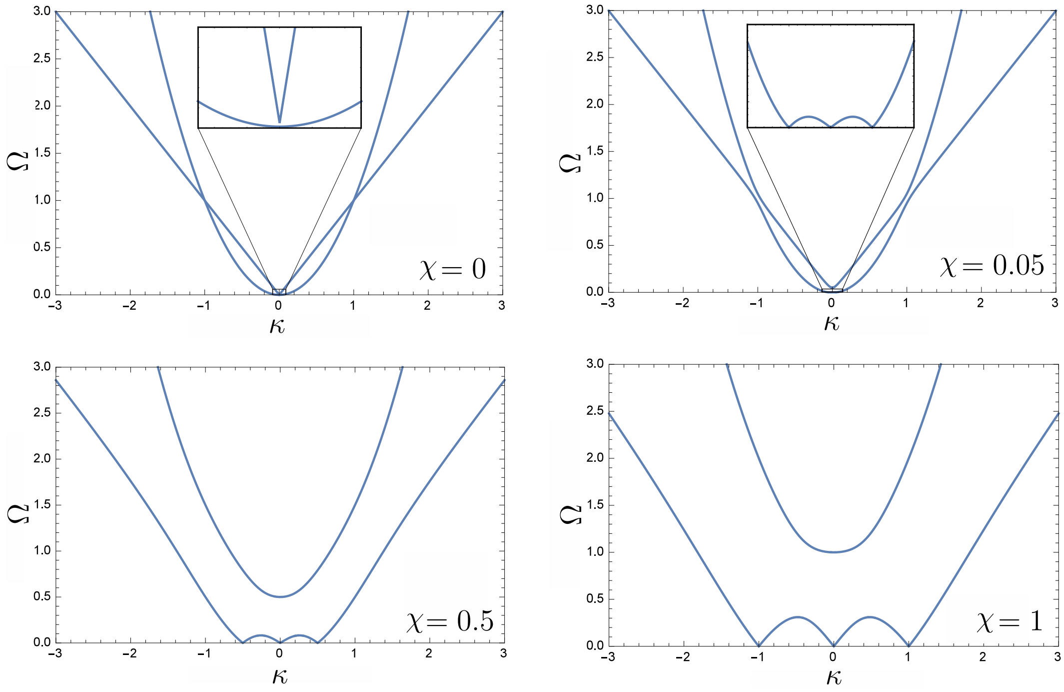

FIGURE 6.4: Dispersion curves for different values of curvature $\chi = 0$, 0.05, 0.5, 1.

For straight beams the dimensionless characteristic equation can be obtained by letting $R \to \infty$:

$$(\kappa^2 - \Omega^2)(\kappa^2 - \Omega)(\kappa^2 + \Omega^2) = 0. \tag{6.17}$$

The six roots are

$$\kappa_1 = -\kappa_2 = \Omega = \kappa_l, \quad \kappa_3 = -\kappa_4 = \sqrt{\Omega} = \kappa_b, \quad \kappa_5 = -\kappa_6 = i\sqrt{\Omega} = i\kappa_b \ , \tag{6.18}$$

and normalized wavenumber κ_l corresponds to extensional waves and κ_b to flexural waves.

6.1.2 Propagating modes

The effect of the curvature χ on the dispersion properties is reported in Figure 6.4. For $\chi = 0$, the well-known decoupled linear and parabolic curves for longitudinal and flexural waves, respectively, are present. The curvature introduce a coupling, which is particularly evident at low frequency Ω. The two curves separate at the intersection points $\kappa = \pm 1$, $\Omega = 1$.

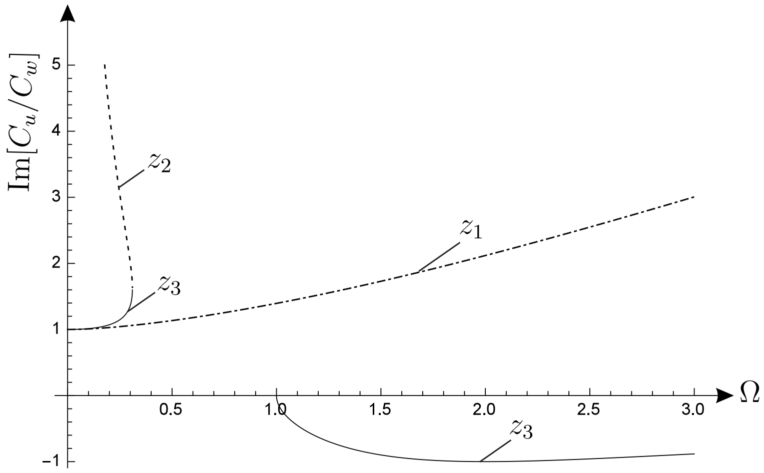

FIGURE 6.5: Ratio between the amplitude of longitudinal and flexural waves C_u/C_w as a function of the frequency Ω. Values are given for curvature $\chi = 1$.

In order to describe the coupling between longitudinal and flexural waves, we focus on the eigensolutions of the system (6.9). First, restricting the analysis to the region $\kappa \geq 0$ and $\Omega \geq 0$ of the dispersion curve of Figure 6.3, we note that the branches A_1B_1 and the one containing C_1 are associated with the root z_3, the branch $0A_1$ with z_2 and the branch departing from B_1 to z_1.

The ratio C_u/C_w between the amplitude of longitudinal and transverse displacements is given in Figure 6.5. Such a ratio is always purely imaginary in the propagating regimes, indicating a $\pi/2$ shift, such that the nodal points for one polarization correspond to the maxima and minima for the other. Around $\Omega = 0$, the branch $0A_1$ is associated with dominant longitudinal waves, the ratio $\mathrm{Im}[C_u/C_w] \sim 1/\Omega$ as $\Omega \to 0$ for the root z_2. The other two propagating modes are fully coupled in the low-frequency regime. In particular, at the point B_1 in Figures 6.2 and 6.3, where $(\kappa, \Omega) = (\chi, 0)$, $C_u = -i\,C_w = -iC$, with C a generic small constant ($C/R \ll 1$ in the linear regime). In this case, the longitudinal displacement $U(s,t) = -i\,Ce^{is/R}$ is a rigid rotation, and the transverse radial displacement $W(s,t) = Ce^{is/R}$ is also uniform.

In the point C_1 there is a pure transverse mode, which is standing mode. At higher frequencies the modes are coupled, but $\mathrm{Im}[C_u/C_w] \sim \Omega$ as $\Omega \to \infty$ for the root z_1 and $\mathrm{Im}[C_u/C_w] \sim 1/\Omega^3$ as $\Omega \to \infty$ for the root z_3, so that the modes tend to decoupled in pure longitudinal and flexural one at increasing frequency

Ω. Such a behaviour can be understood on physical ground, since modes with short wavelengths introduce a separation of length scale between wavelength and curvature of the beam.

6.1.3 Transmission problem

Here we consider a time-harmonic incident wave propagating in the straight beam in the domain $s < s_0$ and impinging the curved domain at $s = s_0$ (Figure 6.6). We analyze the transmission in the second straight beam in the domain $s > s_0 + \alpha R = s_1$. Returning to the system (6.2), the incident wave can be either longitudinal $U_i e^{ik_l s}$ or transverse $W_i e^{ik_b s}$ (see 6.7).

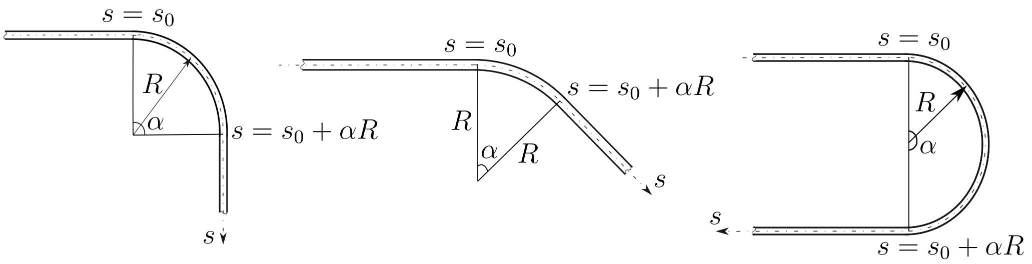

FIGURE 6.6: Transmission problem. A curved beam connect two seminfinite straight beams. The curved beam has curvature $\chi = \varrho/R$, and total angle α.

We assume that tangential/longitudinal displacements have the form

$$u(s) = \begin{cases} U_i e^{ik_l(s-s_0)} + R_1 e^{-ik_l(s-s_0)}, & \text{if } s \leq s_0, \\ C_1 e^{ik_1 s} + a_2 C_2 e^{ik_2 s} + a_3 C_3 e^{ik_3 s} + C_4 e^{ik_4 s} + a_5 C_5 e^{ik_5 s} + a_6 C_6 e^{ik_6 s}, & \text{if } s_0 \leq s \leq s_1, \\ T_1 e^{ik_l(s-s_1)}, & \text{if } s \geq s_1, \end{cases} \tag{6.19}$$

and radial/transverse displacements are

$$w(s) = \begin{cases} W_i e^{ik_b(s-s_0)} + R_2 e^{-ik_b(s-s_0)} + R_3 e^{k_b(s-s_0)}, & \text{if } s \leq s_0, \\ a_1^{-1} C_1 e^{ik_1 s} + C_2 e^{ik_2 s} + C_3 e^{ik_3 s} + a_4^{-1} C_4 e^{ik_4 s} + C_5 e^{ik_5 s} + C_6 e^{ik_6 s}, & \text{if } s_0 \leq s \leq s_1 \\ T_2 e^{ik_b(s-s_1)} + T_3 e^{-k_b(s-s_1)}, & \text{if } s \geq s_1. \end{cases} \tag{6.20}$$

where R_1 and R_2 are the reflection amplitudes for propagating waves and R_3 the reflection amplitude for the evanescent one, while T_1, T_2 are the transmission amplitudes for propagating waves and T_3 the transmission amplitude for the evanescent one. The eigenfuction parameters a_j $(j = 1, 2, \cdots, 6)$ describe the coupling between radial and tangential displacement; they have the form

$$a_j = i\frac{\kappa_j^4 + \chi^2 - \Omega^2}{\chi\kappa_j(\kappa_j^2+1)} = i\frac{\chi\kappa_j(\kappa_j^2+1)}{\kappa_j^2(\chi^2+1)-\Omega^2}. \tag{6.21}$$

In addition k_l and k_b are given in (6.7), while $k_i = \kappa_i/\varrho$ $(i = 1, \cdots, 6)$, with κ_i given in (6.16).

6.2 Transfer matrix

We define the Transfer matrix linking the fields at $s = s_1$ to the fields at $s = s_0$. We impose continuity of the kinematic fields u, w, ϕ and static fields N, M, Q at the interfaces between straight and curved regions, $s = s_0$ and $s = s_1$. We collect the kinematic and static fields in the six-dimensional vector $\mathbf{u} = \begin{bmatrix} u & w & \phi & N & M & Q \end{bmatrix}^T$; thus, for the curved beam, we can set

$$\mathbf{u}(s_0^+) = \mathbf{M}(s_0^+)\mathbf{C}, \qquad \mathbf{u}(s_1^-) = \mathbf{M}(s_1^-)\mathbf{C} = \mathbf{M}(s_1^-)[\mathbf{M}(s_0^+)]^{-1}\mathbf{u}(s_0^+) \tag{6.22}$$

where $\mathbf{C} = \begin{bmatrix} C_1 & C_2 & C_3 & C_4 & C_5 & C_6 \end{bmatrix}^T$ collect the unknown coefficients of the curved beam, see eqns. (6.19) and (6.20). After imposing the following continuity conditions at the interfaces

$$\mathbf{u}(s_0^-) = \mathbf{u}(s_0^+) = \mathbf{u}(s_0) \qquad \mathbf{u}(s_1^-) = \mathbf{u}(s_1^+) = \mathbf{u}(s_1); \tag{6.23}$$

we obtain the relation

$$\mathbf{u}(s_1) = \mathbf{T}\mathbf{u}(s_0), \tag{6.24}$$

which defines the Transfer matrix, i.e.,

$$\mathbf{T} = \mathbf{M}(s_1)[\mathbf{M}(s_0)]^{-1}. \tag{6.25}$$

The characteristic equation for the Transfer matrix is

$$\det[\mathbf{T} - \lambda\mathbf{I}] = \lambda^6 - I_1\lambda^5 + I_2\lambda^4 - I_3\lambda^3 + I_4\lambda^2 - I_5\lambda + I_6 = 0 \tag{6.26}$$

where **I** is the identity matrix. Due to the symplectic nature of **T** we have the following relations (and definitions) for the invariants

$$\begin{aligned}
I_1 &= I_5 = \mathrm{Tr}(\mathbf{T}) \\
I_2 &= I_4 = \tfrac{1}{2}\left[\mathrm{Tr}^2(\mathbf{T}) - \mathrm{Tr}(\mathbf{T}^2)\right] \\
I_3 &= \tfrac{1}{6}\left[\mathrm{Tr}^3(\mathbf{T}) - 3\,\mathrm{Tr}(\mathbf{T}^2)\,\mathrm{Tr}(\mathbf{T}) + 2\,\mathrm{Tr}(\mathbf{T}^3)\right] \\
I_6 &= \det(\mathbf{T}) = 1
\end{aligned} \tag{6.27}$$

The solutions λ of the characteristic equation (eigenvalues) satisfy the conditions

$$\lambda_i \lambda_{i+1} = 1, \qquad (i = 1, 3, 5), \tag{6.28}$$

since they are associated to three couples of waves, each of the same nature, which travel in the opposite direction.

General form of the *Transfer matrix* for a curved beam is too large to be reported here, for the sake of illustration we show the case when $R \to \infty$ and the matrix **T** is simplified to a matrix with two diagonal blocks corresponding to the *Transfer matrices* for straight beam and rod

$$\mathbf{T} = \begin{bmatrix} \mathbf{T}_1 & \mathbf{0} \\ \mathbf{0} & \mathbf{T}_2 \end{bmatrix}, \tag{6.29}$$

where $\mathbf{T}_1$ is the *Transfer matrix* of a straight rod [75], i.e.,

$$\mathbf{T}_1 = \begin{bmatrix} \cos k_l l & -\frac{1}{EAk_l}\sin k_l l \\ EAk_l \sin k_l l & \cos k_l l \end{bmatrix} \tag{6.30}$$

and $\mathbf{T}_2$ is the *Transfer matrix* of a straight beam, i.e.,

$$\mathbf{T}_2 = \begin{bmatrix}
\frac{\cos(k_b l)+\cosh(k_b l)}{2} & \frac{\sin(k_b l)+\sinh(k_b l)}{2k_b} & \frac{\cos(k_b l)-\cosh(k_b l)}{2k_b^2 EJ} & \frac{\sin(k_b l)-\sinh(k_b l)}{2k_b^3 EJ} \\
\frac{k_b[-\sin(k_b l)+\sinh(k_b l)]}{2} & \frac{\cos(k_b l)+\cosh(k_b l)}{2} & \frac{-[\sin(k_b l)+\sinh(k_b l)]}{2k_b EJ} & \frac{\cos(k_b l)-\cosh(k_b l)}{2k_b^2 EJ} \\
\frac{k_b^2 EJ[\cos(k_b l)-\cosh(k_b l)]}{2} & \frac{k_b EJ[\sin(k_b l)-\sinh(k_b l)]}{2} & \frac{\cos(k_b l)+\cosh(k_b l)}{2} & \frac{\sin(k_b l)+\sinh(k_b l)}{2k_b} \\
\frac{-k_b^3 EJ[\sin(k_b l)+\sinh(k_b l)]}{2} & \frac{k_b^2 EJ[\cos(k_b l)-\cosh(k_b l)]}{2} & \frac{k_b[-\sin(k_b l)+\sinh(k_b l)]}{2} & \frac{\cos(k_b l)+\cosh(k_b l)}{2}
\end{bmatrix}, \tag{6.31}$$

with $l = \Delta s$ the length of the interface layer.

6.3 Power flow

An incident extensional or flexural wave with unit amplitude, propagating in the positive s–direction in the region $s < s_0$, is partially reflected (in the region $s < s_0$) and partially transmitted (in the region $s > s_1$) by the curved beam. A longitudinal (or flexural) wave may induce longitudinal and flexural reflected and transmitted waves.

We computed the reflected and transmitted power flow averaged on a period $T = 2\pi/\omega$. In order to discriminate between flexural and longitudinal components and study the coupling between different type of waves we considered different contribution to the power. For the extensional component the time averaged power transmission is

$$\langle P_e \rangle = -\frac{1}{T}\int_0^T N\dot{u}dt, \tag{6.32}$$

which, following [60] can be also expressed in the simplified form

$$\langle P_e \rangle = -\frac{1}{2}N\dot{u}^*, \tag{6.33}$$

where the superscript '*' indicates the complex conjugate and we return back to the not-normalized formulation.

Similarly, power transmission due to flexural wave, expressed in term of fluxes of bending moment and shear force is

$$\langle P_b \rangle = \frac{1}{2}M\dot{\phi}^*, \qquad \langle P_s \rangle = -\frac{1}{2}Q\dot{w}^*, \tag{6.34}$$

where the different signs are associated to the conventions shown in Figure 6.1. Thus, the total time-averaged reflected or transmitted power flow is

$$\langle P_t \rangle = \langle P_e \rangle + \langle P_b \rangle + \langle P_s \rangle. \tag{6.35}$$

The explicit expression for the different contributions are

$$\begin{aligned} \langle P_e \rangle_i &= \frac{1}{2}EA\,k_l\omega C_A^2 \\ \langle P_b \rangle_i &= \frac{1}{2}EJ\,k_b^3\omega C_B^2 + \frac{1}{2R^2}EJ\,k_l\omega C_A^2 \\ \langle P_s \rangle_i &= \frac{1}{2}EJ\,k_b^3\omega C_B^2 \end{aligned} \tag{6.36}$$

where $i = T$, $C_A = T_1$ and $C_B = T_2$ for the transmission, $i = R$, $C_A = R_1$ and $C_B = R_2$ for the reflection and $i = I$, $C_A = U_i = 1$ and $C_B = W_i = 1$ for the longitudinal and transverse incident waves, respectively.

We define relative time-averaged transmitted and reflected power flows by normalizing transmitted and reflected coefficiens by means of the incident one. Relative power transmission coefficients are

$$\begin{aligned} T_{ee} &= \left| \frac{\langle P_e \rangle_T}{\langle P_e \rangle_I} \right| = T_1^2, \\ T_{ff} &= \left| \frac{\langle P_b \rangle_T + \langle P_s \rangle_T}{\langle P_f \rangle_I} \right| = T_2^2, \\ T_{fe} &= \left| \frac{\langle P_b \rangle_T + \langle P_s \rangle_T}{\langle P_e \rangle_I} \right| = 2\sqrt{\Omega}\, T_2^2, \\ T_{ef} &= \left| \frac{\langle P_e \rangle_T}{\langle P_f \rangle_I} \right| = \frac{T_1^2}{2\sqrt{\Omega}}. \end{aligned} \tag{6.37}$$

Relative time-averaged power reflection coefficients are

$$\begin{aligned} R_{ee} &= \left| \frac{\langle P_e \rangle_R}{\langle P_e \rangle_I} \right| = R_1^2, \\ R_{ff} &= \left| \frac{\langle P_b \rangle_R + \langle P_s \rangle_R}{\langle P_f \rangle_I} \right| = R_2^2, \\ R_{fe} &= \left| \frac{\langle P_b \rangle_R + \langle P_s \rangle_R}{\langle P_e \rangle_I} \right| = 2\sqrt{\Omega}\, R_2^2, \\ R_{ef} &= \left| \frac{\langle P_e \rangle_R}{\langle P_f \rangle_I} \right| = \frac{R_1^2}{2\sqrt{\Omega}}. \end{aligned} \tag{6.38}$$

In the coefficients definitions (6.37) and (6.38) the double subscript indicate the normalized and the incident fields, respectively. It is easy to verify the energy conservation

$$\begin{aligned} T_{ee} + T_{fe} + R_{ee} + R_{fe} &= 1, \\ T_{ff} + T_{ef} + R_{ff} + R_{ef} &= 1. \end{aligned} \tag{6.39}$$

for both flexural and extensional incident waves.

6.4 Reflection, transmission and coupling

The reflection and transmission coefficients in eqns. (6.37) and (6.38) depend on the frequency Ω, curvature χ and total angle α.

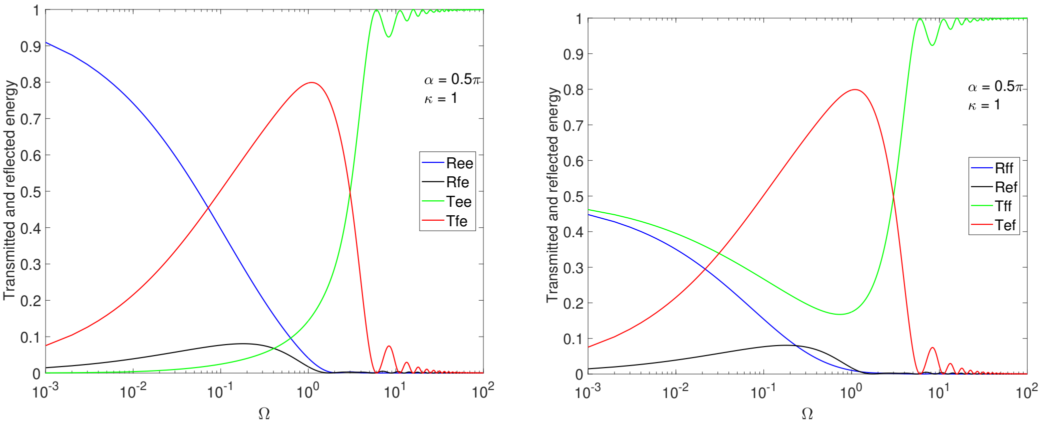

(a) (b)

FIGURE 6.7: Transmitted and reflected power flow as a function of the frequency Ω. Values are given for a total angle $\alpha = \pi/2$ and curvature $\chi = 1$. (a) Longitudinal incident wave (b) Flexural incident wave.

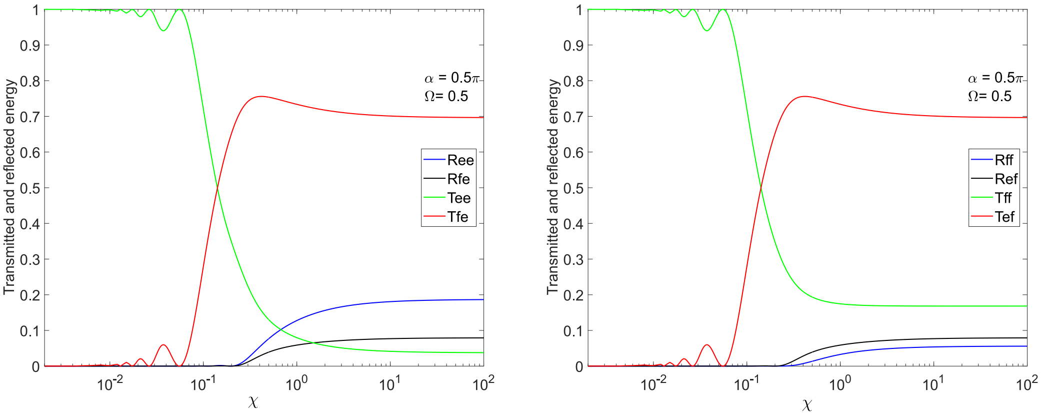

(a) (b)

FIGURE 6.8: Transmitted and reflected power flow as a function of the curvature χ. Values are given for a total angle $\alpha = \pi/2$ and frequency $\Omega = 0.5$. (a) Longitudinal incident wave (b) Flexural incident wave.

The reflected and transmitted energy as a function of the frequency is shown in Figure 6.7. In the low frequency regime it is present a strong coupling between longitudinal and transverse waves. For a longitudinal incident wave at low frequency the transmitted power is predominantly of flexural type. As opposite, in the high frequency regime the incident wave is practically totally transmitted.

A similar behavior is observed as a function of the curvature, shown in Figure 6.8. In this case at low curvature the incident wave is practically totally transmitted, while at high curvature a strong coupling is shown with high reflection and wave transformation. In both cases, in the high curvature regime, the incident wave is mainly transformed into the other one in the transmission domain.

Chapter 7

Conclusions

The work has been focused on wave propagation in metamaterials and complex structures, and this allows us to apply such knowledge to design devices.

A periodic geometric transformation technique has been applied to a phononic elastic crystal and the analytical derivation of the transformed equations for the new periodic system has been fully described. The comparison of dispersion properties between untransformed and transformed configurations shows the correspondence in terms of both frequency and wavenumber vector $\mathbf{k}$.

Since the model is periodic, the cloaking effect can be extended to any number of inclusions; in addition, the design of high reflective elastic systems has been proposed. Such results have been demonstrated for a transmission problem and are valid for both normal and oblique incidence. They have been validated quantitatively by showing the dependance of transmitted power flux on the frequency.Overlapping transformation can be implemented with the purpose to increase the transmission in presence of large voids, while unfolding transformations give rise to localised resonances that, also at zero frequency, can harvest energy around the interfaces between untransformed and transformed domain. In the proposed periodic settings, several interfaces may localise energy, depending on the applied load. Nevertheless, the design requires an elastic system with local negative mechanical properties.

Low-frequency homogenisation has shown the variety of elastic behaviors that can be attained in long wavelength regime, with the possibility to tune the effective phase and group velocities.

This approach works equally well in the case of waveguides with multiple anisotropic and inhomogeneous shells, where reflectance can be strongly enhanced and it is easy to obtain multiple defect modes in an infinite waveguide with voids of negligible size.

A final application proposes an implementation of the transformation technique in order to design a periodic system with a predetermined micro-geometry capable to give Dirac points. In such a case the semi-analytical multipole expansion is a useful technique for the construction of recursive algorithms. The results are scale-independent within the range of validity of the linear elastic theory and they can be applied to elastic systems at different scales including large structures typical of Civil and Structural Engineering or small MEMS systems.

The dynamics of curved beams involving longitudinal and transverse flexural waves has been analysed in Chapter 6. Dispersion properties indicate the existence of 4 propagating regimes, showing in particular, a zero-frequency buckled mode, and the analysis of the eigensolutions, describing the coupling between the longitudinal and transverse modes. The analysis of the transmission problem reveals a transition between a low frequency/high curvature regime and a high frequency/low curvature one. Clearly, the applicability of the results is limited to the frequency range where the Euler-Bernoulli model is applicable. The results of the present work have a range of applicability that span from large engineering structures like bridges to micromechanical components as MEMS.

The main research objective of the Thesis was focused on out of plane shear waves in periodic structures that are governed by the Helmholtz equation. The result will be expanded to the problem of vector elasticity and flexural waves in thin plates in the near future. In this respect both the multipole expansion technique and numerical analyses will be applied. The analysis of wave propagation in curve flexural beams was performed during the 8 month visit at LAUM - Laboratoire d'Acoustique de l'Université du Maine. It will be used to build metasurfaces in flexural systems.

Appendix A. Perfectly Matched Layers (PML)

The concept of a Perfectly Matched Layer (PML) is an analytic continuations of the wave equation into complex coordinates, replacing propagating waves with damped waves. The idea also consists in imposing the behavior of the solution in the PML domain, and then extract the corresponding equations and interface conditions. Thereby, it is possible to create a non-reflective PML. Thus, a key property of PML is that it is designed in such a way that waves incident on PML from a non-PML medium are not reflected at the interface. This property allows PML to strongly absorb outgoing waves from the interior of a computational region without reflecting them back into the interior.

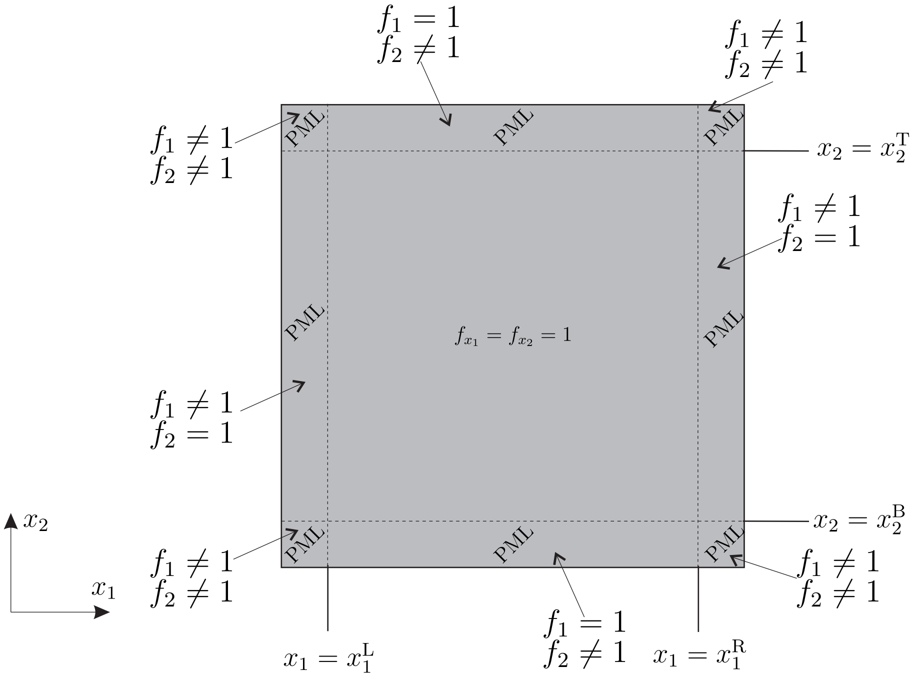

FIGURE A.1: 2D geometry of PML domains and defination of complex stretching gradients.

We introduce the complex coordinate transformation in the PML domains

$$\frac{\partial}{\partial x_i} \to \frac{1}{f_i}\frac{\partial}{\partial x_i}, \quad i = 1, 2. \tag{A.1}$$

Then, using the above transformation, the two-dimensional Helmholtz equation is transformed into

$$\left(\frac{1}{f_1}\frac{\partial}{\partial x_1}\left(\frac{1}{f_1}\frac{\partial}{\partial x_1}\right) + \frac{1}{f_2}\frac{\partial}{\partial x_2}\left(\frac{1}{f_2}\frac{\partial}{\partial x_2}\right) + \beta^2\right)u(x_1, x_2) = 0, \tag{A.2}$$

The f_1, f_2 stretching gradients are determined by the position of the PML domain as shown in Figure A.1.

For the PML domains damping in the x_1 direction

$$f_1 = \begin{cases} 1 + \dfrac{i}{\beta \mid {x_1}^{\mathrm{R(L)}} - x_1 \mid}, & \text{in the lateral PML domains,} \\ 1, & \text{otherwise} \end{cases} \tag{A.3}$$

and in the x_2 direction

$$f_2 = \begin{cases} 1 + \dfrac{i}{\beta \mid {x_2}^{\mathrm{T(B)}} - x_2 \mid}, & \text{in the top/bottom PML domains,} \\ 1, & \text{otherwise} \end{cases} \tag{A.4}$$

for domains where there is no absorption in the x_1 or x_2 directions, respectively, $f_1 = f_2 = 1$.

Appendix B. Green's functions

Here, we describe the method for obtaining the Green functions for Helmholtz and Laplace/quasistatic Helmholtz equations.

Dynamics

Assuming that the source point is at $\mathbf{x}_0$, the Green's function G for the Helmholtz equation in $\mathbb{R}^2$ satisfies the following inhomogeneous equation

$$\nabla^2 G(\mathbf{x}-\mathbf{x}_0)+\beta^2 G(\mathbf{x}-\mathbf{x}_0)=\delta(\mathbf{x}-\mathbf{x}_0) \tag{B.1}$$

where δ is the Dirac delta function.

The general solution the homogeneous Helmholtz equation in polar cylindrical coordinates is defined as

$$G(r)=C_1 J_0(\beta r)+C_2 H_0^{(1)}(\beta r) \tag{B.2}$$

where $H_0^{(1)}$, J_0 are the first kind of Hankel and Bessel functions, respectively.

Considering the flux and measuring the flow moving across a small enclosed circlular domain

$$-\lim_{\epsilon\to 0}\int_{s_\epsilon} \nabla\cdot G\mid_{r\to\epsilon} ds=-1 \tag{B.3}$$

where s is a circle with a small radius ϵ centered at $\mathbf{x}_0$ and area $ds=\epsilon d\epsilon d\theta$. Then, by applying the Green's theorem

$$\begin{aligned}
-\lim_{\epsilon\to 0}\oint_{c_\epsilon}\left[\frac{\partial G}{\partial r}\right]_{r\to\epsilon} ds &= -\lim_{\epsilon\to 0}\oint_0^{2\pi}\epsilon\frac{\partial G}{\partial r}d\theta\\
&= -\lim_{\epsilon\to 0}\oint_0^{2\pi}\epsilon\left[\frac{\partial}{\partial r}\Big(C_1 J_0(\beta r)+C_2 H_0^{(1)}(\beta r)\Big)\right]_{r\to\epsilon} d\theta\\
&= \lim_{\epsilon\to 0} 2\pi\beta\epsilon\left[(C_1+C_2)J_1(\beta r)+iC_2 Y_1(\beta r)\right]_{r\to\epsilon}\\
&= \lim_{\epsilon\to 0} 2\pi\beta\epsilon\left[iC_2\left(-\frac{2}{\pi\beta\epsilon}\right)\right]\\
&= -4iC_2=-1
\end{aligned} \tag{B.4}$$

where the Bessel function of the first kind has negligible value at $r\to\epsilon$. Then, $C_2=-i/4$ and C_1 is chosen as zero.

Green's function for an arbitrary singular point $\mathbf{x}_0$ is given by

$$G(r) = -\frac{i}{4} H_0^{(1)}(\beta r) \tag{B.5}$$

where $r = \mid \mathbf{x} - \mathbf{x}_0 \mid$ and the sign of the function depends on the direction of applied force.

Figure B.1 shows the real part of the displacement field obtained with the Green's function formulation. The point source position is at the origin of coordinate system.

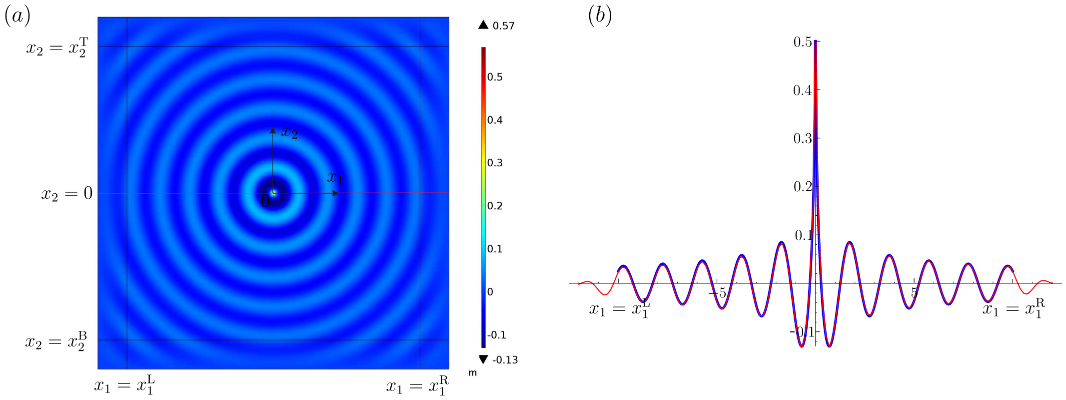

FIGURE B.1: (a) The displacement field computed in Comsol. (b) Comparison of analytical (blue) and numerical (red) solutions along the line $x_2 = 0$ in (a).

Quasistatics

Green's function for quasistatic Helmholtz equation

$$\nabla^2 G(\mathbf{x} - \mathbf{x}_0) = \delta(\mathbf{x} - \mathbf{x}_0) \tag{B.6}$$

In the same way, to find the Green's function, we can consider the flux through a circle, as considered for the equations of dynamics or considering the quasistatic equation in cylindrical coordinate system

$$\frac{1}{r}\frac{\partial}{\partial r}\left(\frac{\partial G}{\partial r}\right) = \frac{\delta}{2\pi r} \tag{B.7}$$

and multiplying both sides by r and integrating from 0 to r, we obtain

$$G(r) = \frac{1}{2\pi} \ln r, \tag{B.8}$$

where $r = \mid \mathbf{x} - \mathbf{x}_0 \mid$.

Appendix C. Computation of the power flow in *COMSOL Multiphysics 5.3* and its correspondence with the power flow in elasticity

We compute the time-averaged energy flux in an electromagnetism physics *COMSOL Multiphysics 5.3*, where the Poynting vector represents the directional energy flux, the energy transfer per unit area per unit time, of an electromagnetic field.

The Poynting vector is defined as

$$\mathbf{P} = \mathbf{E} \times \mathbf{H} = \begin{pmatrix} E_{x_2} H_{x_3} - E_{x_3} H_{x_2} \\ E_{x_3} H_{x_1} - E_{x_1} H_{x_3} \\ E_{x_1} H_{x_2} - E_{x_2} H_{x_1} \end{pmatrix}, \tag{C.1}$$

where $\mathbf{E} = (E_{x_1}\, E_{x_2}\, E_{x_3})^T$ is the electric field vector, $\mathbf{H} = (H_{x_1}\, H_{x_2}\, H_{x_3})^T$ is the magnetic field's auxiliary field vector. By using the constitutive relations, above equation can be written as

$$\mathbf{P} = \frac{1}{\mu_0} \mathbf{E} \times \mathbf{B}, \tag{C.2}$$

where μ_0 is the vacuum permeability, $\mathbf{B}$ is the magnetic field and $\mathbf{H} = 1/\mu\, \mathbf{B}$, μ is the magnetic permeability of the medium in which the field exists. Then, time-averaged Poynting vector is defined as

$$\langle \mathbf{P} \rangle = \langle \mathbf{E} \times \mathbf{H} \rangle = \frac{1}{T} \int_0^T \mathbf{E} \times \mathbf{H}\, dt = \frac{1}{2} Re[\mathbf{E} \times \mathbf{H}^*], \tag{C.3}$$

where * is the sign of complex conjugate, $Re[\;]$ is the real part of function. Then,

$$\langle \mathbf{P} \rangle = \frac{1}{2} \begin{pmatrix} Re[E_{x_2} H^*_{x_3} - E_{x_3} H^*_{x_2}] \\ Re[E_{x_3} H^*_{x_1} - E_{x_1} H^*_{x_3}] \\ Re[E_{x_1} H^*_{x_2} - E_{x_2} H^*_{x_1}] \end{pmatrix} \tag{C.4}$$

and for anisotropic material

$$\mathbf{H} = \frac{1}{\mu} \mathbf{B} = \tilde{\mu}\, \mathbf{B}, \tag{C.5}$$

where $\tilde{\mu} = \mu^{-1}$ and the expanded form is

$$\begin{aligned} H_{x_1} &= \tilde{\mu}_{x_1x_1} B_{x_1} + \tilde{\mu}_{x_1x_2} B_{x_2}, \\ H_{x_2} &= \tilde{\mu}_{x_2x_1} B_{x_1} + \tilde{\mu}_{x_2x_2} B_{x_2}, \\ H_{x_3} &= \tilde{\mu}_{x_3x_1} B_{x_1} + \tilde{\mu}_{x_3x_2} B_{x_2} \end{aligned} \tag{C.6}$$

and here the elements of the inverse matrix $\tilde{\mu}$ in terms of elements of matrix μ is defined as

$$\tilde{\mu} = \frac{1}{\mid \mu \mid} \begin{pmatrix} \begin{vmatrix} \mu_{x_2x_2} & \mu_{x_2x_3} \\ \mu_{x_3x_2} & \mu_{x_3x_3} \end{vmatrix} & \begin{vmatrix} \mu_{x_1x_3} & \mu_{x_1x_2} \\ \mu_{x_3x_3} & \mu_{x_3x_2} \end{vmatrix} & \begin{vmatrix} \mu_{x_1x_2} & \mu_{x_1x_3} \\ \mu_{x_2x_2} & \mu_{x_2x_3} \end{vmatrix} \\ \\ \begin{vmatrix} \mu_{x_2x_2} & \mu_{x_2x_3} \\ \mu_{x_3x_2} & \mu_{x_3x_3} \end{vmatrix} & \begin{vmatrix} \mu_{x_1x_3} & \mu_{x_1x_2} \\ \mu_{x_3x_3} & \mu_{x_3x_2} \end{vmatrix} & \begin{vmatrix} \mu_{x_1x_2} & \mu_{x_1x_3} \\ \mu_{x_2x_2} & \mu_{x_2x_3} \end{vmatrix} \\ \\ \begin{vmatrix} \mu_{x_2x_2} & \mu_{x_2x_3} \\ \mu_{x_3x_2} & \mu_{x_3x_3} \end{vmatrix} & \begin{vmatrix} \mu_{x_1x_3} & \mu_{x_1x_2} \\ \mu_{x_3x_3} & \mu_{x_3x_2} \end{vmatrix} & \begin{vmatrix} \mu_{x_1x_2} & \mu_{x_1x_3} \\ \mu_{x_2x_2} & \mu_{x_2x_3} \end{vmatrix} \end{pmatrix} \tag{C.7}$$

where $\mid . \mid$ indicates the determinant of matrices

$$\begin{aligned} \mid \mu \mid = {} & \mu_{x_1x_1}\mu_{x_2x_2}\mu_{x_3x_3} + \mu_{x_1x_2}\mu_{x_2x_3}\mu_{x_3x_1} + \mu_{x_1x_3}\mu_{x_2x_1}\mu_{x_3x_2} \\ & - \mu_{x_1x_3}\mu_{x_2x_2}\mu_{x_3x_1} - \mu_{x_1x_2}\mu_{x_2x_1}\mu_{x_3x_3} - \mu_{x_1x_1}\mu_{x_2x_3}\mu_{x_3x_2}. \end{aligned} \tag{C.8}$$

For isotropic and out of plane electric field $E_{x_3} = e^{ik(\cos\theta_I x_1 + \sin\theta_I x_2) - i\omega t}$

$$\begin{aligned} \langle P_{x_1} \rangle &= -\frac{1}{2} Re[E_{x_3} H^*_{x_2}], \\ \langle P_{x_2} \rangle &= \frac{1}{2} Re[E_{x_3} H^*_{x_1}], \\ \langle P_{x_3} \rangle &= 0 \end{aligned} \tag{C.9}$$

and the components of magnetic vector field $\mathbf{B} = -i\omega^{-1} \nabla \times \mathbf{E}$ are

$$B_{x_1} = \frac{1}{i\,\omega} \frac{\partial E_{x_3}}{\partial x_2}, \quad B_{x_2} = \frac{1}{i\,\omega} \frac{\partial E_{x_3}}{\partial x_1}, \quad B_{x_3} = 0. \tag{C.10}$$

In elasticity, the time-averaged over a period $T = 2\pi/\omega$ rate of energy flux passing through a surface, with local outward normal $\mathbf{n}$, is

$$\langle \mathbf{P} \rangle = \frac{1}{2} Re[\tau_{3j} n_j \dot{u}^*], \quad j = 1, 2\,, \tag{C.11}$$

where $\tau_{3j} = \mu \partial u / \partial x_j$ are the out of plane shear stress components, $\dot{u}^*$ the complex conjugate of velocity and n_j the components of the normal to the surface. Electric field E_{x_3} corresponds to displacement field u in elasticity.

Appendix D. Comparison between multipole expansion method and finite element simulations

To determine the dispersion surfaces, we fixed the wave vector **k** and we searched for the frequency β satisfying the dispersion relation (5.26). In the multipole expansion method, we implemented the Meylan approach [82], searching for the number of roots within a closed path in the complex plane of β. The paths are centred on the positive real axis and in the analysis we have found only real values.

A comparison between the frequencies computed in *Comsol Multiphisics* and the semi-analytical multipole expansion approach is reported in Table D.1. In the computations N is the truncation number adopted for the finite system (6.8), approximating the infinite sum in (5.24), which we have taken equal to the truncation number for the sum in h_1 and h_2 in (5.23).

$\mathbf{k}d$	FEM	ME ($N=2$)	ME ($N=5$)	ME ($N=10$)
$\left(\frac{\pi}{2},0\right)$	1.356952	1.358036	1.356951	1.356952
	4.526865	4.532874	4.526868	4.526865
	6.257810	–	6.257825	6.257810
	6.559204	6.849747	6.559220	6.559201
	7.929420	7.938114	7.929743	7.929421
	8.037572	8.136470	8.037584	8.037570
$\left(\pi,\frac{\pi}{2}\right)$	2.714203	2.714191	2.714200	2.714203
	3.754604	3.773696	3.754605	3.754604
	5.127843	5.204680	5.127832	5.127841
	7.348258	7.369042	7.348285	7.348258
	7.989113	–	7.989165	7.989111
	8.804243	8.383524	8.804280	8.804240
$\left(\frac{\pi}{2},\frac{\pi}{2}\right)$	1.948120	1.948065	1.948119	1.948120
	4.337816	4.343927	4.337814	4.337816
	5.378690	5.498149	5.378691	5.378688
	7.539204	7.588725	7.539273	7.539201
	7.544650	7.854300	7.545151	7.544664
	8.435667	8.574477	8.435700	8.435666

TABLE D.1: Comparison between numerical (FEM) and multipole expansion (ME) methods. The first 6 eigenfrequencies βd have been computed at three different points in the reciprocal space. Values correspond to a transformed geometry with $R_0/d = 0.4$, $R_1/d = 0.3$, $R_2/d = 0.375$ ($\alpha_1 = 0.25$). Neumann boundary conditions are applied at $r = R_2$. In the multipole expansion method the system (5.24) and the sum in h_1 and h_2 in (5.23) have been truncated at $N = 2$, $N = 5$ and $N = 10$, respectively.

Appendix E. Finite element implementation of the transmission problem

Details on the implementation of the finite element simulation are given here. The most problematic numerical computation was the one reported in Figure 5.9d, where $R_1/d = 0.44\bar{4}$, $R_2/d = 9.88 \cdot 10^{-3}$, $R_0/d = 0.494$. Around each void of radius R_2 we built three shell domains, with external radii $2R_2$, $10R_2$ and R_0, respectively. In each domain, from the inner to the outer, we set the maximum element size s_E/d equal to $1.23 \cdot 10^{-4}$, $2.47 \cdot 10^{-3}$ and $9.88 \cdot 10^{-3}$, respectively, while in the external matrix the limiting element size is $s_E/d = 1.23 \cdot 10^{-2}$. The mesh consists of $9.2 \cdot 10^6$ linear triangular elements corresponding to $64.5 \cdot 10^6$ degrees of freedom. The computation was performed on a 2xXeon E5-2600v4 workstation with 192 GB RAM in 57 min.

Appendix F. Matrix M

After implementation of representations (6.19) for $u(s)$ and (6.20) for $w(s)$, in the domain $s_0 < s < s_1$ and relations (6.4) for ϕ, N, M and Q, the matrix $\mathbf{M}$ is defined as

$$\mathbf{M}(s) = \begin{bmatrix} e^{-ik_1 s} & a_2 e^{-ik_2 s} & a_3 e^{-ik_3 ss} & e^{-ik_4 s} & a_5 e^{-ik_5 s} & a_6 e^{-ik_6 s} \\ a_1^{-1} e^{-ik_1 s} & e^{-ik_2 s} & e^{-ik_3 s} & a_4^{-1} e^{-ik_4 s} & e^{-ik_5 s} & e^{-ik_6 s} \\ \phi_1 & \phi_2 & \phi_3 & \phi_4 & \phi_5 & \phi_6 \\ N_1 & N_2 & N_3 & N_4 & N_5 & N_6 \\ M_1 & M_2 & M_3 & M_4 & M_5 & M_6 \\ Q_1 & Q_2 & Q_3 & Q_4 & Q_5 & Q_6 \end{bmatrix} \tag{F.1}$$

where

$$\begin{aligned} \phi_1 &= -\left(\frac{1}{R} + i\frac{k_1}{a_1}\right) e^{-ik_1 s}, & \phi_2 &= -\left(\frac{1}{R}a_2 + ik_2\right) e^{-ik_2 s}, \\ \phi_3 &= -\left(\frac{1}{R}a_3 + ik_3\right) e^{-ik_3 s}, & \phi_4 &= -\left(\frac{1}{R} + i\frac{k_4}{a_4}\right) e^{-ik_4 s}, \\ \phi_5 &= -\left(\frac{1}{R}a_5 + ik_5\right) e^{-ik_5 s}, & \phi_6 &= -\left(\frac{1}{R}a_6 + ik_6\right) e^{-ik_6 s}, \\ N_1 &= \left(\frac{1}{a_1 R} - ik_1\right) e^{-ik_1 s}, & N_2 &= \left(\frac{1}{R} - ik_2 a_2\right) e^{-ik_2 s}, \\ N_3 &= \left(\frac{1}{R} - ik_3 a_3\right) e^{-ik_3 s}, & N_4 &= \left(\frac{1}{a_4 R} - ik_4\right) e^{-ik_4 s}, \\ N_5 &= \left(\frac{1}{R} - ik_5 a_5\right) e^{-ik_5 s}, & N_6 &= \left(\frac{1}{R} - ik_6 a_6\right) e^{-ik_5 s}, \\ M_1 &= \left(-\frac{i}{R} + \frac{k_1}{a_1}\right) k_1 e^{-ik_1 s}, & M_2 &= \left(-\frac{ia_2}{R} + k_2\right) k_2 e^{-ik_2 s}, \\ M_3 &= \left(-\frac{ia_3}{R} + k_3\right) k_3 e^{-ik_3 s}, & M_4 &= \left(-\frac{i}{R} + \frac{k_4}{a_4}\right) k_4 e^{-ik_4 s}, \\ M_5 &= \left(-\frac{ia_5}{R} + k_5\right) k_5 e^{-ik_5 s}, & M_6 &= \left(-\frac{ia_6}{R} + k_6\right) k_6 e^{-ik_6 s}, \\ Q_1 &= -\left(\frac{1}{R} + i\frac{k_1}{a_1}\right) k_1^2 e^{-ik_1 s}, & Q_2 &= -\left(\frac{a_2}{R} + ik_2\right) k_2^2 e^{-ik_2 s}, \\ Q_3 &= -\left(\frac{a_3}{R} + ik_3\right) k_3^2 e^{-ik_3 s}, & Q_4 &= -\left(\frac{1}{R} + i\frac{k_4}{a_4}\right) k_4^2 e^{-ik_4 s}, \\ Q_5 &= -\left(\frac{a_5}{R} + ik_5\right) k_5^2 e^{-ik_5 s}, & Q_6 &= -\left(\frac{a_6}{R} + ik_6\right) k_6^2 e^{-ik_6 s}. \end{aligned} \tag{F.2}$$

Bibliography

[1] N. Engheta and R. Ziolkowski, *Metamaterials: Physics and Engineering Explorations*. Wiley & Sons, 2006.

[2] A. Sarychev and V. M. Shalaev, *Electrodynamics of Metamaterials*. World Scientific, 2007.

[3] R. Craster and S. Guenneau, *Acoustic Metamaterials: Negative Refraction, Imaging, Lensing and Cloaking*. Springer Series in Materials Science, 2012.

[4] J. Pendry, D. Schurig, and D. Smith, "Controlling electromagnetic fields," *Science*, vol. 312, no. 5781, pp. 1780–1782, 2006.

[5] U. Leonhardt, "Optical conformal mapping," *Science*, vol. 312, no. 5801, pp. 1777–1780, 2006.

[6] V. Veselago, "The electrodynamics of substances with simultaneously negative values of ϵ and μ," *Soviet Physics Uspekhi*, vol. 10, no. 4, pp. 509–514, 1968.

[7] J. Pendry, "Negative refraction makes a perfect lens," *Physical Review Letters*, vol. 85, no. 18, pp. 3966–3969, 2000.

[8] A. Alù and N. Engheta, "Boosting molecular fluorescence with a plasmonic nanolauncher," *Physical Review Letters*, vol. 103, no. 4, p. 043902, 2009.

[9] M. Noginov, H. Li, Y. Barnakov, D. Dryden, G. Nataraj, G. Zhu, C. Bonner, M. Mayy, Z. Jacob, and E. Narimanov, "Controlling spontaneous emission with metamaterials," *Optics Letters*, vol. 35, no. 11, pp. 1863–1865, 2010.

[10] M. Silveirinha and N. Engheta, "Tunneling of electromagnetic energy through subwavelength channels and bends using ϵ-near-zero materials," *Physical Review Letters*, vol. 97, no. 15, p. 157403, 2006.

[11] B. Edwards, A. Alù, M. Young, M. Silveirinha, and N. Engheta, "Experimental verification of epsilon-near-zero metamaterial coupling and energy squeezing using a microwave waveguide," *Physical Review Letters*, vol. 100, no. 3, p. 033903, 2008.

[12] J. Maxwell, *On physical lines of force*. The Scientific Papers of James Clerk Maxwell ed W D Niven (Cambridge: Cambridge University Press), 1890.

[13] P. Hertz, "Die Bewegung eines Elektrons unter dem Einflusse einer stets gleich gerichteten Kraft," *Mathematische Annalen*, vol. 65, no. 1, pp. 1–86, 1907.

[14] M. Kerker, "Invisible bodies," *Journal of the Optical Society of America*, vol. 65, no. 4, pp. 376–379, 1975.

[15] E. Mansfield, "Neutral holes in plane sheet-reinforced holes which are elastically equivalent to the uncut sheet," *The Quarterly Journal of Mechanics and Applied Mathematics*, vol. 6, no. 3, pp. 370–378, 1953.

[16] Z. Hashin, "The elastic moduli of heterogeneous materials," *Journal of Applied Mechanics*, vol. 29, no. 1, pp. 143–150, 1962.

[17] J. MacKenzie, "The elastic constants of a solid containing spherical holes," *Proceedings of the Physical Society B*, vol. 63, no. 1, pp. 2–11, 1950.

[18] K. Bertoldi, D. Bigoni, and W. Drugan, "Structural interfaces in linear elasticity. Part II: Effective properties and neutrality," *Journal of the Mechanics and Physics of Solids*, vol. 55, no. 1, pp. 35–63, 2007.

[19] P. Lueg, "On the invention of active noise control," *The Journal of the Acoustical Society of America*, vol. 87, pp. 2251–2254, 1990.

[20] P. Nelson and S. Elliott, *Active control of sound*. Academic Press, 1992.

[21] F. Vasquez, G. Milton, and D. Onofrei, "Active exterior cloaking for the 2D Laplace and Helmholtz equations," *Physical Review Letters*, vol. 7, no. 103, p. 073901, 2009.

[22] F. Vasquez, G. Milton, and D. Onofrei, "Broadband exterior cloaking," *Optics Express*, vol. 7, no. 17, pp. 14800–14805, 2009.

[23] F. Vasquez, G. Milton, and D. Onofrei, "Exterior cloaking with active sources in two dimensional acoustics," *Wave Motion*, vol. 48, pp. 515–524, 2011.

[24] A. Norris, F. Amirkulova, and W. Parnell, "Source amplitudes for active exterior cloaking," *Inverse Problems*, vol. 28, p. 105002, 2012.

[25] A. Norris, F. Amirkulova, and W. Parnell, "Active elastodynamic cloaking," *Mathematics and Mechanics of Solids*, vol. 19, no. 6, pp. 603–625, 2013.

[26] J. O'Neill, O. Selsil, R. McPhedran, A. Movchan, and N. Movchan, "Active cloaking of inclusions for flexural waves in thin elastic plates," *The Quarterly Journal of Mechanics and Applied Mathematics*, vol. 68, no. 3, pp. 263–288, 2015.

[27] H. Lamb, *Hydrodynamics*, vol. Sixth Edition. Cambridge University press, 1932.

[28] N. Muskhelishvili, *Some Basic Problems of the Mathematical Theory of Elasticity*. Groningen, P.Noordhoff, Ltd, 1949.

[29] A. Greenleaf, M. Lassas, and G. Uhlmann, "On nonuniqueness for Calderón's inverse problem," *Mathematical Research Letters*, vol. 10, no. 5, pp. 685–693, 2003.

[30] A. Greenleaf, M. Lassas, and G. Uhlmann, "Anisotropic conductivities that cannot be detected by EIT," *Physiological Measurement*, vol. 24, no. 2, pp. 413–419, 2003.

[31] R. Kohn, H. She, M. Vogelius, and M. Weinstein, "Cloaking via change of variables in electric impedance tomography," *Inverse Problems*, vol. 24, no. 1, p. 015016, 2008.

[32] D. Colquitt, I. Jones, N. Movchan, A. Movchan, M. Brun, and R. McPhedran, "Making waves round a structured cloak: lattices, negative refraction and fringes," *Proceedings of the Royal Society A*, vol. 469, no. 2157, 2013.

[33] A. Norris, "Acoustic cloaking theory," *Proceedings of the Royal Society A*, vol. 464, no. 2097, pp. 2411–2434, 2008.

[34] G. Milton, M. Briane, and J. Willis, "On cloaking for elasticity and physical equations with a transformation invariant form," *New Journal of Physics*, vol. 8, p. 248, 2006.

[35] M. Brun, S. Guenneau, and A. Movchan, "Achieving control of in-plane elastic waves," *Applied Physics Lettters*, vol. 94, p. 061903, 2009.

[36] A. Norris and A. Shuvalov, "Elastic cloaking theory," *Wave Motion*, vol. 48, no. 6, pp. 525–538, 2011.

[37] G. Milton and J. Willis, "On modifications of Newton's second law and linear continuum elastodynamics," *Proceedings of the Royal Society A*, vol. 463, no. 2079, pp. 855–880, 2007.

[38] D. Colquitt, M. Brun, M. Gei, A. Movchan, N. Movchan, and I. Jones, "Transformation elastodynamics and cloaking for flexural waves," *Journal of the Mechanics and Physics of Solids*, vol. 72, pp. 131–143, 2014.

[39] M. Brun, D. Colquitt, I. Jones, A. Movchan, and N. Movchan, "Transformation cloaking and radial approximations for flexural waves in elastic plates," *New Journal of Physics*, vol. 16, no. 093020, 2014.

[40] M. Kadic, T. Bückmann, R. Schittny, and M. Wegener, "Metamaterials beyond electromagnetism," *Reports on Progress in Physics*, vol. 76, no. 12, p. 126501, 2013.

[41] R. Fleury and A. Alù, "Cloaking and Invisibility: a Review (Invited Review)," *Progress In Electromagnetics Research*, vol. 147, pp. 171–202, 2014.

[42] M. Raza, Y. Liu, E. Lee, and Y. Ma, "Transformation thermodynamics and heat cloaking: a review," *Journal of Optics*, vol. 18, no. 4, p. 044002, 2016.

[43] N.-A. Nicorovici, R. McPhedran, and G. Milton, "Transport properties of a three-phase composite material: the square array of coated cylinders," *Proceedings of the Royal Society A*, vol. 442, no. 1916, pp. 599–620, 1993.

[44] N.-A. Nicorovici, R. Mcphedran, and G. Milton, "Unusual Resonant Phenomena where Image Charges have a Real Significance," *Physical Review B*, vol. 49, 1994.

[45] N.-A. Nicorovici, R. McPhedran, S. Enoch, and G. Tayeb, "Finite wavelength cloaking by plasmonic resonance," *New Journal of Physics*, vol. 10, no. 11, p. 115020, 2008.

[46] G. Milton, N.-A. Nicorovici, R. McPhedran, K.Cherednichenko, and Z. Jacob, "Solutions in folded geometries, and associated cloaking due to anomalous resonance," *New Journal of Physics*, vol. 10, no. 11, p. 115021, 2008.

[47] A. Norris and C. Vemula, "Scattering of flexural waves on thin plates," *Journal of Sound and Vibration*, vol. 181, no. 1, pp. 115–125, 1995.

[48] V. Zalipaev, A. Movchan, C. Poulton, and R. McPhedran, "Elastic waves and homogenization in oblique periodic structures," *Proceedings of the Royal Society A*, vol. 458, no. 2024, pp. 1887–1912, 2002.

[49] R. McPhedran, A. Movchan, and N. Movchan, "Platonic crystals: bloch bands, neutrality and defects," *Mechanics of Materials*, vol. 41, no. 4, pp. 356–363, 2009.

[50] C. Poulton, A. Movchan, R. McPhedran, N. Nicorovici, and Y. Antipov, "Eigenvalue problems for doubly periodic elastic structures and phononic band gaps," *Proceedings of the Royal Society A*, vol. 456, no. 2002, pp. 2543–2559, 2000.

[51] A. Movchan, N. Movchan, and R. McPhedran, "Bloch-Floquet bending waves in perforated thin plates," *Proceedings of the Royal Society A*, vol. 463, no. 2, pp. 2505–2518, 2007.

[52] C. Poulton, R. McPhedran, N. Movchan, and A. Movchan, "Convergence properties and flat bands in platonic crystal band structures using the multipole formulation," *Waves in Random and Complex Media*, vol. 20, no. 4, pp. 702–716, 2010.

[53] M. Smith, M. Meylan, and R. McPhedran, "Scattering by cavities of arbitrary shape in an infinite plate and associated vibration problems," *Journal of Sound and Vibration*, vol. 330, no. 16, pp. 4029–4046, 2011.

[54] M. Smith, M. Meylan, and R. McPhedran, "Flexural wave filtering and platonic polarizers in thin elastic plates," *The Quarterly Journal of Mechanics and Applied Mathematics*, vol. 66, no. 4, pp. 437–463, 2013.

[55] A. Søe-Knudsen, "On advantage of derivation of exact dynamical stiffness matrices from boundary integral equations (L)," *The Journal of the Acoustical Society of America*, vol. 128, pp. 551–554, 2010.

[56] A. Søe-Knudsen, "Design of stop-band filter by use of curved pipe segments and shape optimization," *Structural and Multidisciplinary Optimization*, vol. 44, no. 6, pp. 863–874, 2011.

[57] S. Lee and J. Y. Hsiao, "Free in-plane vibrations of curved nonuniform beams," *Acta Mechanica*, vol. 155, no. 3, pp. 173–189, 2002.

[58] B. Lee and J. Wilson, "Free vibrations of arches with variable curvatures," 1989.

[59] S. Walsh and R. White, "Vibration power transmission in curved beams," *Journal of Sound and Vibration*, vol. 233, no. 3, pp. 455–488, 2000.

[60] L. Brillouin, *Wave Propagation in Periodic Structures: Electric Filters and Crystal Lattices*. New York: Dover Publications Inc., 2nd ed.corrections and additions, 1946.

[61] K. Graff, *Wave motion in elastic solids*. Oxford: Oxford University Press, 1975.

[62] J. Achenbach, *Wave Propagation in Elastic Solids*. North Holland Series in Applied Mathematics and Mechanics, 1973.

[63] A. Leissa and M. Qatu, *Vibrations of Continuous Systems*. McGraw-Hill Education, 2011.

[64] M. Qatu, *Vibration of laminated shells and plates*. Academic Press, 2004.

[65] S. Markus and T. Nanasi, "Vibrations of curved beams," *Shock and Vibration Digest*, vol. 13, no. 4, pp. 3–14, 1981.

[66] P. Chidamparam and A. Leissa, "Vibration of planar curved beams, rings, and arches," *Applied Mechanics Reviews*, vol. 46, no. 9, pp. 467–483, 1993.

[67] N.-I. Kim, K.-J. Seo, and M.-Y. Kim, "Free vibration and spatial stability of non-symmetric thin-walled curved beams with variable curvatures," *International Journal of Solids and Structures*, vol. 40, pp. 3107–3128, 2003.

[68] B. K. Lee, S. Oh, J. Mo, and T. Lee, "Out-of-plane free vibrations of curved beams with variable curvature," *Journal of Sound and Vibration*, vol. 318, no. 1-2, pp. 227–246, 2008.

[69] A. Søe-Knudsen and S. Sorokin, "Analysis of linear elastic wave propagation in piping systems by a combination of the boundary integral equations method and the finite element method," 2010.

[70] A. Søe-Knudsen and S. Sorokin, "Modelling of linear wave propagation in spatial fluid filled pipe systems consisting of elastic curved and straight elements," 2010.

[71] B. Kang, C. Riedel, and C. Tan, "Free vibration analysis of planar curved beams by wave propagation," *Journal of Sound and Vibration*, vol. 260, pp. 19–44, 2003.

[72] D. Mead, "Wave propagation in continuous periodic structures: research contributions from Southampton," *Journal of Sound and Vibration*, vol. 190, no. 3, pp. 495–524, 1996.

[73] F. Romeo and A. Luongo, "Invariants representation of propagation properties for bi-coupled periodic structures," *Journal of Sound and Vibration*, vol. 257, no. 5, pp. 869–886, 2002.

[74] G. Carta, M. Brun, and A. Movchan, "Dynamic response and localization in strongly damaged waveguides," *Proceedings of the Royal Society A*, vol. 470, no. 20140136, 2014.

[75] G. Carta and M. Brun, "Bloch-Floquet waves in flexural systems with continuous and discrete elements," *Mechanics of Materials*, vol. 87, pp. 11–26, 2015.

[76] G. Carta, M. Brun, A. Movchan, and T. Boiko, "Transmission and localisation in ordered and randomly-perturbed structured flexural systems," *International Journal of Engineering Science*, vol. 98, pp. 126–152, 2016.

[77] M. Morvaridi, G. Carta, and M. Brun, "Platonic crystal with low-frequency locally-resonant spiral structures: wave trapping, transmission amplification, shielding and edge waves," *Journal of the Mechanics and Physics of Solids*, no. 121, pp. 496–516, 2018.

[78] M. Smith, M. Meylan, R. McPhedran, and C. Poulton, "A short remark on the band structure of free edge platonic crystals," *Waves in Random and Complex Media*, vol. 24, no. 4, pp. 421–430, 2014.

[79] P. Ewald, "Die Berechnung optischer und elektrostatischer Gitterpotentiale (Evaluation of optical and electrostatic lattice potentials)," *Annalen der Physik (Leipzig)*, vol. 369, no. 3, pp. 253–287, 1921.

[80] C. Berman and L. Greengard, "A renormalization method for the evaluation of lattice sums," *Journal of Mathematical Physics*, vol. 35, no. 11, pp. 6036–6048, 1994.

[81] S. Chin, N. Nicorovici, and R. McPhedran, "Green's function and lattice sums for electromagnetic scattering by a square array of perfectly conducting cylinders," *Physical Review*, vol. E49, no. 5, pp. 4590–4602, 1994.

[82] M. Meylan and L. Gross, "A parallel algorithm to find the zeros of a complex analytic function," *Australia and New Zealand Industrial and Applied Mathematics Journal*, vol. 44, no. E, pp. E236–E254, 2003.

[83] W. Ewing, *Elastic Waves In Layered Media*. McGraw Hill Book Company Inc., 1957.

[84] M. Abramowitz and I. Stegun, *Handbook of mathematical functions with formulas, graphs, and mathematical tables*. New York, NY:Dover Publications, 1965.

[85] L. Rayleigh, "On the influence of obstacles arranged in rectangular order upon the properties of medium," *Philosophical Magazine*, vol. 34, no. 211, pp. 481–502, 1892.

[86] A. Moroz, "Quasi-periodic Green's functions of the Helmholtz and Laplace equations," *Journal of Physics A*, vol. 39, no. 36, pp. 11247–11282, 2006.

[87] F. Maurin, C. Claeys, E. Deckers, and W. Desmet, "Probability that a band-gap extremum is located on the irreducible Brillouin-zone contour for the 17 different plane crystallographic lattices," *International Journal of Solids and Structures*, vol. 135, pp. 26–36, 2018.

[88] A. Dykhne, "Conductivity of a two-dimensional two-phase system," *Soviet Physics Journal of Experimental and Theoretical Physics*, vol. 32, no. 1, pp. 110–115, 1971.

[89] J. Keller, "A theorem on the conductivity of a composite medium," *Journal of Mathematical Physics*, vol. 5, no. 4, pp. 548–549, 1964.

[90] J. Flaherty and J. Keller, "Elastic behavior of composite media," *Communications in Pure and Applied Mathematics*, vol. 26, no. 4, pp. 565–580, 1973.

[91] P. Suquet, "Une methode simplifié pour le calcul des propriétés élastiques de matériaux hétérogénes a structure périodique," *Comptes Rendue de l'Académie des Sciences Seriés*, vol. 311, no. 2b, pp. 769–774, 1990.

[92] M. Brun, O. Lopez-Pamies, and P. C. neda, "Homogenization estimates for fiber-reinforced elastomers with periodic microstructures," *International Journal of Solids and Structures*, vol. 44, no. 18-19, pp. 5953–5979, 2007.

[93] J. Pendry, A. Holden, W. Stewart, and I. Youngs, "Extremely Low Frequency Plasmons in Metallic Mesostructures," *Physical Review Letters*, vol. 76, no. 25, pp. 4773–4776, 1996.

[94] R. Shelby, D. Smith, and S. Shultz, "Experimental Verification of a Negative Index of Refraction," *Science*, vol. 292, no. 5514, pp. 77–79, 2001.

[95] H. Bondi, "Negative Mass in General Relativity," *Reviews of Modern Physics*, vol. 29, no. 3, pp. 423–428, 1957.

[96] Z. Liu, X. Zhang, Y. Mao, Y. Zhu, Z. Yang, C. Chan, and P. Sheng, "Locally Resonant Sonic Materials," *Science*, vol. 289, no. 5485, pp. 1734–1736, 2000.

[97] Y. Ding, Z. Liu, C. Qiu, and J. Shi, "Metamaterial with Simultaneously Negative Bulk Modulus and Mass Density," *Physical Review Letters*, vol. 99, no. 9, p. 093904, 2007.

[98] X. Liu, G. Hu, G. Huang, and C. Sun, "An elastic metamaterial with simultaneously negative mass density and bulk modulus," *Applied Physics Letters*, vol. 98, no. 25, p. 251907, 2011.

[99] N.-A. Nicorovici, D. McKenzie, and R. McPhedran, "Optical resonances of three-phase composites and anomalies in transmission," *Optics Communications*, vol. 117, no. 1-2, pp. 151–169, 1995.

[100] G. Milton and N.-A. Nicorovici, "On the cloaking effects associated with anomalous localized resonance," *Proceedings of the Royal Society A*, vol. 462, no. 2074, pp. 3027–3059, 2006.

[101] Y. Liu, B. Gralak, R. McPhedran, and S. Guenneau, "Finite frequency external cloaking with complementary bianisotropic media," *Optics Express*, vol. 22, no. 14, pp. 17387–17402, 2014.

[102] H. Ziegler, "On the Concept of Elastic Stability," *Advances in Applied Mechanics*, vol. 4, pp. 351–403, 1956.

[103] D. Smith, J. Pendry, and M. Wiltshire, "Metamaterials and Negative Refractive Index," *Science*, vol. 305, no. 5685, pp. 788–792, 2004.

[104] J. Achenbach, *Reciprocity in Elastodynamics*. Cambridge University Press, 2004.

[105] J. Miklowitz, *The Theory of Elastic Waves and Waveguides*, vol. 22. North Holland Publishing Company, Amsterdam, 1978.

[106] F. Liu, Y. Lai, X. Huang, and C. Chan, "Dirac cones at $\vec{k} = 0$ in phononic crystals," *Physical Review B*, vol. 84, no. 8, p. 224113, 2011.

[107] J. Mei, Y. Wu, C. Chan, and Z. Zhang, "First-principles study of Dirac and Dirac-like cones in phononic and photonic crystals," *Physical Review B*, vol. 86, no. 3, p. 035141, 2012.

[108] R. McPhedran, A. Movchan, N. Movchan, M. Brun, and M. Smith, "Parabolic trapped Modes and Steered Dirac Cones in Platonic Crystals," *Proceedings of the Royal Society A*, vol. 471, no. 2177, p. 20140746, 2015.

[109] M. Abramowitz and I. Stegun, *Handbook of Mathematical Functions with Formulas, Graphs, and Mathematical Tables*. United States Department of Commerce, National Bureau of Standards (NBS), 1964.

[110] S. Timoshenko and J. Gere, *Theory of elastic stability*. McGraw-Hill, Singapore, 1968.